Theses and Dissertations

Theses, Dissertations, and Senior Projects

January 2018

Small-Scale Characterization Of Additive Manufactured Ti-6al-4v Alloy Through Instrumented Indentation

Muztahid Muhammad

Follow this and additional works at: https://commons.und.edu/theses

SMALL-SCALE CHARACTERIZATION OF ADDITIVE MANUFACTURED TI-6AL-4V ALLOY THROUGH INSTRUMENTED INDENTATION

by

Muztahid Muhammad
Bachelor of Science, Military Institute of Science and Technology, 2015

A Thesis
Submitted to the Graduate Facility

of the

University of North Dakota

in partial fulfillment of the requirements

for the degree of

Master of Science

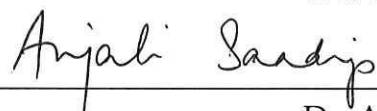Grand Forks, North Dakota

December
2018

This thesis, submitted by Muztahid Muhammad in partial fulfillment of the requirements for the Degree of Master of Mechanical Engineering from the University of North Dakota, has been read by the Faculty Advisory Committee under whom the work has been done and is hereby approved.

_____
Dr. Meysam Haghshenas

_____
Dr. Cai Xia Yang

_____
Dr. Anjali Sandip

This thesis (or dissertation) is being submitted by the appointed advisory committee as having met all of the requirements of the School of Graduate Studies at the University of North Dakota and is hereby approved.

_____
Grant McGimpsey
Dean of the School of Graduate Studies

_____
December 5, 2018
Date

PERMISSION

Title   Small-Scale Characterization of Additive Manufactured Ti-6Al-4V
               Alloy Through Instrumented Indentation

Department Mechanical Engineering

Degree   Master of Science

In presenting this thesis in partial fulfillment of the requirements for a graduate degree from the University of North Dakota, I agree that the library of this University shall make it freely available for inspection. I further agree that permission for extensive copying for scholarly purposes may be granted by the professor who supervised my thesis work or, in his (or her) absence, by the Chairperson of the department or the dean of the School of Graduate Studies. It is understood that any copying or publication or other use of this thesis or part thereof for financial gain shall not be allowed without my written permission. It is also understood that due recognition shall be given to me and to the University of North Dakota in any scholarly use which may be made of any material in my thesis.

Muztahid Muhammad
DATE 12/05/2018

TABLE OF CONTENTS

LIST OF FIGURES

LIST OF TABLES

ACKNOWLEDGMENTS

All the praises go to the almighty

ABSTRACT

Ti-6Al-4V alloy has been favored by the transportation applications in the automotive and aerospace industries due to its good combination of excellent physical and mechanical properties. Ti alloys are naturally suited to additive manufacturing (AM) method, a layer wise manufacturing technique, since conventional manufacturing method of Ti alloys are quiet challenging. However, cooling rate and thermal processing history of AM Ti-6Al-4V alloy are quite different in comparison to conventionally fabricated Ti-6Al-4V alloy which leads to undesirable microstructures in the AM Ti-6Al-4V alloy with respect to large columnar prior β grains being found to grow potentially across the entire height from bottom layer to top layer. Therefore, it is required to assess the microstructure-process-structure-property-performance relationship of the additive manufactured Ti-6Al-4V alloy to assess whether it could meet the demands of engineering design considerations.

The samples studied in this research were prepared using laser powder bed fusion (L-PBF) method, a well-developed AM process to print Ti-6Al-4V alloy in different scan direction and scan size. Instrumented indentation testing technique, a robust, reliable, convenient, and non-destructive characterization method to study small-scale mechanical properties in metals and alloys at ambient and elevated temperatures, was used to assess ambient-temperature indentation creep of AM Ti-6Al-4V alloy. To examine depth-sensing indentation creep behavior of Ti-6Al-4V alloy at ambient temperature, a dual-stage scheme (loading followed by a constant load-holding and unloading) at different peak loads of 250 mN, 350 mN, and 450 mN with holding time of 400 s was performed. Creep parameters *i.e.* creep rate, creep stress exponent, and indentation size effect were analyzed and compared with conventional findings, according to the Oliver and Pharr method, at different additive manufacturing scan directions and scan sizes.

The effect of post heat treatment (*i.e.* aging and solutionizing with different cooling rates) on the microstructure and micromechanical properties of a Ti-6Al-4V alloy processed by laser powder bed fusion (L-PBF) technique is studied. Heat treatment cycles employed in this study include solutionizing at 950 °C (for 1 h) followed by three different cooling rates (water quench, air cooling, and furnace cooling). A separate set of samples were also used toward artificial aging (solutionizing followed by water quenching and artificial aging). To assess small-scale properties of as-printed/ heat treated materials, instrumented nanoindentation testing technique as a robust, convenient, and non-destructive approach is employed. The martensitic α and $\acute{\alpha}$ in as -printed Ti-6Al-4V alloy grows in lamellar structure in epitaxial way upon various heat treatments below β-transus temperature. With the relatively steep cooling rate, the β phase recrystallization transforms into a compact secondary basket-weave α phase since the primary α-phase develops and connects each other with different orientations.

Microstructural quantitative analyses (*i.e.* optical microscopy and scanning electron microscopy) were performed as well to assess processing parameter-microstructure-property correlations in the additively manufacture Ti-6Al-4V alloy. These studies were done in parallel to the two main tasks of this project to be able to elaborate the mechanical measurements with microstructural evidences. Also, the obtained results were compared against traditionally processed Ti-6Al-4V.

Chapter I

1. Introduction

1.1. Background Information and Motivation

Titanium (Ti), named after the 'Titans' of Greek mythology, has emerged as a powerful metal of interest for transportation applications in the automotive and aerospace industries for the past several decades due to combination of its distinguishable physical and mechanical properties [15]. Ti (atomic number 22 and atomic weight 47.9) is a lustrous transition metal with a silver color, low density, light weight (almost half of steel), and high strength (almost similar to steel), and excellent biocompatibility [15]–[18]. Ti is resistant to corrosion in sea water, aqua regia, and chlorine. Its corrosion resistance and strength-to-density ratio is highest of any metallic element. It can form stable and adherent surface oxide layer upon exposure to water and air which has made Ti and its alloy and excellent candidates in extreme corrosive environments and sea water [15]. Moreover, Titanium is well-sought for high temperature applications due to its great strength-to-weight ratio at elevated temperature [15].

Among different Ti alloys, Ti-6Al-4V alloy (UNS designation R56400, AMS designation 4911) is known as the 'workhorse' [19] alloy which accounts for more than half of all commercial Ti applications. Its applications include but not limited to implants and prostheses (wrought and/or cast), additive manufacturing, parts and prototypes for racing and aerospace industry, marine applications, chemical industry, gas turbines etc. However, traditional fabricating methods like welding, casting, forming, and machining of the Ti-6Al-4V alloy, are quite challenging due to high-temperature oxidation, high chemical reactivity, and poor thermal conductivity. Additive manufacturing (AM), a layer-wise material manufacturing method, despite being a relatively new family of processing technologies seems to be a suitable replacement for the conventional manufacturing processes of the Ti-6Al-4V alloy.

The AM of Ti-6Al-4V alloy is particularly well suited thank to both complexities associated with machining and the inherent high cost of the raw materials. The additive manufacturing of the Ti-6Al-4V alloy possesses several advantages over conventional manufacturing method including:

- Cost reduction.
- Decreased labor cost and material wastage.
- Smaller footprints.
- Less process.

- No mold and pattern.
- Shorten fabrication time.
- Enhanced material properties.

There are also few disadvantages associated with additive manufacturing processes such as:

- Slow build rates.
- High production cost.
- Considerable effort in application design and setting process parameters.
- Requires post-processing.
- Discontinuous production process.
- Limited component size/small build volume.
- Poor mechanical properties.

Among different AM techniques, laser powder bed fusion (L-PBF), also known as direct metal laser sintering (DMLS), is a well-developed process to print the Ti-6Al-4V alloy. In the L-PBF process, high power density laser is used to melt and fuse metallic powder together [20]. Cooling rate during the additive manufacturing process and thermal processing history are quite different compared with conventional manufacturing processes that lead to the development of inconvenient microstructures where large columnar prior β grains, undesirable residual stress, and distortion. This type of microstructure has the tendency to influence mechanical property anisotropy.

As Ti-6Al-4V alloy is a two-phase alloy and consistency of mechanical properties and microstructures in additive manufacturing is still a critical issue, mechanical properties can be significantly varied by tailored microstructure [21]. The microstructure of Ti-6Al-4V alloy, in particular formation of α, can vary a lot due to various cooling rates at different positions and distances from the built plate in different additive manufacturing methods [22]. Formation of layers with repeated partial re-melting and solidification of previous layer and cooling in various ways for various geometries adds complications to the processes. In spite of many studies in the literature to date, rate dependent plastic deformation and effect of the post heat treatment cycles of the Ti-6Al-4V alloy manufactured by the L-PBF method has not been studied at small scales with microstructural gradients. Therefore, it is necessary to assess the relationship between the microstructure, processing parameters, and properties (*i.e.* creep) of the additively manufactured Ti-6Al-4V alloys to determine its ability in meeting demands of the engineering design considerations.

Depth-sensing (instrumented) indentation testing technique is a robust, convenient and non-destructive characterization method to study small-scale and local mechanical

properties in metals and alloys at ambient and elevated temperatures. In this thesis, depth-sensing indentation creep behavior and effect of post heat treatment cycles analysis of an additively manufactured Ti-6Al-4V alloy, manufactured via laser powder bed fusion (L-PBF) method at different scan directions and scan sizes, is studied at ambient temperature through an indentation-based study. Microstructural quantitative analyses (i.e. optical microscopy and scanning electron microscopy) were performed to assess microstructure of additively manufactured Ti-6Al-4V $\alpha+\beta$ alloy, and creep property correlations during the holding time as a function of indenter load.

1.2. Problem Statement and Scope of Thesis

1.2.1. Ambient temperature creep behavior

A number of researchers have used instrumented indentation technique and conventional methods (uniaxial tension) to assess rate-dependent plastic deformation of Ti and Ti alloys. Ma *et al.* [23] used micro-indentation to study room temperature creep behavior of Ti-10V-2Fe-3Al based on dislocation mechanism by micro-indentation and found that power-law creep deformation was the controlling mechanism of creep in Ti-10V-2Fe-3Al alloy. Kumar *et al.* analyzed creep-fatigue interactions in the Ti-6Al-4V alloy at ambient temperature [24]. Matsunaga *et al.* experimented creep tests on polycrystalline Ti along with pure Mg and pure Zn at ambient temperature and found steady state creep rate around 10^{-9} s^{-1} and creep stress exponents (n) around 3.0 at ambient temperature [25]. Hasija *et al.* analyzed time-dependent plasticity by developing a computational model [26]. Barboza *et al.* studied creep behavior of conventionally made Ti-6Al-4V alloy consisting of Widmanstätten microstructure using conventional uniaxial test and found different creep stress exponents (n) as 4.4 and 4.1 at 500^{0}C and 600^{0}C respectively [27]. Kral *et al.* [8] using conventional uniaxial approach analyzed rate-dependent plastic deformation in conventionally manufactured ultrafine-grained Ti-6Al-4V at both elevated temperatures and ambient-temperature indentation creep. Badea *et al.* [6] investigated creep behavior of hot-forged Ti-6Al-4V alloy and compared the creep stress exponent and activation energy at different temperature ranges. However, it's worth mentioning that, at higher stresses, Ti alloys can sometimes exhibit unusually high creep stress exponent values, such as n > 15 [6].

There has been numerous reports of occurring ambient-temperature creep[1] in $\alpha+\beta$ Ti–6Al–4V [16], [20]. The hexagonal close packed (hcp) crystalline structure of the Ti-6Al-4V is responsible for the ambient-temperature creep in general [7, 28]. During room temperature creep, in the hcp structure, only one slip system is activated which is due to

---

[1] Ambient-temperature creep appears below *0.3–0.4T$_m$* for the tested *hcp* metals.

the low symmetric structure, generating low work hardening. As a result, deformation proceeds at ambient temperature and under stresses below the yield stress [7, 28].

Harrison *et al.* [29] studied time dependent creep of Ti-6Al-4V by developing a model where strain accumulation is generated by dwell time fatigue effects at ambient "cold" temperature creep. Moreover, the occurrence of ambient temperature (or logarithmic) creep is not unusual in many materials including pure Ti and Ti alloys [30–32].

The prime factor in low-temperature (*i.e.* ambient temperature) creep sensitivity of Ti alloys (*i.e.* Ti-6Al-4V) is strong tendency of Ti in time-dependent strain accumulation at low temperatures [28]. According to the design criteria, the stress levels that impose the mentioned strain accumulations are normally in the acceptable (safe) range. To this end, understanding the nature of creep sensitivity could be a challenging task but it provides a foundation for our understanding on crack development in $\alpha+\beta$ Ti alloys. For instance, ambient-temperature creep in the Ti-6Al-4V alloy fuel tanks and fasteners has been reported previously in the literature [23].

Having stated the above-mentioned literature, ambient-temperature creep response of an additively manufactured Ti-6Al-4V alloy and correlations between creep parameters (*i.e.* creep rate, creep stress exponent, indentation strain rate sensitivity) and additive manufacturing printing parameter variables (*i.e.* scan directions and scan sizes) has not yet been documented. In the present study an instrumented (depth-sensing) indentation testing technique was employed to assess ambient-temperature creep and the corresponding mechanisms of an additively manufactured (AM) Ti-6Al-4V alloy. Besides, indentation size effect and microstructural assessments were studied in the present thesis. To this end, microstructural quantitative analyses (*i.e.* optical microscopy (OM) and scanning electron microscopy (SEM)) are performed to assess microstructure of the AM Ti-6Al-4V alloy and the creep property correlations during the holding time as a function of indenter peak load.

The findings of this thesis provide a baseline to study elevated-temperature creep of AM Ti-6Al-4V alloy and to compare the results with the conventionally made Ti-6Al-4V alloy. Most of the reported creep results in the literature are based upon traditional (tensile) approach which could be destructive, time-consuming and tough-to-control (specially at the elevated temperatures) tests. Specifically, on the AM aspect, a number of creep test coupons must be printed which could be a costly task as well. Considering this, the present thesis promotes the application of the depth-sensing indentation testing technique, as a reliable, convenient, and non-destructive approach that can be performed on a small volume of material and can be used toward assessing time-dependent plastic deformation (creep) in AM materials at ambient and elevated temperatures.

1.2.2. Study of effect of post heat treatment cycles

Due to short interaction times and accompanying highly localized heat input, large thermal gradients exist during L-PBF process which results in build-up of thermal processes. Rapid solidification leads to segregation phenomena and development of non-equilibrium process Moreover, additive manufacturing variables (scan size and scan directions) may affect melt pool stabilities during the process, which leads to an increased porosity and higher surface roughness.

To ensure optimal building conditions, heat treatment of Ti-6Al-4V alloy has been investigated extensively [11, 33–35]. AM Ti-6Al-4V alloy manufactured via L-PBF technique experience a high yield stress, a high tensile strength, but relatively low ductility. To improve the ductility [36] and to achieve the desirable microstructural properties of Ti-6Al-4V alloy manufactured via L-PBF method, heat treatment may be a viable option. In addition, post heat treatment reduces the thermal stresses that has been built up during the process. However, there has been limited research based on the additive manufacturing variables [37, 38].

In this thesis an instrumented (depth-sensing) indentation testing technique was employed to assess the effect of post heat treatment cycles (cooling rates) and the corresponding mechanisms of an additively manufactured (AM) Ti-6Al-4V alloy at different scan size and scan directions. The heat treatments employed in this thesis include (*i*) an aging treatment (solutionizing at 950 °C for an hr and then aging at 540^0C for 5 hrs), (*ii*) solutionizing at cooling with different rates (solutionizing at 950 °C for an hr followed by water quench, solutionizing at 950 °C for an hr followed by air cooling, and solutionizing at 950 °C for an hr followed by furnace cooling). It is desired to study the effect of cooling rate and aging on the microstructure and mechanical properties of the AM Ti-6Al-4V and to compare the results with the as-printed sample.

1.3 Thesis Organization

The thesis has been divided into five chapters which are as follows:

- Chapter one provides introduction to the thesis topic and states the motivation and objectives of the work.
- Chapter two introduces background information regarding titanium alloys, Ti-6Al-4V alloy, additive manufacturing, and instrumented indentation technique. It includes the discussion of the established theories and studies regarding the effect of features on the microstructural mechanical properties of Ti alloys and Ti-6Al-4V alloy. It further discusses microstructure-process-property relationship of Ti-6Al-4V alloy.

- Chapter three presents the various experimental methods used in this research.
- Chapter four discussed the experimentally observed results and correlation established between the local mechanical properties and microstructural features of AM Ti-6Al-4V alloy. The experimental results determined via instrumented indentation technique for Ti-6Al-4V alloy were also compared with conventionally manufactured Ti-6Al-4V alloy. The relationship between microstructures and mechanical properties for each sample examined were reported.
- Chapter 5 provides conclusions of the research results and recommendations to further understanding the relationship among microstructure-process-property relationship.

Chapter II

2. Literature Review

2.1. Titanium alloys

2.1.1. Introduction

Titanium (Ti) has been a metal of interest for transportation applications in the automotive and aerospace industries due to its excellent physical and mechanical properties. Having many desirable properties such as light weight (almost half of steel), high specific strength (almost similar to steel) and stiffness, use and development of the titanium alloy has been dominated by aerospace industry for over the past half century [17], [39], [40]. Excellent biocompatibility such as being non-toxic, non-allergic as well as Ti alloys with shape memory and superelastic properties increased its use in biomedical industries [18]. In addition, Ti and its alloys can form a stable and adherent surface oxide upon exposure to water and air and this ability has made Ti alloys excellent candidates for structural efficiency in extreme corrosive environments and sea water [39]. Moreover, its high strength-to-weight ratio at elevated temperatures have made Ti a suitable material for both ambient and high temperature applications [39]. However, high cost of extraction and processing of Ti metals has limited it's applications [41].

Having great strength-to-weight ratio and providing substantial weight have given Ti alloys an upper hand over steel for use in aerospace components. Although using Ti alloys instead of aluminum could be quite costly, Ti alloys possess the advantage of operating at far higher operating range where elevated temperature becomes an issue for aluminum alloy, or where volume constraints rule out the use of thicker gauge aluminum components [42]. Superior compatibility with composite materials, leading to weight reduction of composite materials in aircraft manufacturing, has increased the use of Ti alloys manifold in the aerospace industry [43].

In this section, along with the discussion of the main focus of this thesis, Ti-6Al-4V alloy, a brief metallurgical background of Ti alloys including crystallography and deformation mechanism were described. Finally, suitability and acceptability of titanium alloys for fabricating via additive manufacturing (AM) was discussed along with the microstructure characterization and mechanical properties of the AM Ti-6Al-4V alloy.

2.1.2. Crystal structure of Ti alloys

Pure Ti consists of α hexagonal close packed (HCP) structure at ambient temperature which undergoes an allotropic phase transformation to a β body centered cubic (BCC) at a β-transus temperature of approximately 882 ⁰C that stays stable up to the melting point 1625 ⁰C [44]. These two types of crystal structure are shown in the Fig. 2:1. However, a mixed $\alpha+\beta$ is also found.
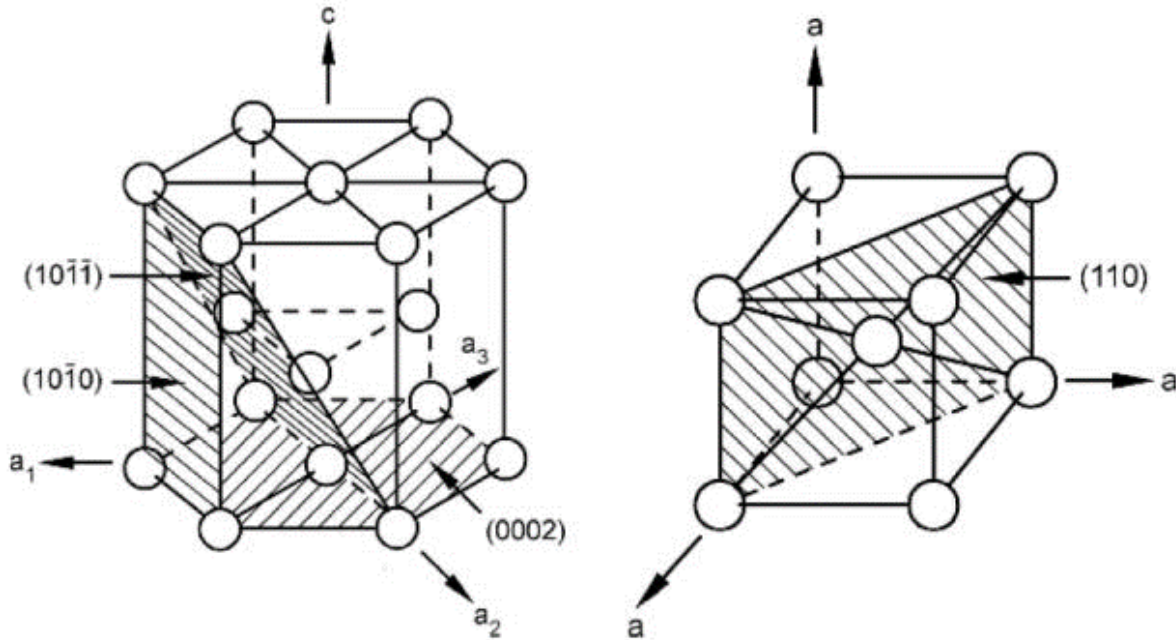
Fig. 2.1: The α (HCP) and β (BCC) unit cells of Ti [45].

Being a transition element with an incomplete outer shell in its electronic configuration, Ti has the ability to readily form alloy with the substitutional solid solutions with the most transitional elements within a reasonable atomic size difference to Ti atom [45]. Moreover, forming solid solutions by non-metallic interstitial elements possesses a profound effect on solid solution hardening. These alloying additions often stabilize one of the phases in order to keep one or both phases at operating temperature [45].

Due to lack of symmetry in HCP structure, α-phase lower ductility than the β-phase but exhibits higher creep resistance. The α-Ti possessed higher strength and stiffness but it is anisotropic. It's Young's modulus varies from 100 GPa to 145 GPa depending on the direction of applying load relative to the crystal orientation [45].

Phase distribution and volume distributions also affect both material and mechanical properties. The β-phase is both electrically [46] and thermally [47] more conductive than the α-phase. According to Fig 2.2, a sharp increase in conductivity at ~ 1150K is observed as Ti transforms from α to β.
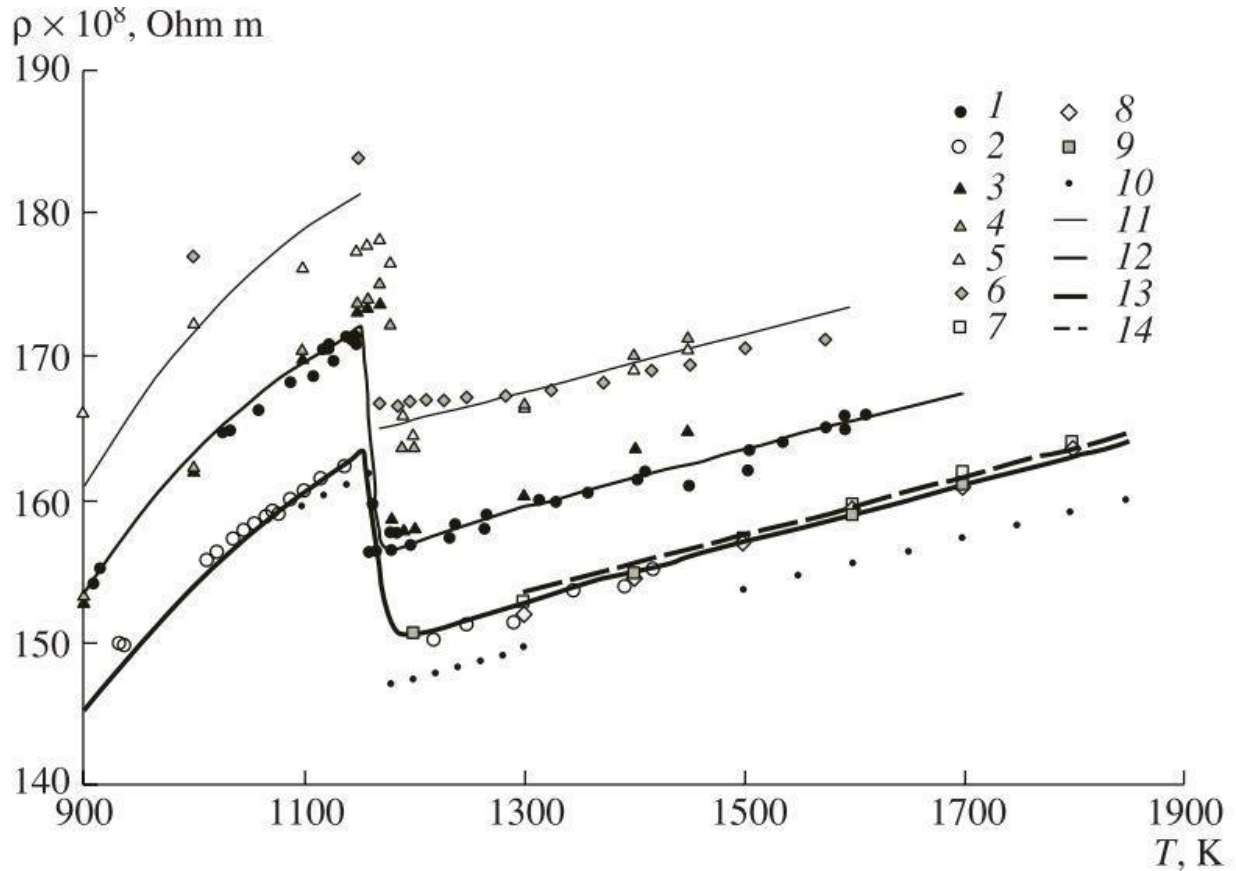
Fig. 2.2: Effect of temperature on the resistivity of commercially pure Ti [46].

Dual phase of Ti facilitates many alloying additions in Ti leading to numerous complex phase diagram of alloy composition. Major alloying additions have been classified into four categories as shown in Fig 2.3.
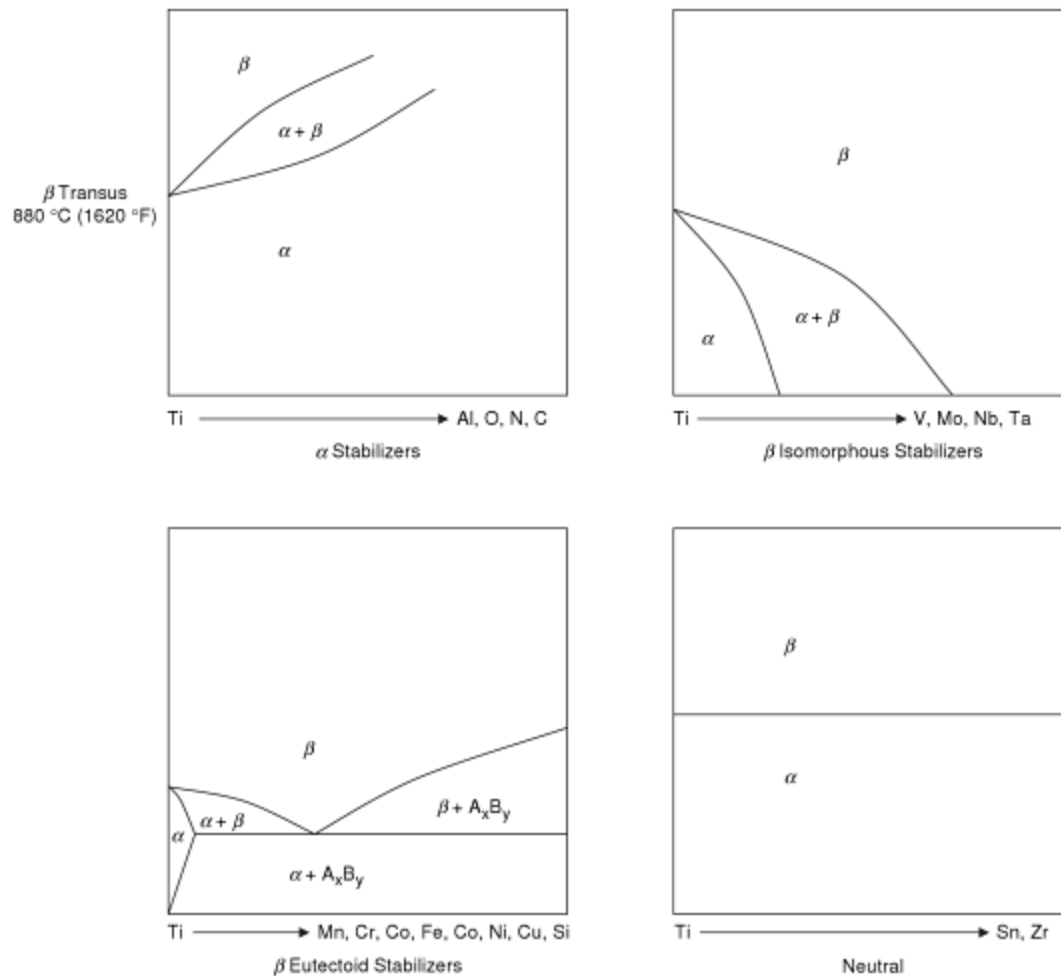
Fig. 2.3: Four generic binary phase diagram types of Ti alloy [48].

Alpha-stabilizers are the elements that increase the beta-transus. Al, O, N, and C are the most prominent alpha-stabilizers. They increase solute content after being added to the alloy. Oxygen can be added as an interstitial where adjustable strength level is required. B, Ga, Ge and the rare earth elements have lower solubility and are less used alpha stabilizers [45].

Beta stabilizers are the elements that decrease the temperature (beta -transus), dissolve in readily, strengthen the beta phase, and exhibit low alpha phase. Beta stabilizers can be split into two types:

a) **β-isomorphous stabilizers**: β-isomorphous stabilizers are isomorphous with or totally soluble in Ti.

b) **β- eutectoid stabilizers**: β- eutectoid stabilizers are of two types: β- isomorphous stabilizers and β- eutectoid stabilizers.

β- isomorphous stabilizers include molybdenum and vanadium which are isomorphous with, or totally soluble in Ti.

β- eutectoid stabilizers form intermetallic compounds with Ti and include Cu and Ni.

Neutral stabilizers neither stabilizes α or β phase. However, the addition of neutral alloying can alter other material properties like providing solid solution strengthening. Sn, Zr etc. are examples neutral stabilizers.

2.1.3. Ti phase transformation

It is common for many α grains to be nucleated at the β grain boundaries by cooling, generally leading to a relatively fine grained microstructure. As a results, the anisotropic properties of the room temperature hcp α-phase, does not always meet the expectation of strongly anisotropic fabricated parts. However, there is still a texture inherited from the β phase due to orientation relationship that is maintained between the β and α through the transformation. Therefore, limited number of different α orientations are formed from each β grain. Preferential α variant selection can also occur by further limiting textural weakening.

During the polymorphic Ti phase transformation, the same orientation relationship is maintained as was first observed by Burgers for single crystals of zirconium, a metal with similar phase behavior to Ti [49]. The Burgers orientation relationship is as follows:

$\{110\}_\beta \ || \ \{0002\}_\alpha \ \langle 111 \rangle_\beta \ || \ \langle 11\bar{2}0 \rangle_\alpha$

Upholding this Burgers orientation relationship ensures that there are only six possible orientations variants of β that can form from a single α grain in the $\alpha \rightarrow \beta$ transformations. Further 12 α orientation variants can be formed with the $\beta \rightarrow \alpha$ transformation. Total 72 variants should form with equal probability, effectively randomizing the α texture if all of the variants mentioned in the previous two transformations form within a heat cycle that sees the material transform $\alpha \rightarrow \beta \rightarrow \alpha$ [50]. If the transformation occurs, then the texture of material that has been through a heat treatment in the β-phase several times should have a very weak texture that bares little, if any, resemblance to the untreated material. However, sometimes there is an apparent preference for certain variants to form relative to others resulting in a stronger texture than would be expected. Variant selection may lead to the phenomenon of 'texture memory', where after β heat treatment the original α texture is recovered to a certain extent [51]. There are various factors affecting texture variant selection including deformation of the β-phase [52], an increased β grain size [53], and local internal strains [54].

2.2. Ti-6Al-4V alloy

2.2.1. Introduction

Among Ti alloys, Ti-6Al-4V alloy, which is also known as the 'workhorse' alloy [19], [42], accounts for more than half of all industrial Ti applications [15].

The Ti-6Al-4V alloy is an α-β alloy where 5.50 – 6.75% of the composition by weight is the α stabilizing element aluminum (Al), and 3.5 – 4.5% of the composition is the β stabilizing element vanadium (V) [55]. Ti-6Al-4V is the most widely manufactured alloy of the Ti industry, accounting for approximately 60% of all Ti metal production [42]. Due to its good combination of properties of high temperature strength, corrosion resistance, and good weldability [42], it is mostly used in aerospace industries. However, traditional manufacturing processes including welding, casting, forming, and machining of the Ti-6Al-4V alloy, are quite challenging due to high-temperature oxidation, high chemical reactivity, and poor thermal conductivity. Additive manufacturing, a layer-wise manufacturing technique, seems to be suitable solution for manufacturing problems arising from traditional manufacturing methods of Ti-6Al-4V alloy.

2.2.2. Microstructure of conventional Ti-6Al-4V alloy

The microstructure of Ti-6Al-4V alloy is largely dependent upon its thermal processing history. The cooling rate from the β-phase has an immense effect on the microstructure. On cooling slowly below the β-transus temperature, α is nucleated at the heterogeneous sites of β grain boundaries creating a continuous grain boundary layer. α lamella then proceed to grow by a diffusional process into the β grains by consuming them. At lower cooling rates α platelets tend to grow aligned with the same crystallographic orientation creating a 'colony' within close proximity. These colonies are shown in Fig. 2.4. Faster cooling rates results in finer α structures and several variants grow more inter-woven forming of a Widmanstätten or 'basket weave' microstructure [21]. Due to the growth of α enriching the β phase in vanadium, some β is retained down to room temperature to the point that the β is stable at room temperature [56]. Rapid cooling rate would be able to limit the amount of diffusion possible and therefore would result in the formation of martensitic structures. The most common martensite is α' which is similar in structure to equilibrium α but has slightly altered lattice constants due to the super-saturation of alloying elements. The α' laths tend to decompose into fine α plates with sufficient thermal energy for diffusion [57]. Martensitic microstructure is shown in Fig. 2.4.
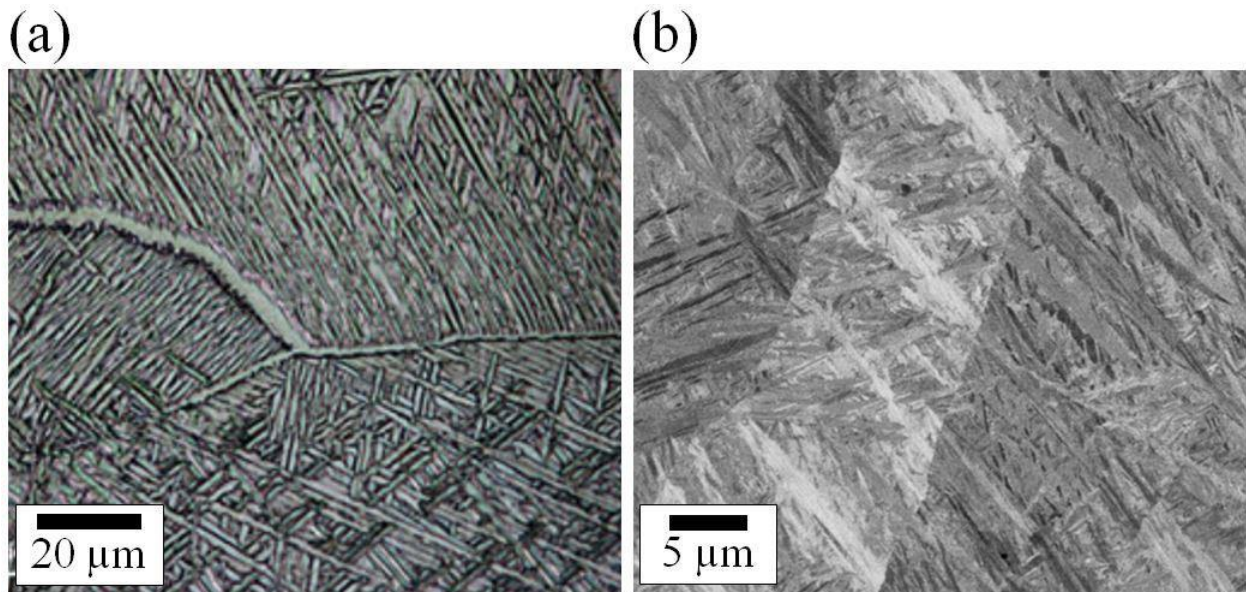
Fig. 2.4: Microstructures of Ti-6Al-4V: (a) Widmanstättaen microstructure [58] and (b) α martensitic microstructure [59].

Such microstructures are not, however, always desirable for optimum mechanical properties. Alternative Ti-6Al-4V microstructures can be tailored through more complex thermo-mechanical processing like Fig. 2.5 resulting in either a bi-modal (Fig 2.6 a) or fully equiaxed structure (Fig 2.6 b) depending on the cooling rate from step III of the process [45].
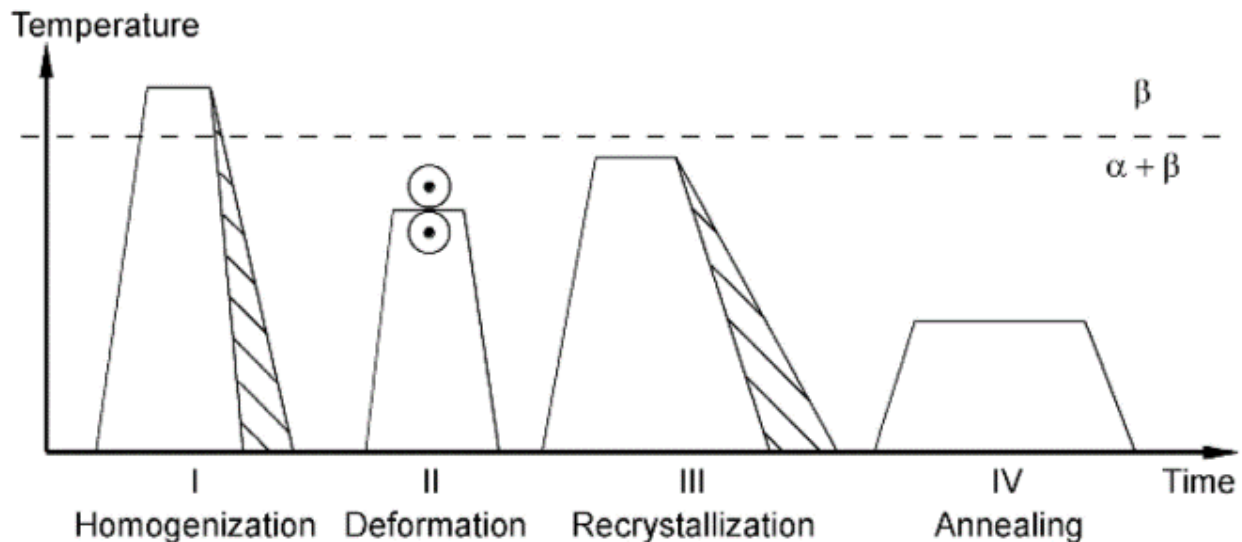
Fig. 2.5: Processing route for developing bi-modal and equiaxed Ti-6Al-4V [45].

Sometimes, in an attempt to produce a more uniform wrought microstructure, hot working is initially conducted in the single β phase field to recrystallize and anneal cast

material. By Dynamic Recrystallization (DRX), deformation in the β phase field refines the very coarse prior β grain structures formed on solidification [60], [61]. The resultant DRX grain size in Ti-6Al-4V shows good agreement with the Zener-Holloman relationship *i.e.* higher strain rates and lower temperatures lead to a finer recrystallization grain size [60]. However, it is also found that, the volume percentage recrystallized by DRX is reduced by the same parameters. For instance, deforming at temperatures above the β transus at 1050 °C, at rates of 1 s^{-1}, and down to a total strain 0.7, only 3.1% of the material is found to recrystallize [61]. The recrystallized volume fraction can be increased with the aid of higher deformation temperatures, lower strain rates, and higher total strains, although these changes are not favorable from a process practicality point of view, and these will lead to an increase in the recrystallized grain size [62].
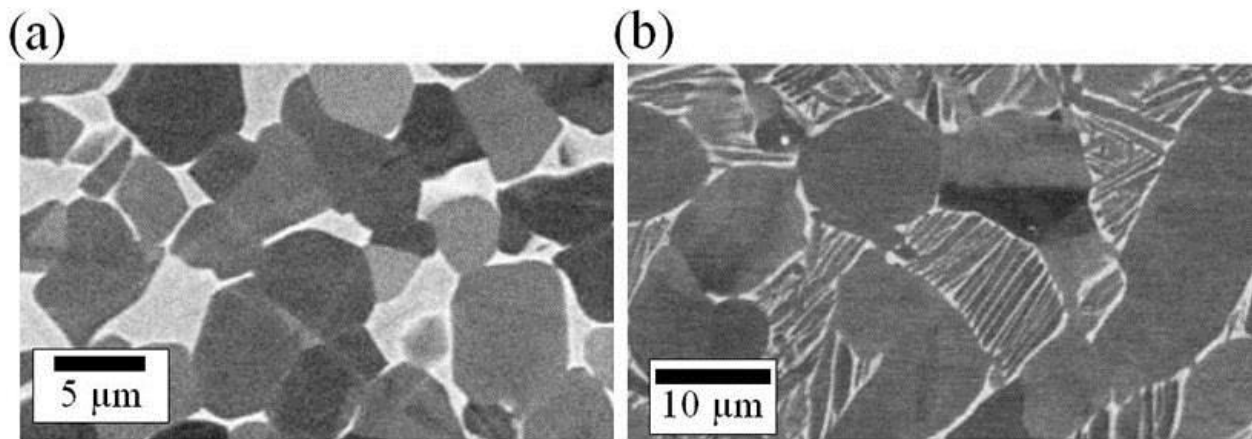
Fig. 2.6: a) bi-modal and b) fully equiaxed Ti-6Al-4V alloy microstructures obtainable through the processing route shown schematically [63]

Although α - β microstructure formed through the cooling from the β phase is dependent on the cooling rate, large prior β grain size is often a combination of Widmanstätten and colony α microstructures. Processes called 'spheroidisation' or 'globularisation', deformation in the α-β phase field break up this microstructure [64, 65]. Shape changes of a lamellar structure into a globular, equiaxed, morphology are occurred in the globularisation process. It is found to occur in a two-step processes: the deformation causes intense shear bands to form across and within α plates, and then the subsequent migration of interface boundaries to reduce surface energy which causes the penetration of the β phase to separate the α 'globules' [65, 66]. After the full break-up of the grain structure, the Burgers' orientation relationship is no longer maintained between the α variants [64].

2.2.3. Effects of Microstructure on Mechanical Properties

Mechanical properties of the Ti-6Al-4V alloy is strongly affected by the microstructure. Lütjering *et al*. [45] investigated the relation of the difference in mechanical properties to the effective slip length, equivalent to the size of the alpha laths, or colonies if present. Since the slip can transfer across α plate boundaries within a single colony, hence the entire colony is able to act as a large single grain [67]. It is found that reduced slip length does not only improve the strength but also enhances the fatigue life as both the nucleation and propagation can be linked to the colony size and slip length. Higher the cooling rate through the β transus temperature, the higher the strength and potential fatigue performance of the alloy. Continuous higher cooling rate produces a martensitic microstructure leading to a reduction in ductility [68] and creep resistance [44].

2.2.4. Prior β-Ti Solidification Microstructure

Mechanical properties of the Ti-6Al-4V alloy are determined by the α colony size. Since α-colony is in turn affected by the prior β grain size (as α laths can extend across entire prior β grains), it is desirable to have as fine prior β grain size as possible.

Large β grain sizes are common in Ti-6Al-4V alloy solidification microstructures which is partly due to the rapid β grain growth that takes place above the β transus, and partly due to the nature of the solidification itself.

2.2.5. Deformation Mechanisms of Ti-6Al-4V alloy

The dual phase microstructure of Ti-6Al-4V alloy has made the deformation mechanisms complex. At ambient temperature, the deformation behavior is dominated by the α-phase since it is a dominant phase making up to 95% of the volume of the alloy.

For the hexagonal close pack (*HCP*) phase, slip primarily occurs along the three $\langle 11\bar{2}0 \rangle$ close packed directions in the <a> direction. There are 12 slip planes that this slip direction can act in: one basal (0002), three prismatic $\{10\bar{1}0\}$, and six pyramidal $\{10\bar{1}1\}$. However, these planes are reduced to 4 independent systems due to symmetry and combinations of slip systems giving the same slip as can be achieved by another slip system [69]. This indicates that the Von Mises criterion for five independent slip systems is not fulfilled. Hence, a deformation mode with a component in the <c> direction is required. This criterion can be fulfilled by slip in <c + a>, or by twinning, although both of these require a greater resolved sheer stress to be activated than pure <a> deformation [70]. There are four twinning modes commonly observed in hcp titanium: two are activated by tension

along the c-axis: {10$\bar{1}$2} and {11$\bar{2}$1}, and two are activated under compression: {10$\bar{1}$1}and {11$\bar{2}$2} [71]. Some of the main deformation modes are shown in Fig. 2.7.

{10$\bar{1}$0} ⟨11$\bar{2}$0⟩	{10$\bar{1}$1} ⟨11$\bar{2}$3⟩	⟨10$\bar{1}$2⟩ ⟨10$\bar{1}$1⟩	{11$\bar{2}$2} ⟨11$\bar{2}$3⟩	{11$\bar{2}$1} ⟨11$\bar{2}$6⟩
Prismatic ⟨a⟩ slip	Pyramidal ⟨c+a⟩ slip	Tensile twin	Compressive twin	Tensile twin, type II
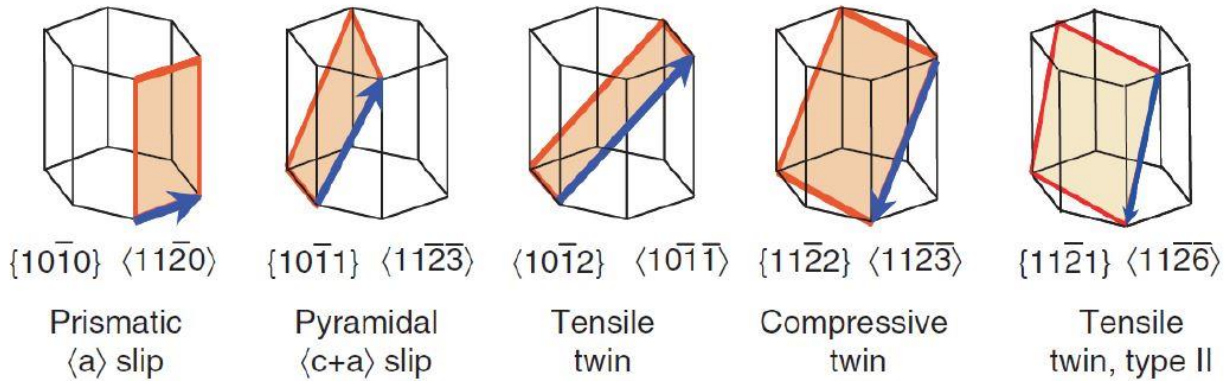
Fig. 2.7: A selection of some of the main deformation mechanisms observed in titanium alloys [72].

The deformation mechanism of most hcp metals can be generalized by their cation/ anion (c/a) ratio. As c/a ratio of α-Ti is below the ideal value of 1.633, slip most easily occurs on the prismatic planes although basal and pyramidal slip can also be activated [73].

Traditionally, twinning does not occur in Ti-6Al-4V alloy unless it is at very high strain rates or at cryogenic temperatures, when the critically resolved stress for deformation by slip is higher [74, 75]. High concentration of aluminum (*Al*) suppresses twinning [45] which is the reason behind it. However, twinning has more recently been observed at ambient temperature and low strain rates with deformations as small as only 6% strain [74]. Difficulty in distinguishing them from similarly orientated grains is the reason behind being missed by previous studies [76]. The dominating twin system stated in the literature, {10$\bar{1}$2} ⟨10$\bar{1}\bar{1}$⟩, is shown in Fig. 2.8.
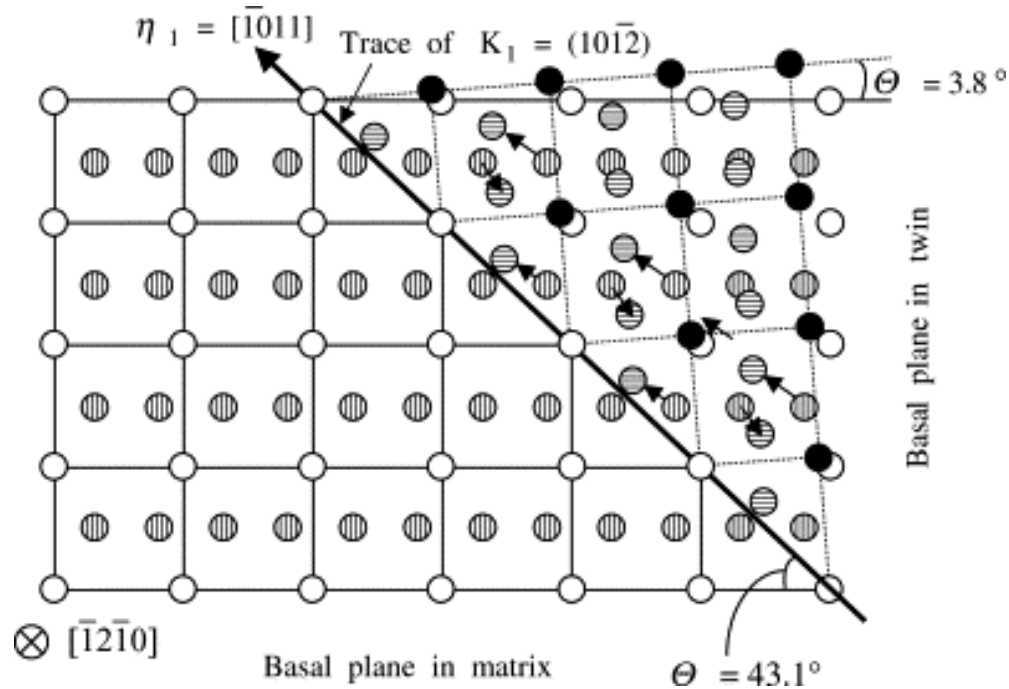
Fig. 2.8: Illustration of atom movements in {10-12} twin [77].

2.3. Additive Manufactured Ti-6Al-4V Alloy

2.3.1. L-PBF process

Laser-powder bed fusion (L-PBF) is an additive manufacturing (AM) technique used for fabricating metallic components from the ground-up [78]. In L-PBF process, a focused laser beam discriminately melts a thin bed of compacted powder material track-by-track and layer-by-layer to produce a solid part, typically within an inert atmosphere purged at a specific flow rate. A schematic representation of a L-PBF environment is shown in Fig. 2.9. L-PBF parts experience extremely localized temperature gradients and highly-dynamic heating/ cooling rates due to the high heat flux laser irradiation required for melting powder metal, resulting in relatively fast melting and solidification during their manufacture. Initial solidification and cooling rates directly affect the microstructure of built parts, hence knowledge of the solidifying melt pool behavior upon removal of the laser, including solid phase nucleation and dendritic growth, allows one to deduce initial microstructure phase and distribution. Due to cyclic, laser-induced conduction with previous layers, solid-state transformation, *i.e.* microstructural evolution continues at a longer time scale in L-PBF process. Both the single (*i.e.* sensible) and multi-phase (*i.e.* latent) heat transfer rates that occur during L-PBF depend on process parameters including laser power, laser beam size, and traverse speed. Other design parameters such as scan patterns, build orientation, powder size etc. can also affect resultant heat transfer.
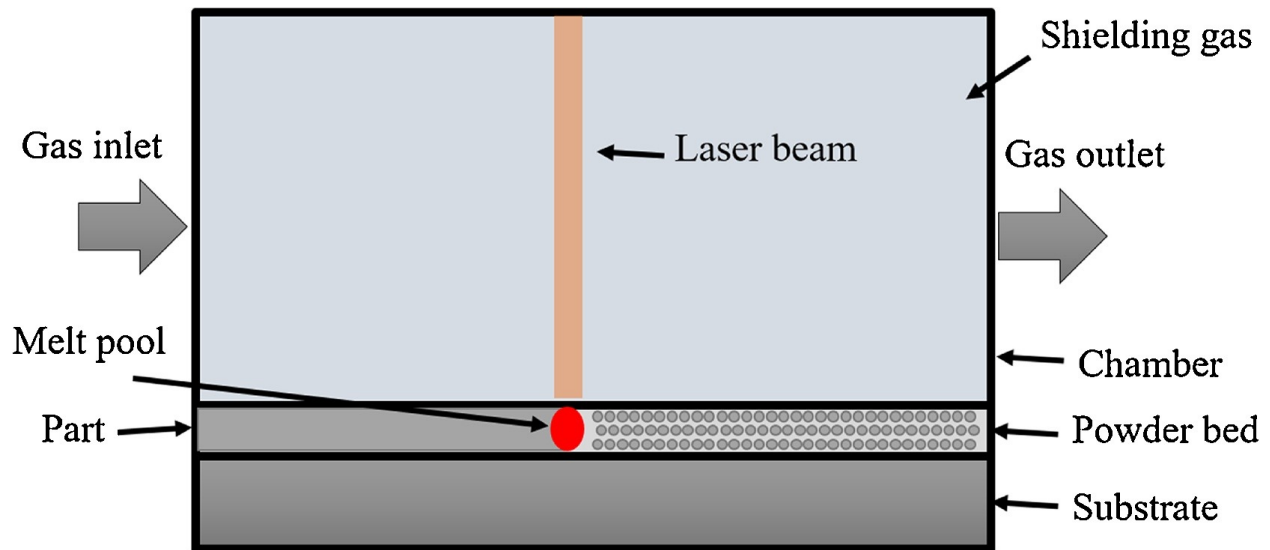
Fig. 2.9: Schematic representation of a typical L-PBF process consisting of a single moving laser beam, a chamber with shielding gas, powder bed, part and substrate [79].

During welding and laser-based AM processes inert shielding gas is employed to reduce oxide formation along part/powder surfaces, to protect the melt pool against contamination and to aid in expelling so-called 'spatter' debris. Effects of shielding gases on welding/AM processes and on final material quality have been studied in the literature. Ly *et al.* [80] investigated spatter generation during the L-PBF process via experimentation and found that the presence of flowing argon gas can decrease spatter significantly relative to when the process is performed in vacuum. Wang *et al.* [81] analyzed the effects of shielding gas during laser deep penetration welding and showed that the shielding gas can help stabilize the laser welding process via convection heat transfer and enhanced ionization–recombination. Philo *et al.* [82] performed the simulation of the flow within an L-PBF (Renishaw AM 250) chamber. They found that the flow atop the powder bed to be non-uniform and these flow non-uniformities increased spatter generation. Kah *et al.* [83] experimentally investigated the effects of various shielding gases on the microstructure and mechanical properties of different materials including steel and aluminum during welding. For austenitic stainless steels, they found that increasing the amount of nitrogen in the shielding gas can increase the ductility and improve the tensile strength, hardness, and pitting corrosion resistance of the final weld [83].

There are numerous instances that the L-PBF process may be numerically modeled and simulated using finite element (FE) methods [84–87]. These approaches have been studied with varying degrees of fidelity for understanding process-structure-property

relationships while minimizing the need for repetitious, costly experimentation. In general, a continuum or powder-scale method can be utilized, while the latter requiring significantly more computational resources. In powder-scale techniques [88, 89], thermos-fluidic phenomena, (such as melt pool fluid dynamics, melt pool wetting/ spreading/ wicking, powder distribution/ size effects, solidification and microstructural-coupling) can be more accurately modeled due to the L-PBF process being better represented. However, in most of the cases, such effects can be secondary or tertiary in nature relative to the impactful phenomena driven by the bulk temperature response of the participating media (*i.e.* powder, part, and substrate), for instances, cooling rates, temperature gradients, peak temperatures and others. In these studies, participating media was modeled as continua, and the effects of powder bed porosity was indirectly accounted for through use of effective bulk properties. The latent thermal energy transfer can be idealized and/ or incorporated into the model to model powder melting and melt pool solidification during L-PBF. The samples studied in this thesis were manufactured in single track directed L-PBF system with inert (argon) gas shielding as shown in the fig schematically and numerical modeling in Fig. 2.10 and Fig. 2.11
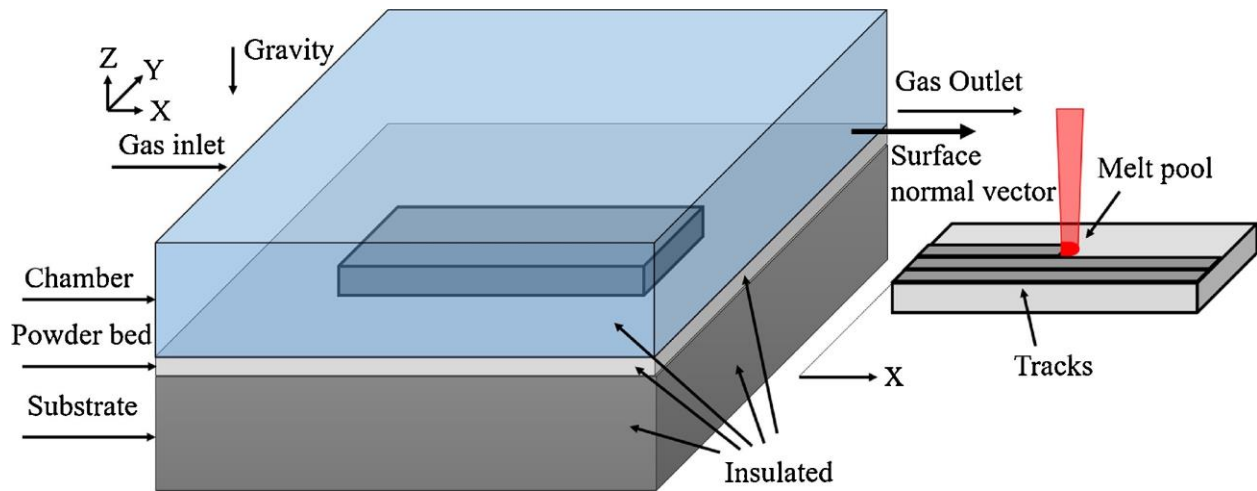
Fig. 2.10: Schematic representation of substrate, powder bed, solidified tracks, and chamber including coordinate axes [79].
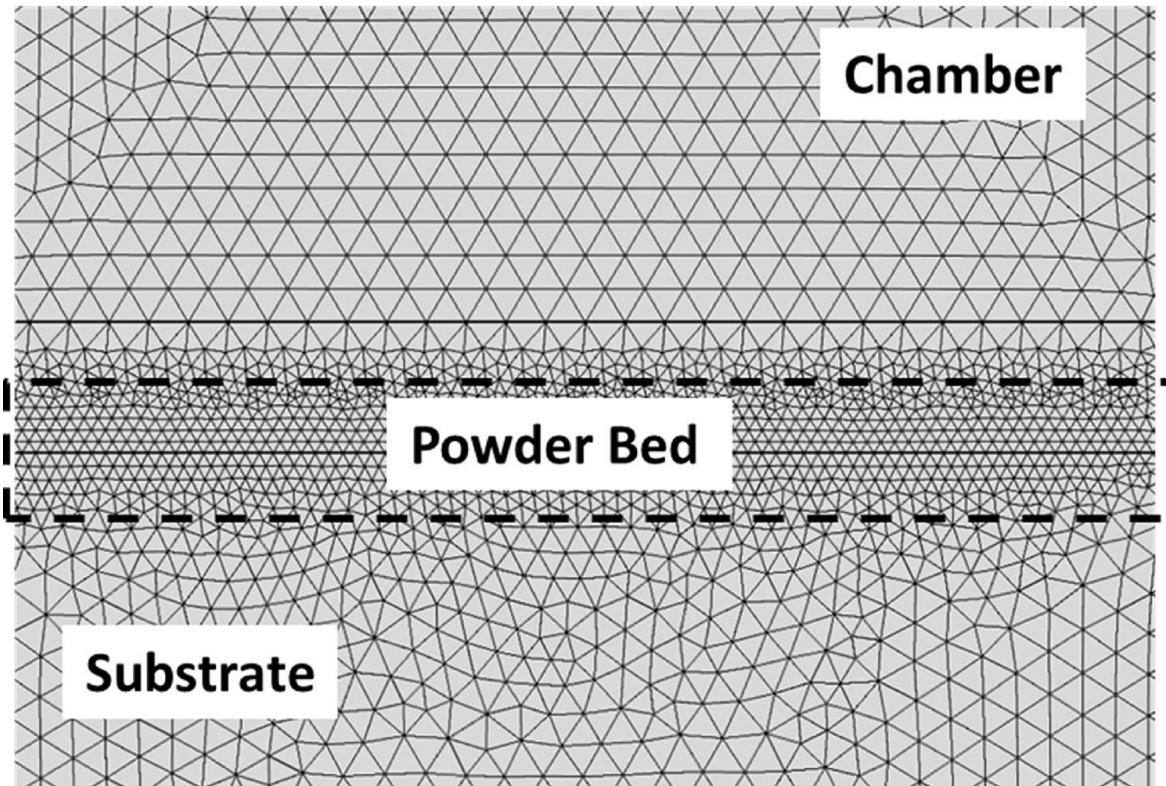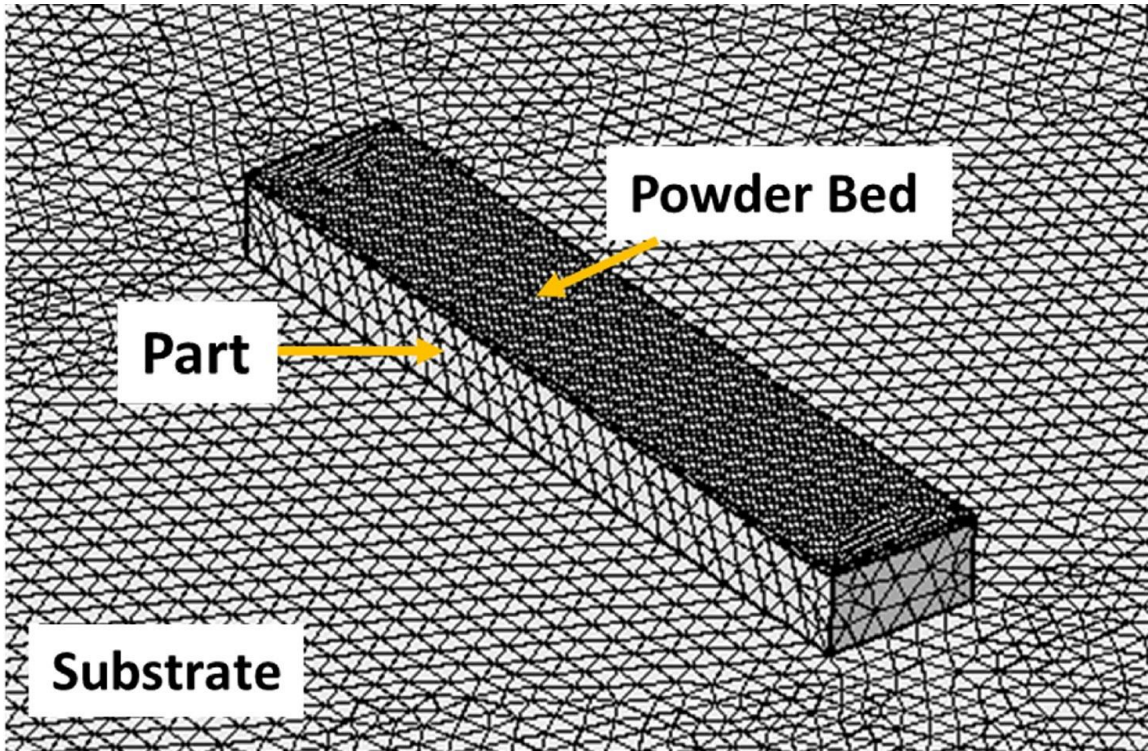
Fig. 2.11: (Top) isometric view of meshed powder bed, substrate and part (part height not to scale) and (bottom) side view of meshed substrate, powder bed and chamber of numerical modeling [79].

2.3.2. Columnar Prior β Macrostructure

The cooling rate in the AM is way faster than the one in the conventional manufacturing methods like forging. This directly affect the morphology, size, and distributions of the grains in the microstructure.

The most striking microstructure feature commonly observed in the AM Ti-6Al-4V alloy is large columnar prior β grains that can be often observed by naked eye and that can extend up to the entire height of the build. Columnar growth is observed with laser [68, 90], electron [91, 92], and arc [93] heat sources as shown in Fig. 2.12.
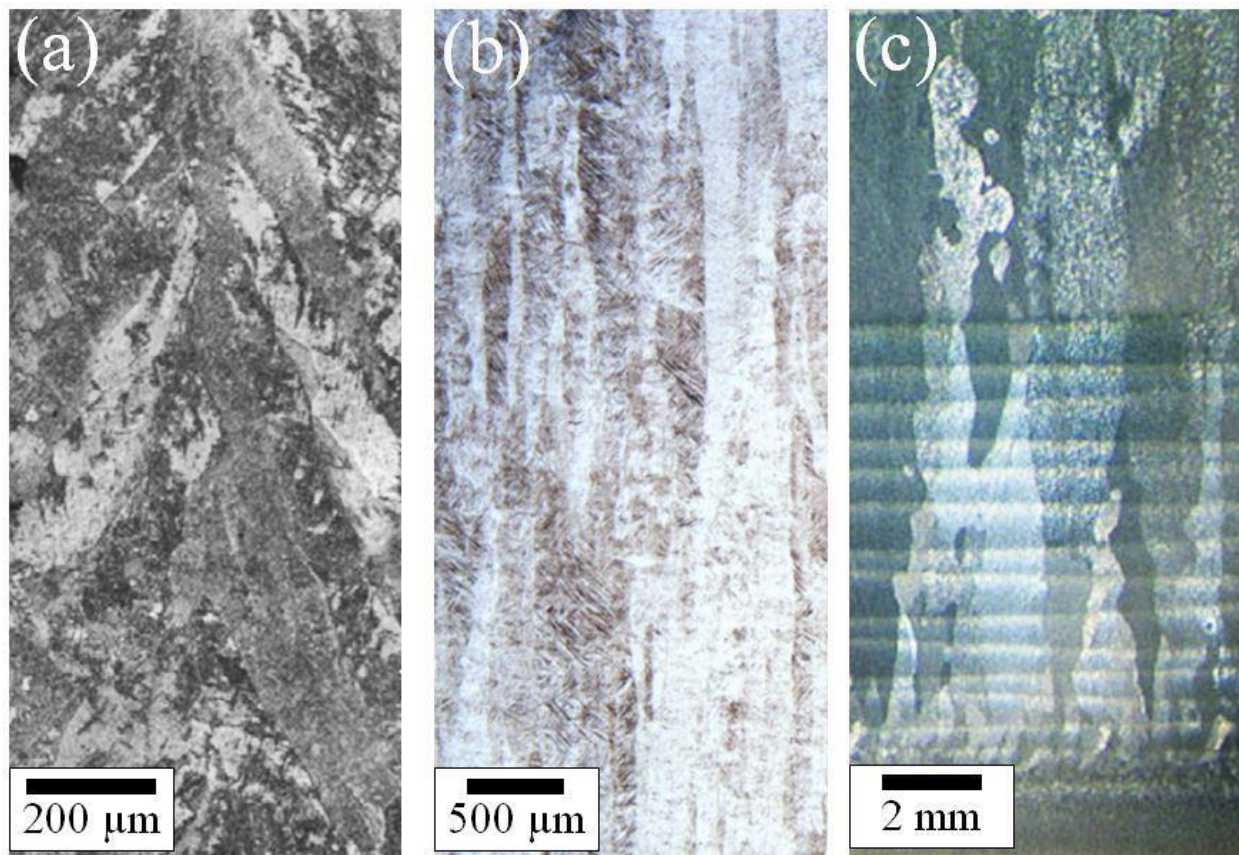
Fig. 2.12: Columnar prior β microstructures in: a) electron beam (SEBM) [91], b) laser beam (SLM) [94], and c) arc melted (WAAM) additive manufacturing processes [95].

The large prior β grains are formed as a result of the AM solidification conditions when combined with the phase relationships in Ti alloys. The steps that lead to the columnar structure shown in Fig. 2.13 starting from an equiaxed prior β substrate that at ambient temperature made up of an α lamella structure with retained β (Fig. 2.13 a). Irrespective of the feedstock, the heat source not only melts the material being deposited and some of the substrate material beneath it, but to a certain depth the substrate is raised to a

temperature above the β-transus, fully transforming it to the cubic β-phase (Fig. 2.13). This β phase returns to the orientation prior to transformation due to re-growth of the residual β retained between the laths. With the heat source moving on and the molten material begins to cool and solidify, the high thermal gradients in the melt pool and low solute partitioning in Ti *i.e.* there is insufficient super-cooling ahead of the solidification front to enable nucleation ahead of the growth front [84]. Moreover, owing to the high solubility of most elements including oxygen in Ti, there are few particles present in the melt for heterogeneous nuclei. Therefore, the molten material solidifies in epitaxial way on to the β grain beneath it at the fusion boundary, continuing the grain. This cycle is repeated with each time of the heat source as additional layers are deposited (Fig. 2.13), the thermal field returning the previously deposited material to the previous high temperature β structure, and the melt pool solidifying epitaxial way upon it. The coarse columnar structure develops through many layers as no nucleation occurs ahead of the solidification front. These orientations are able to out compete other less well aligned orientations, as the <001> growth directions are the 'easy growth directions' for bcc

structures [47], [96].
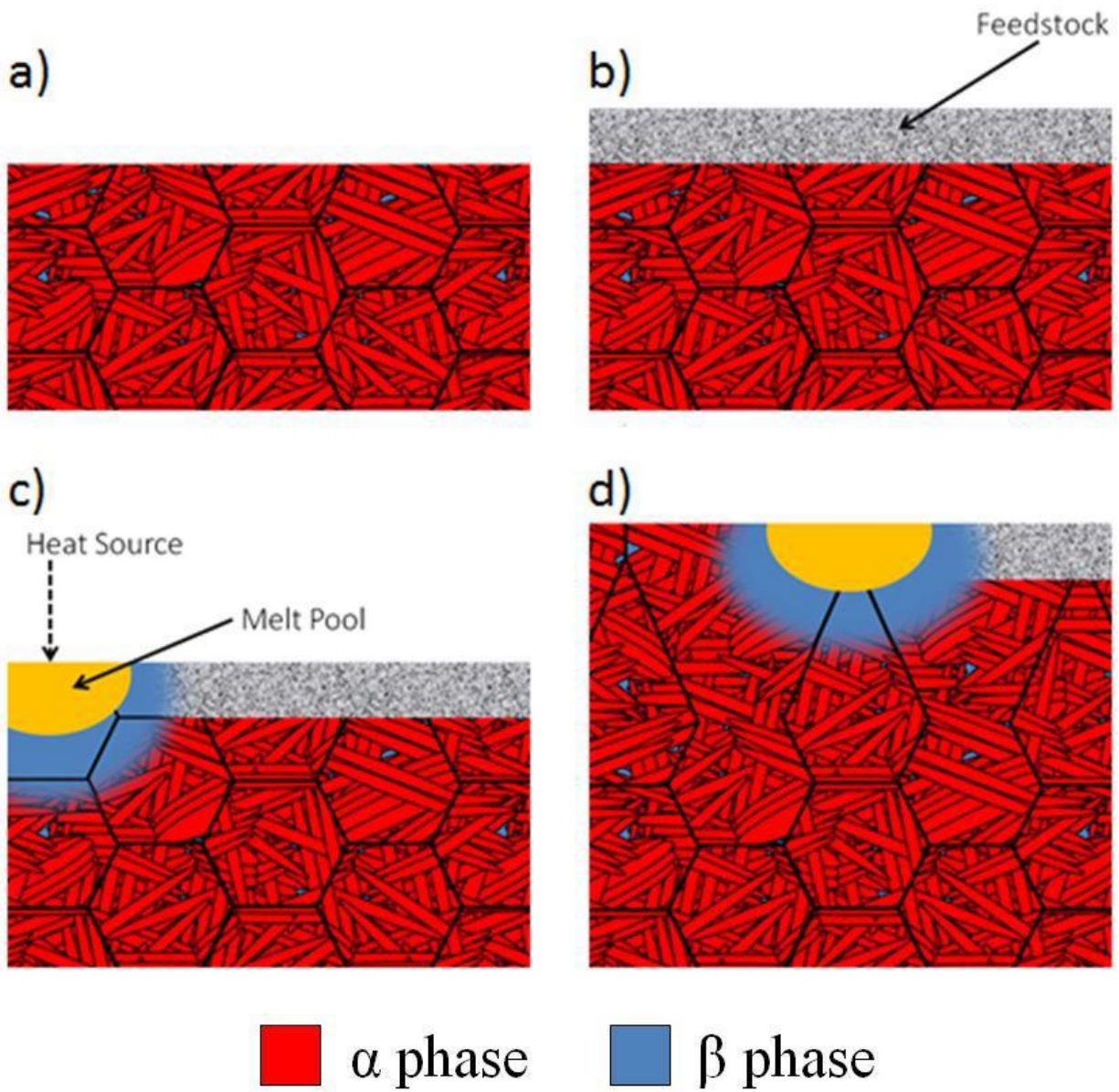
Fig.2.13: Schematic of the steps involved that lead to the coarse columnar prior β structure observed in Ti-6Al-4V AM builds: (a) an equiaxed prior β substrate, (b) addition of feedstock (in this case powder), (c) the heat source that melts the feedstock and underlying material, and heats the surrounding material into the β phase, and (d) with additional layers, prior β grains grow epitaxially through the build height, growing competitively [76].

2.3.3. α + β lamellar microstructure

The microstructure of Ti-6Al-4V is highly dependent on the cooling rate through the β transus. Although with most AM techniques no cooling is forcibly applied, but because of the small melt pool is cooled by conduction through the substrate and previously deposited material as it is sufficient to cool the material very quickly.
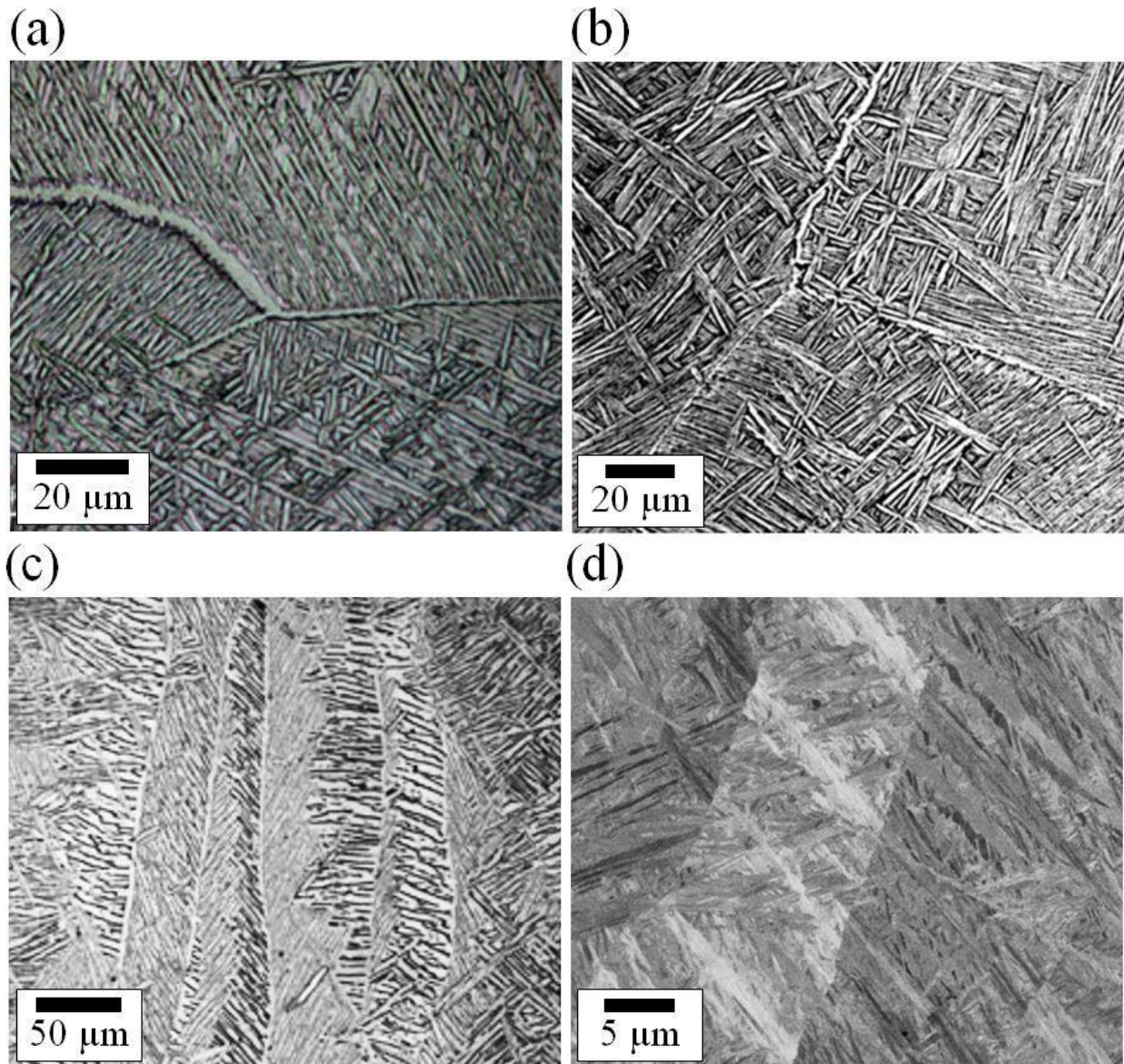
Fig. 2.14: Typical Ti-6Al-4V AM microstructures. (a) [95] & (b) [90] are typical α+β Widmanstätten microstructures generated in arc and laser blown powder based processes respectively. A typical microstructure of a heated powder bed process is given in (c) where diffusion has allowed a greater volume of β to be retained [47] and (d) α-martensitic microstructure generated by extreme cooling rates with SLM [59].

A fine layer of α' martensite has been observed in several studies at the top of AM Ti-6Al-4V alloy including WAAM [97] and EBM [47] resulting in the acicular sub-micron structure shown in Figure 2:14 (d). The formation of martensite in the top layer is not surprising since the final layer of deposition is not subsequently reheated into the β phase by the successive passes, and its cooling rate through the β transus is greater than for the rest of the build.

2.4. Instrumented Indentation

Great steps have been achieved over the past few years in the development of techniques for probing the mechanical properties of materials on the submicron level through the advancement of the development of instruments that continuously measure force and displacement [98–101]. The load-displacement data derived through indentation can be used to determine mechanical properties even when the indentations are too small to be imaged conveniently. The indentation positioning capacity of some of the instruments is in the submicron regime, hence, a way is available by which the mechanical properties of a surface can be mapped with submicron resolution with mechanical properties microprobe [102, 103].

The elastic modulus (E) and the hardness (H) are the two mechanical properties measured most frequently using load and depth sensing indentation techniques from data obtained through one complete cycle of loading and unloading [101]. According to a model for the deformation of an elastic half space by an elastic punch, the unloading data are then analyzed which relates the contact area at peak load to the elastic modulus. To provide separate measurements of E and H, methods for independently estimating the contact area from the indenter shape function are used.

In the late 19th century, Boussinesq [104, 105] and Hertz [106] originally considered the elastic contact problem, which plays a key role in the analysis procedure. For computing the stresses and displacements in an elastic body loaded by a rigid and axisymmetric indenter, Boussinesq developed a method based on potential theory which subsequently been used to derive solutions for a number of important geometries such as cylindrical and conical indenters [105, 107].

Tabor [108] performed the earliest experiments in which load and displacement sensing indentation methods were used to measure mechanical properties by studying the indentation of a number of metals deformed by hardened spherical indenters. Stillwell and Tabor performed a similar study to examine the behavior of conical indenters [109]. One particularly remarkable observation resulting from these studies concerns the shape

of the hardness impression after the indenter is unloaded and the material elastically recovers. Since elastic contact solutions exist for each of these geometries (*i.e.,* a spherical indenter in a spherical hole and a conical indenter in a conical hole), it was observed that the ways in which plasticity affects the interpretation of elastic unloading data can be dealt with by taking into account the shape of the perturbed surface in the elastic analysis. Using the obtained results Tabor showed that the shape of the entire unloading curve and the total amount of recovered displacement can be accurately related to the elastic modulus and the size of the contact impression for both spherical and conical indenters. Important observations found from these studies are: (a) the diameter of the contact impression of the indenter in the surface formed by conical indenters does not recover during unloading but the depth recovers; (b) the indenter must be loaded and unloaded a few times before the load displacement behavior becomes perfectly reversible *i.e.,* a limited amount of plasticity sometimes occurs in each of the first few loading and unloading recordings; and (c) effects of non-rigid indenters on the load (P)- displacement (h) behavior can be effectively accounted for by defining a reduced modulus, E_r, through the equation [99]:

$$\frac{1}{E_r} = \frac{(1-v^2)}{E} + \frac{(1-v_i^2)}{E_i}$$

(1)

Here, E and v are Young's modulus and Poisson's ratio respectively for the specimen and E_i and v_i are the same parameters for the indenter respectively.

In the early 1970, interest in load and displacement sensing indentation testing as an experimental tool for measuring elastic modulus began with the work of Bulychev, Alekhin, Shorshorov, and co-workers [110–112]. Instrumented microhardness testing machines was used to obtain indentation load-displacement data which was then analyzed according to the equation [99]:

$$S = \frac{dP}{dh} = \frac{2}{\sqrt{\pi}} E_r \sqrt{A}$$

(2)

Here, S (dP/dh) is the experimentally measured stiffness of the upper portion of the unloading data, E_r is the reduced modulus of elasticity, and A is the projected area of the elastic contact. The modulus of elasticity can be derived by measuring the initial unloading stiffness and assuming that the contact area is equal to the optically measured area of the hardness impression. Equation (2) is applicable for all types of indenter including spherical and cylindrical indenter [112, 113].

Doerner and Nix [101] put together ideas to produce the most comprehensive method to date for determining hardness and modulus from indentation load-displacement data. They proposed a simple empirical method based on extrapolating the initial linear portion of the unloading curve to zero load and using the extrapolated depth with the indenter shape function to determine the contact area which was later confirmed with finite element simulations of the indentation of silicon and nickel by conical indenters [114]. With the contact area so derived, the modulus can be computed from Eq. (2) and the hardness from its normal definition:

$$H = \frac{P_{max}}{A} \tag{3}$$

Here, H is hardness, P_{max} is the peak indentation load, and A is the projected area of the hardness impression.

For real material behavior, the above stated findings could not adequately explain the continuous change of contact area and stiffness which change immediately and continuously as the indenter is withdrawn [99]. Oliver and Pharr [99, 102], developed a new method for analyzing indentation load-displacement data which addresses these problems. They presented an analysis technique is which accounts for the curvature in the unloading data and provides a physically justifiable procedure for determining the depth that was used in conjunction with the indenter shape function to establish the contact area at peak load. The hardness and moduli of several materials were then calculated using the analysis and compared with values determined by independent means to establish the accuracy of the method. Moreover, several practical issues concerning procedures for taking data and methods for determining load frame compliance and indenter shape functions were also discussed by Oliver and Pharr [99]. In this research, creep parameters, residual stress measurement, and effect of post heat treatment analysis were performed using Oliver and Pharr method.

2.5. Creep

2.5.1. Introduction

Creep is a mechanical failure which is defined as time-dependent plastic deformation of materials subjected to a constant load or stress. However, In case of indentation creep behavior, from the variation of creep rate, a creep curve originating from the depth-sensing indentation is divided into two separate zones: transient creep and steady-state creep [115]. Unlike traditional uniaxial creep curves obtained from tension/ compression testing, depth-sensing indentation testing does not have a third stage, or accelerated

creep, as materials do not drastically fail under the indenter during indentation-based creep testing [116].
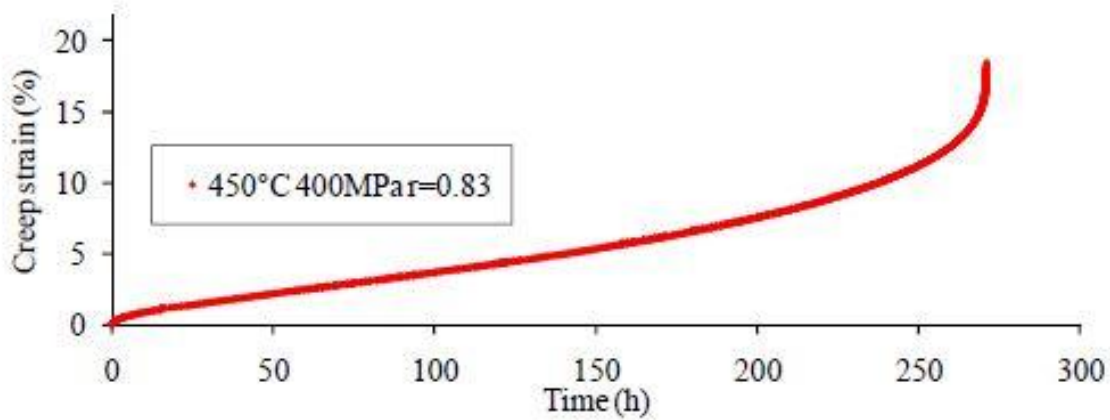
Fig. 2.15: General creep curve of Ti-6Al-4V alloy at 450⁰C [6].

Moreover, stress states and volume of material deformation are different in the uniaxial and instrumented indentation creep techniques; a tri-axial non-homogeneous stress state and a continually growing deformation volume underneath the indenter are two important features of the instrumented indentation testing approach.

2.5.2. Indentation Creep

Indentation creep can be defined as time dependent motion of a hard indenter into a solid under constant load and temperature [117]. This process saves both time and cost associated with manufacturing samples since only sample of small size is required. This technique is particularly advantageous for health hazardous radioactive nuclear materials since a large number of data could be generated on the same sample. Metallographically polished specimen surface is the only requirement for evaluation of indentation hardness and creep.

The methods for the measurement of time-dependent phenomena can be conveniently divided into two categories: (1) broad-band, quasistatic, or creep techniques: the load, stress, or strain rate is held constant for a period of time while measuring the response of the material; and (2) frequency-specific dynamic techniques: the load or stress is varied at a single frequency while measuring the response of the material. Though standard bulk-testing methods exist for these types of measurements, in many of today's technologies, the volume of material of interest may be on such a scale that these techniques become impractical. For specimens prepared in a form that allows testing with modified uniaxial techniques, these preparation processes are often tedious or may very

well alter those properties that are of interest. Indentation creep testing might be an alternate means for mechanical characterization (*i.e.* conventional creep testing).

There are instances of four types of tests being employed using depth-sensing indentation systems to gain insight into the relationship between indentation strain rate and hardness: indentation load relaxation (ILR) tests, [118, 119] constant rate of loading (CRL) tests, [120] constant-load indentation creep tests, [121–123] and impression creep tests [124]. Each of these tests have drawn analogies between hardness and flow strength, as well as between the uniaxial strain rate and the indentation strain rate, *i.e.* [123]:

$$H = C_1 \sigma \tag{4}$$

$$\dot{\varepsilon}_u = C_2 \dot{\varepsilon}_\iota \tag{5}$$

Here, H is the hardness of the material, σ is the stress, $\dot{\varepsilon}_u$ is the uniaxial strain rate, $\dot{\varepsilon}_\iota$ is the indentation strain rate, and C_1 and C_2 are constants.

In an indentation creep test, the dynamics of deformation are very different than those occurring in the previously described uniaxial creep test. The deformed volume of material under the indenter continually expands to encompass previously undeformed material. Since the material strains under the indenter, the material underneath the indenter is very much likely to form an expanding cavity with a hydrostatic core, where no deformation is occurring, and an expanding elastic/ plastic boundary. The creep process is dependent upon the rate at which the elastic/ plastic boundary can proceed into the material. Since the radius of the elastic/ plastic boundary is related to the radius of the indentation, the most appropriate definition for the indentation strain rate is defined as the instantaneous change in contact area divided by the instantaneous contact area ($\dot{A}/A$) and it is a direct measure of the progression of the elastic/ plastic boundary into the material. However, for a geometrically similar indenter ($i.e.\ similar\ \dot{h}/h$), the instantaneous displacement rate ($\dot{h}$) of the indenter divided by the instantaneous displacement (h) is simply related to $\dot{A}/A$, and the indentation strain rate has typically been defined as $\dot{h}/h$ [123].
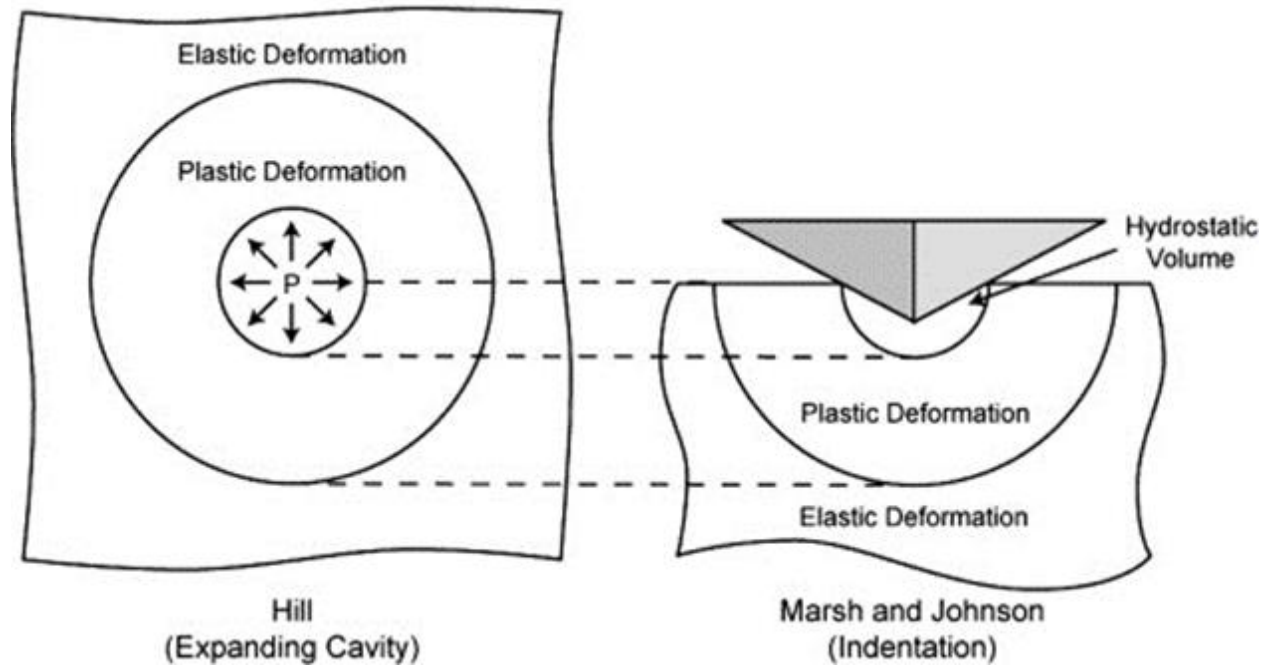
Fig. 2.16: Schematic representation of the deformation field under an indenter, as an expanding hemispherical volume subjected to hydrostatic pressure, as developed by Marsh [1] and Johnson [2].
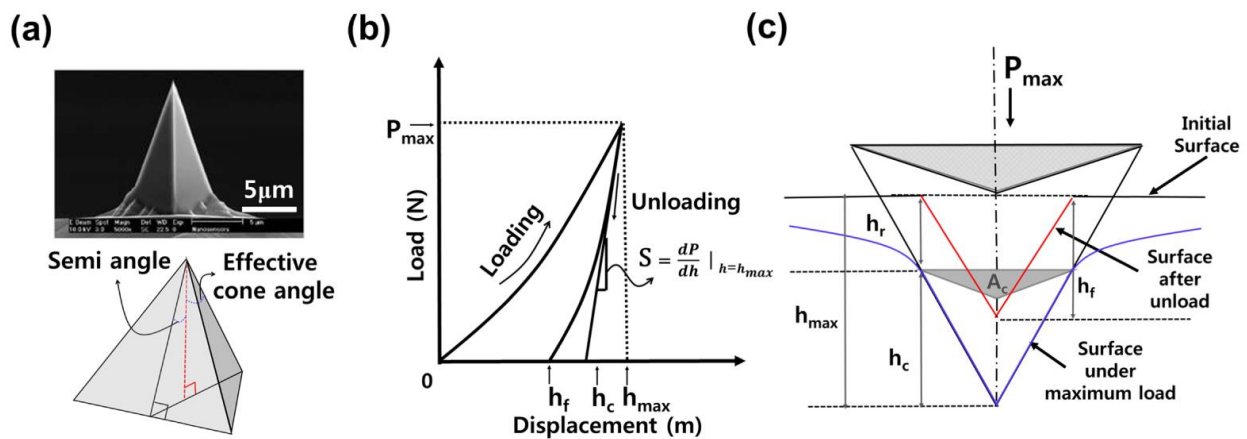
Fig. 2.17: (a) Scanning electron microscopy image of the indentation tip and geometrical definitions for evaluating tip coefficients (b) Schematic representation of the indentation curve of load-displacement and (c) surface profile behavior before and after indentation (h_{max}: maximum penetration depth, h_c: contact depth, h_f: final depth, h_r: residual depth, S: stiffness, P_{max}: maximum load, A_c: projected contact area) [3]

Though indentation creep testing is a viable technique for comparing the time-dependent properties of materials that cannot be characterized by standard bulk techniques, comparison of the indentation results to uniaxial creep data is a subject of major

importance. The prime difference between uniaxial testing and indentation testing lies in the geometry of the two tests. In general, in any mechanical tests, forces and displacements are controlled and/or measured depending upon the type of apparatus being used. However, the displacement response of a material to an applied force, on its own, tells nothing of the properties of the material without incorporating the geometry of the specimen. In conventional uniaxial testing, the geometry of the test is defined by the user. Specimens are typically geometrically simple like a cylindrical compression specimen or a dog-bone tensile specimen. In an indentation test, the geometry of the material is actually being controlled by the very properties of the material that are of interest like the hardness, Young's modulus, or strain-rate sensitivity. Typically, the test itself is designed to examine the properties that are of interest.

2.5.3. Creep in Ti Alloy

A number of researchers have used both nano/ micro-indentation technique and conventional methods (uniaxial tension) to assess rate-dependent plastic deformation in Ti and Ti alloys. Ma *et al.* [23] investigated room temperature creep behavior of Ti-10V-2Fe-3Al alloy with dual phase alloy based on dislocation mechanism by micro-indentation. It was found that power-law creep deformation was the controlling mechanism of creep in Ti-10V-2Fe-3Al alloy. Their results revealed that creep parameters exhibited significantly indentation depth dependent, at the secondary stage of creep, creep strain rate and creep rate increased with the increase of maximum indenter load, while creep stress and creep stress exponent showed an opposite trend. Kumar *et al.* studied creep-fatigue interactions in the Ti-6Al-4V alloy at ambient temperature using low cycle fatigue tests with and without hold times and found that the creep damage was responsible for a large reduction in life of the sample tested with hold time [24]. Matsunaga *et al.* investigated inter-granular deformation mechanisms by performing creep tests on polycrystalline Ti along with pure Mg and pure Zn at ambient temperature. They observed straightly aligned dislocation arrays in all of the specimens, although only one slip system was activated inside of each grain. Steady state creep rate around 10^{-9} s^{-1} and creep stress exponents (n) around 3.0 at ambient temperature were found [25]. Barboza *et al.* analyzed creep behavior of conventionally made Ti-6Al-4V alloy consisting Widmanst*ä*tten microstructure using conventional uniaxial test and found different creep stress exponents as 4.4 and 4.1 at 500 °C and 600 °C [27]. Creep strain rates of the conventional Ti–6Al–4V alloy were found lower than those of the α-Ti and composites. Kral *et al.* [8] analyzed uniaxial constant stress compression and constant load tensile creep tests in conventionally manufactured ultrafine-grained Ti-6Al-4V alloy at elevated temperatures compared it with ambient-temperature indentation creep. They found that

the results of the uniaxial creep tests showing the minimum creep rates of the Ultra Fine Grained (UFG) specimens were significantly higher in comparison with those of the Coarse Grained (CG) state. However, the differences in the minimum creep rates of both states of alloy greatly decrease with increasing values of applied stress. The CG alloy exhibited superior creep resistance than the UFG one over the stress range used. Badea *et al*. [6] analyzed creep behavior of hot-forged Ti-6Al-4V alloy and compared the creep stress exponent and activation energy at different temperature ranges from 450^0C to 600^0C under applied stresses ranging from 100 MPa to 500 MPa. For all the creep conditions, as the temperature increased, fracture surfaces exhibited ductile rupture characteristics, with a more pronounced necking, deeper voids and larger void diameters. Gollapudi *et al.* [125] studied the stress and temperature dependence of the transient creep strain and transient time of Ti-834 alloy, *i.e.* Ti–5.8Al–4.0Sn–3.5Zr–0.7Nb–0.5Mo–0.35Si–0.06C (in wt%) to understand the rate controlling mechanism of transient creep. Oliveira *et al.* [126] investigated the short-time creep behavior of Ti-6Al-4V by plasma carburizing under a constant tensile load in air at 600 °C using a dead-weight-creep-rupture machine and found that the creep properties of the "Widmanstätten + carburized" specimens were improved relative to those of untreated specimens. Es-Souni [4] conducted research on the high-temperature near α-Ti alloy Ti–5.8Al–4.0Sn–3.5Zr–0.7Nb–0.35Si–0.06C (Timetal 834) in order to further understanding of creep mechanisms and how they are affected by microstructure and alloying effects. He provided evidence to support the idea that at the stress and temperature range (500 ^{0}C to 625 ^{0}C) investigated, creep is controlled by bow-out and climb of dislocation segments pinned at lath boundaries and second-phase particle.
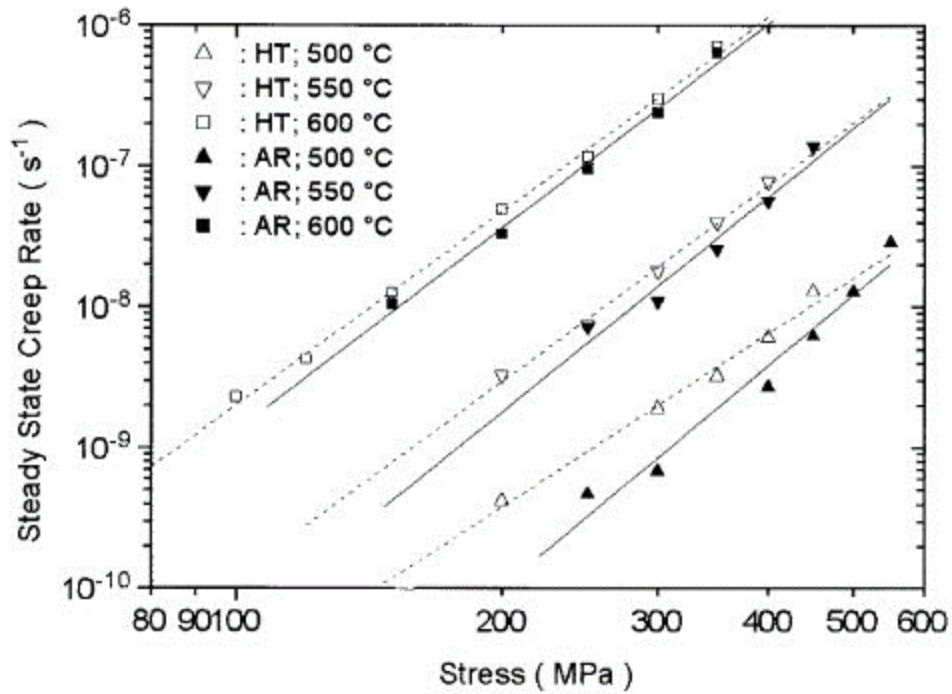
Fig. 2.18: Stress dependence of the steady-state creep rate for the microstructures investigated at different temperatures (HT= heat treated, AR= as received) [4].

Ziaja *et al* [5] performed Finite Element Analyses (FEM) by modelling primary creep behavior of two-phase titanium alloy Ti-6Al-2Mo-2Cr (VT3-1) at elevated temperature with various microstructure.

Evans *et al* [127] studied secondary creep behavior of two α/β titanium alloys (IMI318 and IMI685) at elevated temperature. Moreover, at higher stresses, Ti alloys can sometimes demonstrate unusually high creep stress exponent values, such as n > 15 [6, 127].
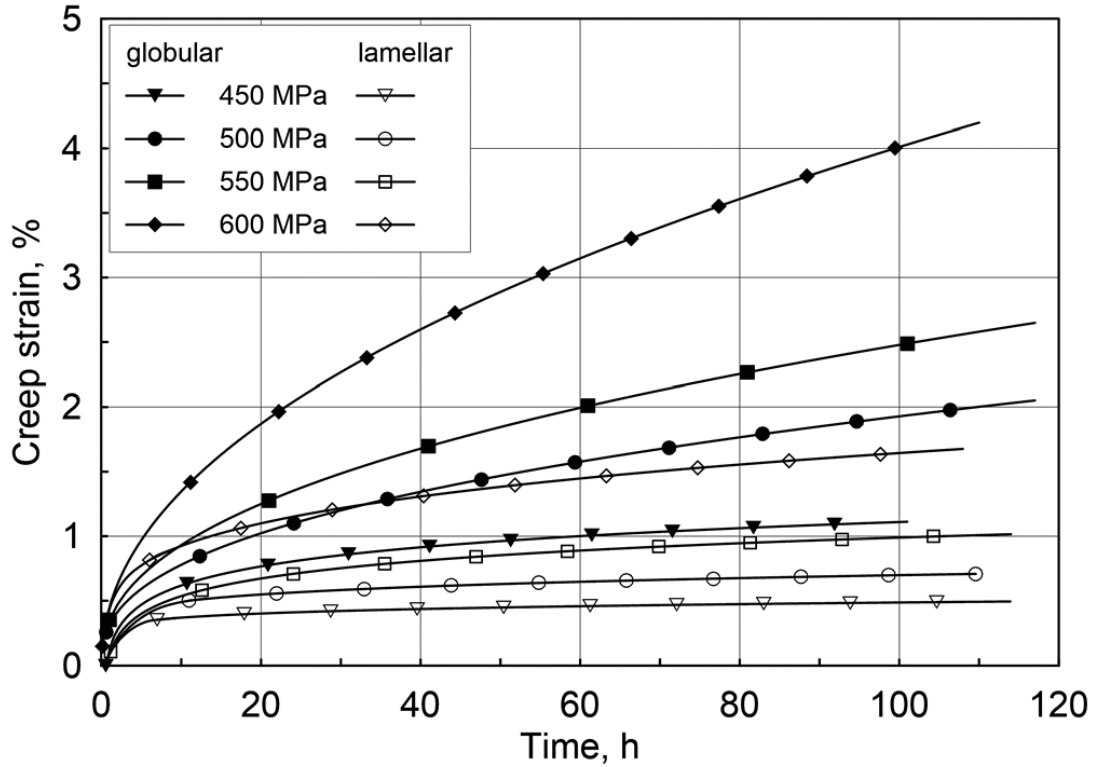
Fig. 2.19: Primary creep curves of Ti-6Al-2Mo-2Cr alloy (VT3-1) with lamellar and globular microstructure at 450°C [5].
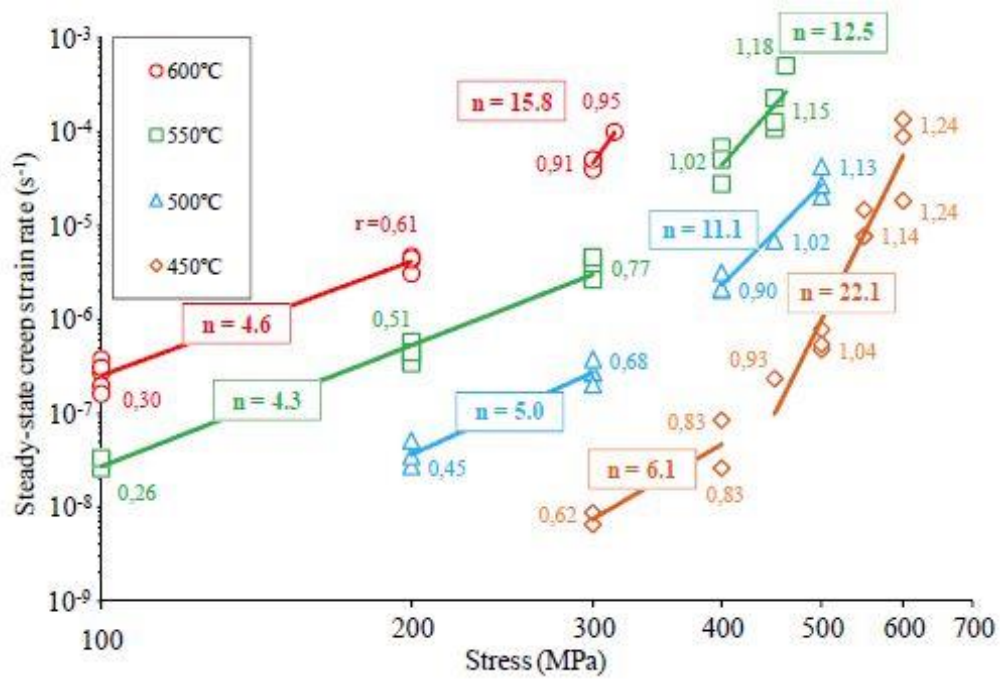
Fig. 2.20: Dependence of steady-state creep rate on applied stress at 500°C and 600°C along with unusual high value of 'n' [6].

2.5.4. Ambient Temperature Creep in Ti-6Al-4V Alloy

It has been reported in numerous literature that the ambient-temperature creep[2] occurs in $\alpha+\beta$ Ti–6Al–4V [40, 128]. In general, the HCP crystalline structure of the Ti-6Al-4V alloy is responsible for the ambient-temperature creep [7, 28]. That is, in the hcp structure, during ambient temperature creep, only one slip system is activated which is due to the low symmetric structure, generating low work hardening. As a result, deformation proceeds at ambient temperature and under stresses below the yield stress [7, 28].

Kameyama *et al*. [7] analyzed the suppressing effect of ambient-temperature creep of CP-Ti by cold-rolling at ambient temperature and compared with as received samples. They found that with increasing the thickness reduction, the twin, dislocation density and $\sigma_{0.2}$ increased but at the same time, the steady-state creep rates under the applied stress for constant $\sigma/\sigma_{0.2}$ were decreased.
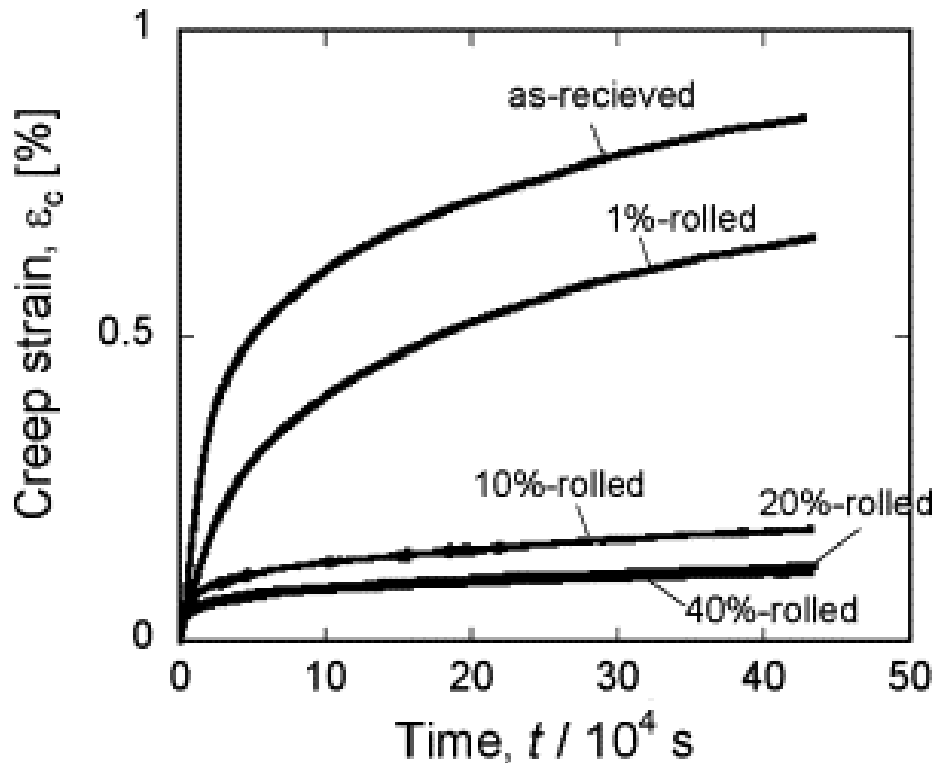
Fig. 2.21: Creep curves of the various CP-Ti samples at ambient temperature under the applied stress of $0.8\sigma_{0.2}$ [7]

Imam *et al*. [129] found an appreciable amount of creep conventionally built Ti-6Al-4V alloy at room temperature through uniaxial loading. Hasija *et al*. developed an experimentally validated computational model for Ti-6Al alloys accounting for plastic

---

2 Ambient-temperature creep occurs below 0.3–0.4Tm for hcp metals.

anisotropy and analyzed time-dependent plasticity for analyzing creep [26]. They observed cold creep to be the dominant mode of deformation in Ti alloys at low temperatures, where significant strains can accumulate with time. Kral *et al* [8] examined creep behavior of conventionally built Ti-6Al-4V alloy and compared it with the instrumented indentation creep tests at ambient temperature and found that annealing had little effect on the creep behavior in UFG Ti alloy at ambient temperature.
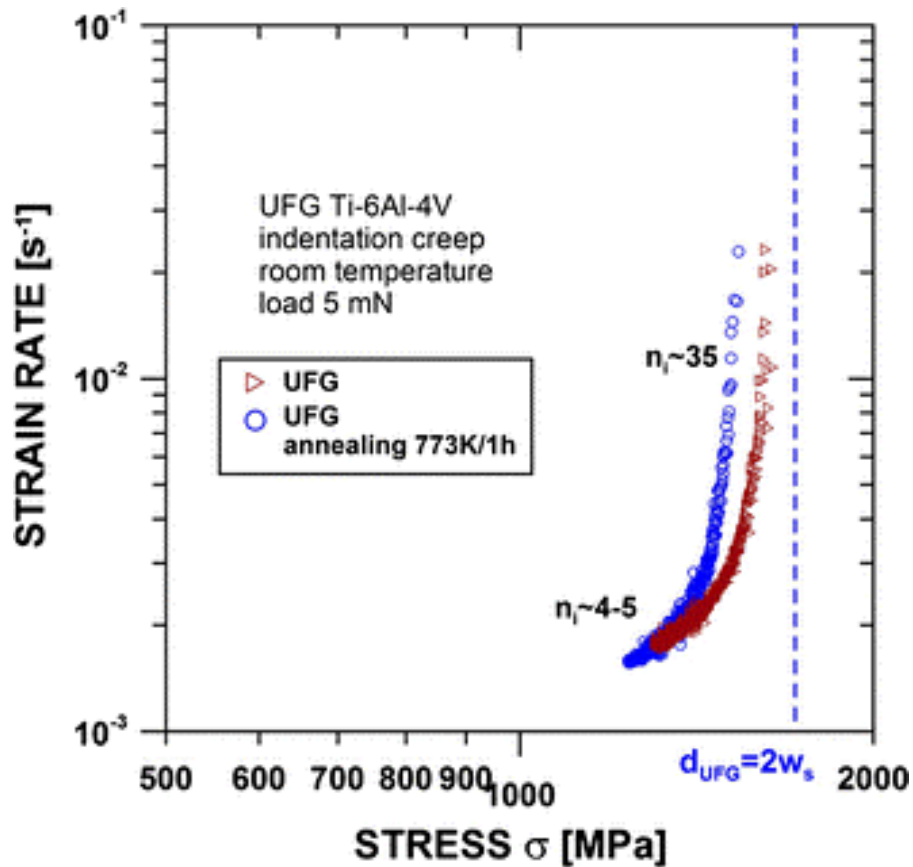
Fig. 2.22: Dependence of indentation strain rate versus applied stress for Ti–6Al–4V in the UFG and annealed state measured at room temperature under constant load 5 mN [8].

Harrison *et al.* [29] developed a model to study creep of Ti-6Al-4V by time dependent strain accumulation generated by dwell time fatigue effects at ambient "cold" temperature creep. The phenomenon of ambient temperature (or logarithmic) creep is not unusual in many materials including pure Ti and Ti alloys [30–32].

Evans [30] stated that the key factor in low-temperature (*i.e.* ambient temperature) creep sensitivity of Ti alloys (including Ti-6Al-4V alloy) is strong tendency of Ti in time-dependent strain accumulation at low temperatures. According to the design criteria, the

stress levels that impose the mentioned strain accumulations, are normally in the acceptable (safe) range. To this end, understanding the nature of creep sensitivity could be a challenging task but provides a foundation for understanding on crack development in $\alpha + \beta$ Ti alloys. For instance, room-temperature creep in the Ti-6Al-4V alloy fuel tanks and fasteners has been reported in the literature [25].

2.6. Heat Treatment of AM Ti-6Al-4V Alloy

2.6.1. Introduction

With regard to basic characteristics of titanium alloy including the equilibrium phase diagram, physical and metallurgical properties, heat treatment process and metallographic structure, there are a lot of useful data can be acquired for reference. A variety of microstructures can be tailored by simple thermo-mechanical treatments on this $\alpha + \beta$ alloy. Therefore, it is necessary to assess the effect of various heat treatment on microstructure and micromechanical properties of additively manufactured Ti-6Al-4V alloy.

2.6.2. Heat treatment of Ti alloys

Effect of heat treatment on microstructure and micromechanical properties of conventionally build Ti alloys has been reported in numerous literature. Seshacharyulu *et al.* [130] studied the hot deformation behavior of extra-low interstitial (ELI) grade Ti–6Al–4V alloy with Widmanstätten preform microstructure over wide temperature (750–1100°C) and strain rate ranges (0.001–100 s^{-1}) with the help of processing maps and the material exhibited cracking at prior β grain boundaries when deformed at lower temperatures (<800°C) and slower strain rates (<0.1 s^{-1}). Naughton *et al.* [131] have conducted experiments for the strain rate sensitivity index (*m)* for the Ti–6Al–4V ELI grade wire alloy at the temperatures ranging from 750^{0}C to 1050°C to determine superplastic forming capabilities.

Venkatesh *et al*. [9] evaluated the strain rate sensitivity and the strain hardening exponent of the Ti–6Al–4V ELI alloy subjected to different heat treatment conditions with and without the thermal oxide layer. Although the as-received Ti–6Al–4V ELI alloy consisted of primary α and $\alpha + \beta$ phases, they found that after air cooling and aging (AC + aging), the microstructure became a mixture of acicular α and β with primary α. After water quenching and aging (WQ + aging), they observed that the microstructure consisted of primary α and $\alpha' + \beta$ plus some fine secondary α phase in the β phase.

Zhang *et al.* [132] noted that for Ti–6Al–4V alloy, the formation of martensite transformed from β phase at 955°C is due to the fast cooling rate during water quenching. It was explained by them that phase transformation occurs from the high temperature β-Ti to low temperature α-Ti (diffusion controlled when slow cooling) or α′-Ti (shear dominated when rapid cooling). This explanation was in agreement with the microstructure described by Donachie [133]. Jovanovic *et al.* [134] also found a similar microstructure after heat treatment at 950°C followed by water quenching for Ti–6Al–4V alloy.
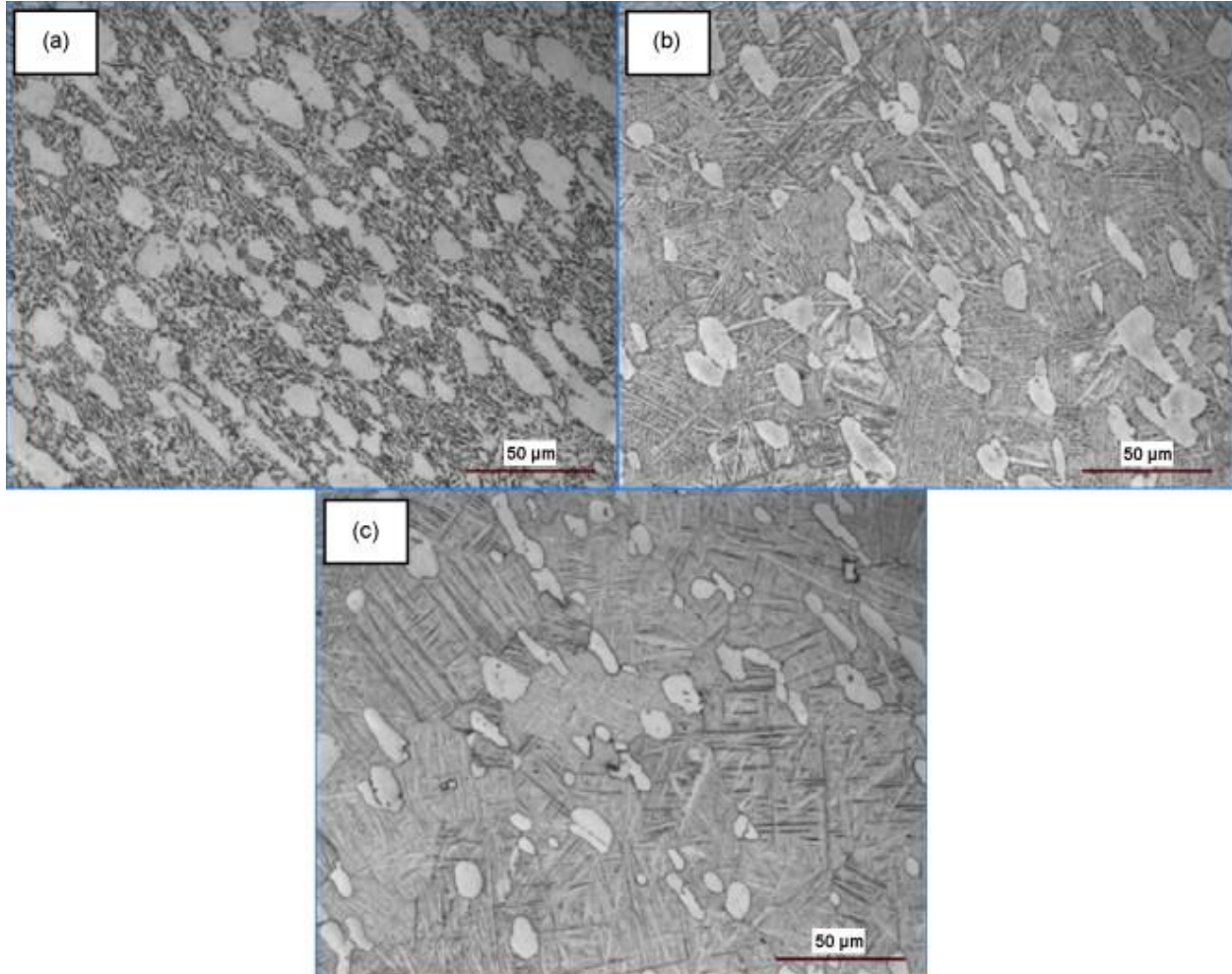
Fig. 2.23: Microstructures of Ti–6Al–4V ELI alloy studied by Venkatesh *et al.* [9] in different conditions, (a) as-received, (b) air cooling plus aging (AC + aging), and (c) water quenching plus aging (WQ + aging).

Venkatesh *et al.* [9] also stated that both WQ + aging and AC + aging heat treatment procedures led to an effective surface hardening arising from the formation of an oxidized layer of about 0.15 mm in depth. Although the AC + aging moderately increased the interior hardness, the WQ + aging significantly increased the internal hardness by

about 50% due to the formation of martensite. However, the formed surface layer seemed to have no effect on the yield strength (YS) and only have a slight decrease in the ultimate tensile strength (UTS), although they observed a certain reduction in the ductility.

Their obtained micro-hardness profile is shown in Fig. 2.24. It was observed that the highest hardness value occurred at the surface of the specimens, indicating that the surface has effectively been hardened. The specimen which was subjected to water quenching followed by aging (WQ + aging) exhibited much higher hardness values, while the as-received specimen had the lowest hardness out of the three conditions considered in this study. This was supported in accordance with the results obtained by Jovanovic *et al.* [134] for Ti–6Al–4V alloy. In general, the hardness increases as the rate of cooling increases due to the formation of martensite arising from rapid cooling [132, 133, 135]. The hardness of the sample subjected to air cooling followed by aging (AC + aging) lied in-between those of the WQ + aging and as-received specimens. From Fig. 2.23, it is clear that the size of the acicular α is relatively large in the AC + aging condition, when compared to the WQ + aging microstructure which has thin α' plates.
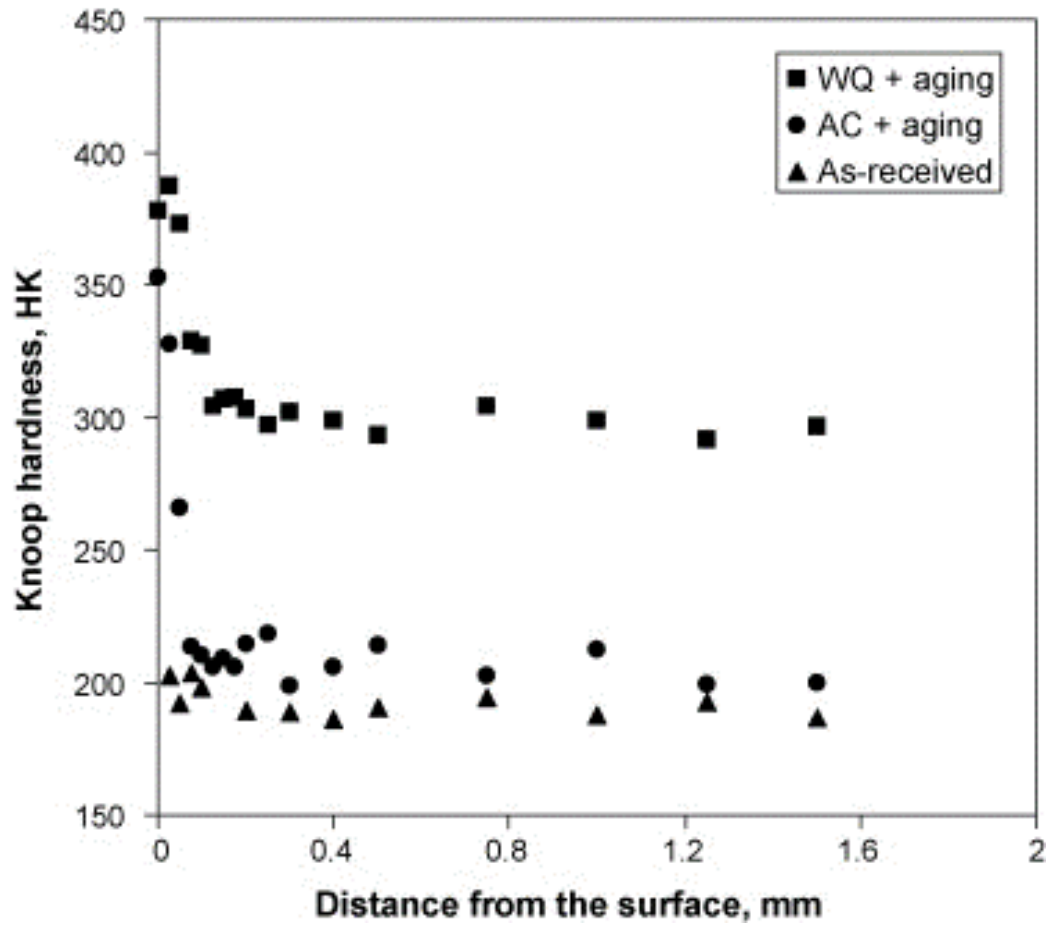
Fig. 2.24: Knoop microhardness profile of the Ti–6Al–4V ELI alloy in three conditions studied by Venkatesh *et al* [9].
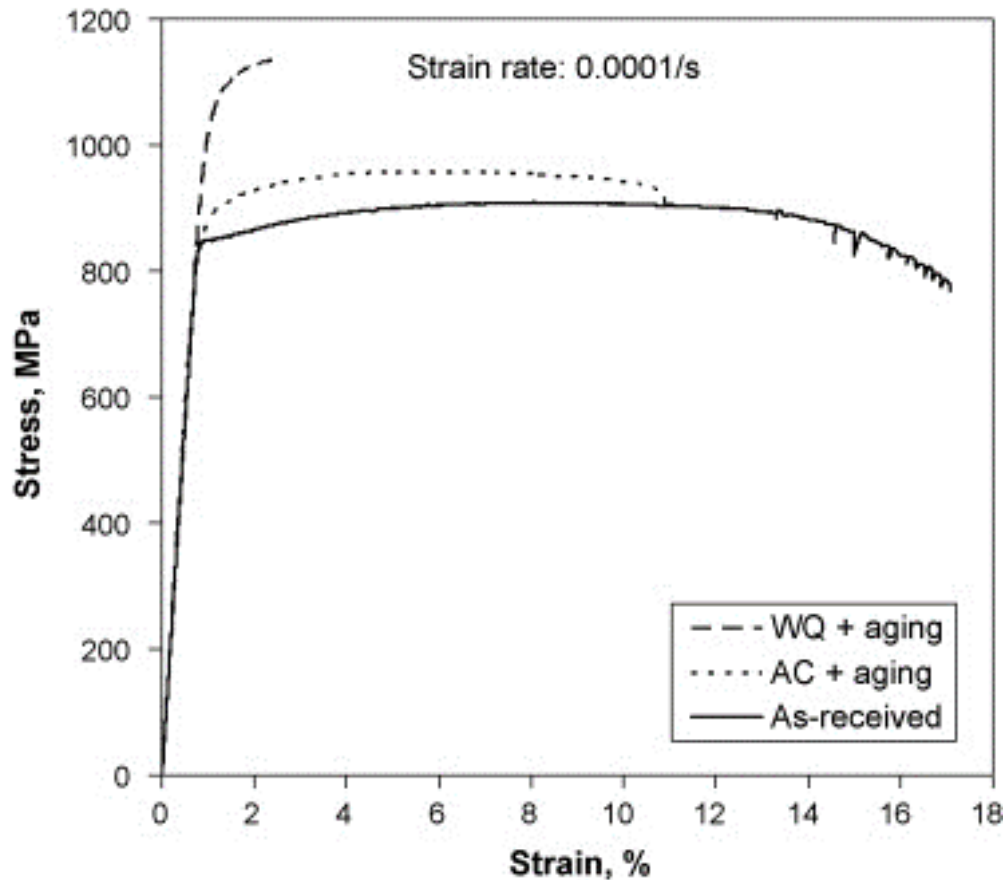
Fig. 2.25: Stress–strain curves of Ti–6Al–4V ELI alloy in different conditions tested at a strain rate of 0.0001 s^{-1} showing the comparison of ductility of different types of heat treated Ti-6Al-4V alloy by Venkatesh *et al.* [9].

2.6.3. Heat treatment of additively manufactured Ti-6Al-4V alloy

Although L-PBF process offers several advantages compared to conventionally built Ti-6Al-4V, the unique conditions during L-PBF conditions arouses certain problems. Due to short interaction times and accompanying highly localized heat input, large thermal gradients exist during the process. These results in build-up of thermal stresses, while the rapid solidification leads to segregation phenomena and the development of non-equilibrium phases. In addition, non-optimal scan parameters may cause melt pool instabilities during the process, leading to an increased porosity and a higher surface roughness.

Vrancken *et al.* [10] performed optimization of mechanical properties of Ti-6Al-4V alloy via heat treatment of parts produced by Selective Laser Melting (SLM). After 2 h at 780 °C, followed by FC, the fine martensitic structure has been transformed to a mixture of α and β, in which the α phase is present as fine needles (Fig. 2.26a).

41
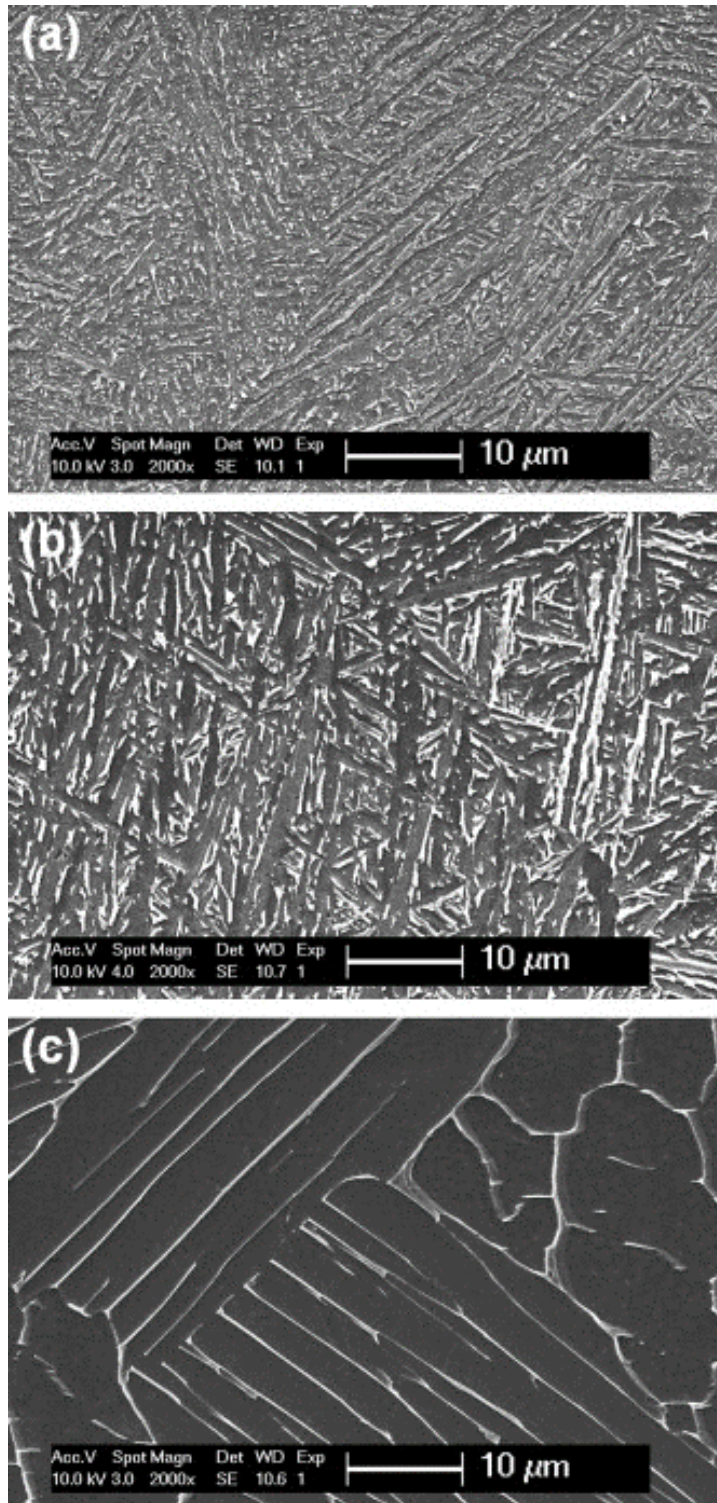
Fig. 2.26: Microstructure of Ti-6Al-4V studied by Vrancken *et al.* [10] produced by SLM after heat treating at different temperatures for 2 h, followed by FC. (a) 780 °C and (b) 843 °C below the β transus, (c) 1015 °C above the β transus. Lighter zones are β phase, the dark phase is the α phase.

Fig. 2.27 (a) shows the side view of SLM material after a heat treatment performed by Vrancken *et al.* [10] at 940 °C, followed by WQ, below the β transus. After conducting heat treatment below the β transus and at sufficiently low cooling rates, the prior β grains are became even more visible due to the formation of a layer of grain boundary α and the more aggressive etching of the $\alpha + \beta$ mixture as opposed to the original α'. However, Fig. 2.27 (b) shows that the microstructure no longer contains long columnar prior β grains after treatment above the β transus, indicating extensive grain growth of the SLM material when heated above the β transus, up to the point of semi-equiaxed βgrains. Results found by Studies of Sercombe *et al.* [37] Vilaro *et al.* [38] are in agreement about this microstructural transformation.
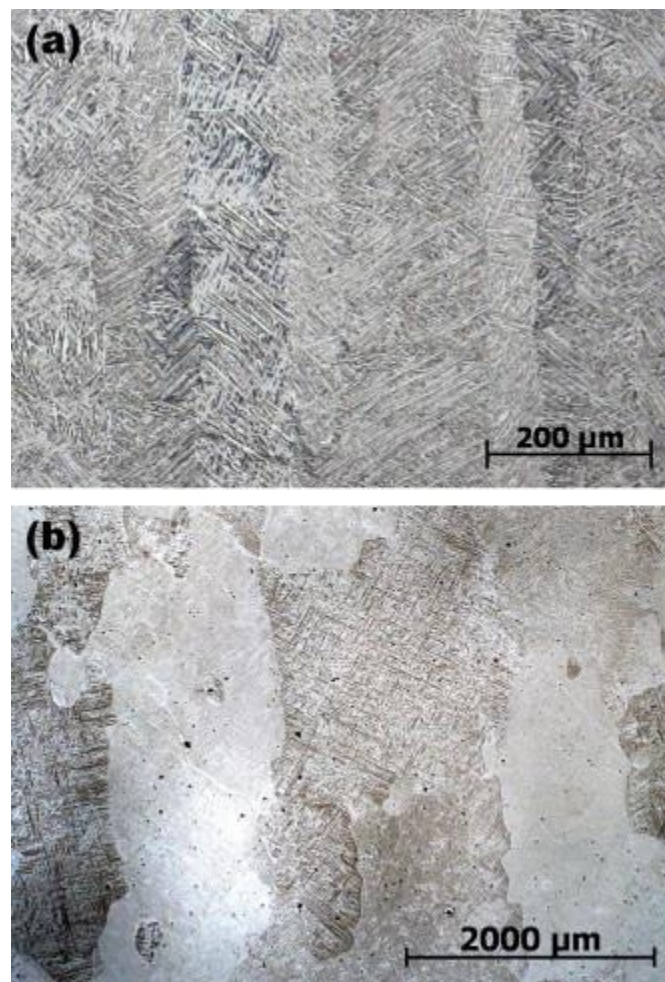
Fig. 2.27: Side view of study of SLM material by Vrancken *et al.* [10] (a) after 1 h at 940 °C followed by 2 h at 650°C, illustrating the long columnar prior β grains. After heat treatment, a lamellar mixture of α and β is present inside the columnar prior β grains. (b) After 1015°C, 2 h, followed by WQ, indicating the extensive growth of the columnar grains. Due to the WQ, the microstructure is fully martensitic.

Vrancken *et al.* [10] also found that, as the equilibrium fraction of β phase rises at high temperatures, the intergranular β phase in the reference material grows into equiaxed grains. Upon cooling, these β grains transformed to lamellar $\alpha + \beta$, resulting in a duplex microstructure, seen in Fig. 2.28. Their obtained microstructure consisted of equiaxed α grains and lamellar transformed β grains. At higher heat treatment temperatures, the higher equilibrium volume fraction of β phase ultimately leads to a higher fraction of lamellar $\alpha + \beta$ at room temperature. While heating above the β transus, grain growth of the β phase can take place leading to large grains.
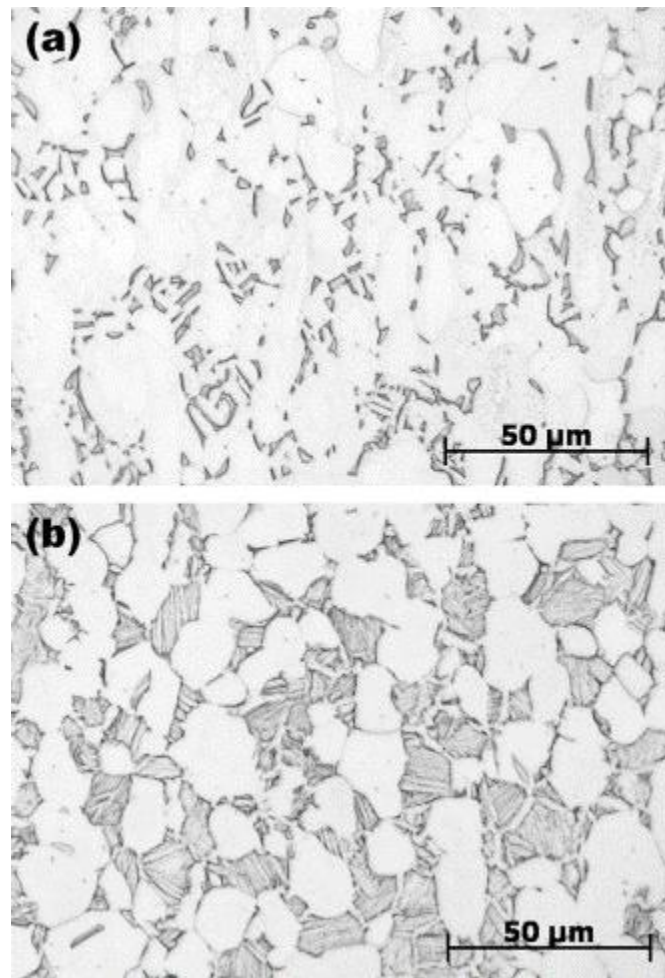
Fig. 2.28: (a) Heat treated SLM Ti-6Al-4V for 2 h at 780°C, followed by furnace cooling and (b) 1 h at 940°C, followed by air cooling to 650°C. The α phase is light, the β phase is dark. Increase in lamellar fraction when treated at a higher maximum temperature observed by Vrancken *et al.* [10].

Due to the specific microstructure resulting from the L-PBF process, to obtain optimal mechanical properties specific treatments are required. The microstructure of Ti-6Al-4V alloy processed by L-PBF consists of a fine acicular martensite called the α' phase [136, 137]. Mechanical properties of these L-PBF Ti-6Al-4V parts are a high yield stress (about 1 GPa), a high ultimate tensile strength but a relatively low ductility (less than 10%) as shown in Fig. 2.29. To achieve a variety of desired mechanical properties for specific applications, and to improve the ductility of Ti-6Al-4V alloy products manufactured by L-PBF, suitable post-production heat treatments must be elaborated. In addition, these treatments allow the reduction of thermal stresses that have been built up during the additive manufacturing process.
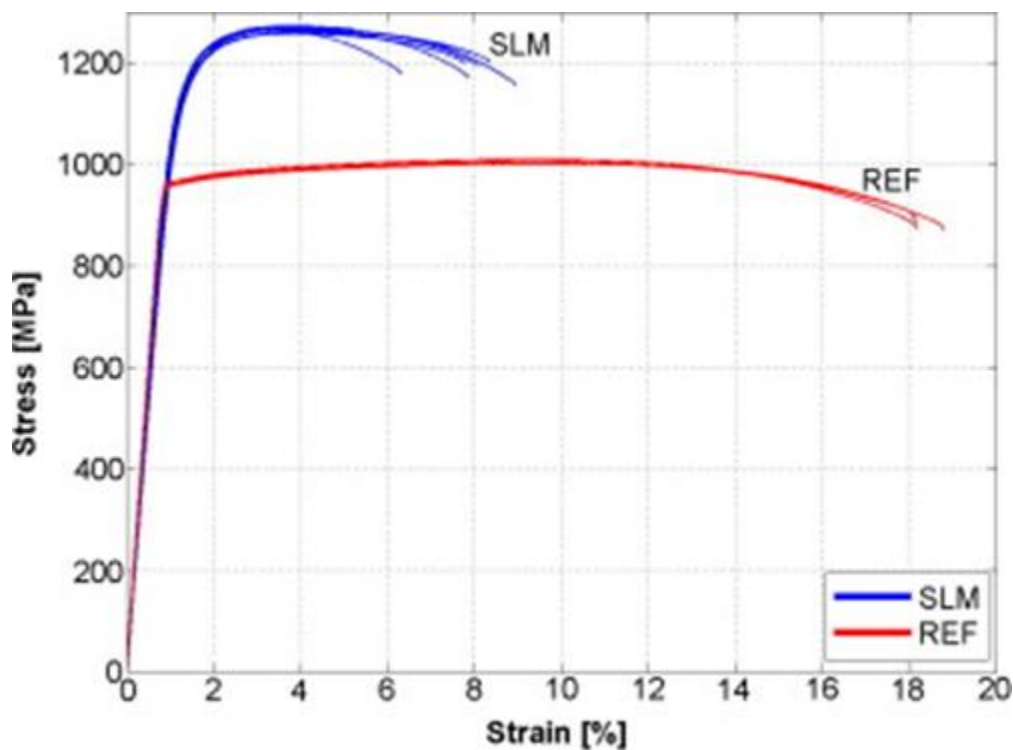
Fig. 2.29: Stress–strain curves for untreated SLM Ti-6Al-4V and reference Ti-6Al-4V [10].

However, only limited research has been performed on this topic. Facchini *et al.* [36] performed post-building heat treatment of a Ti-6Al-4V alloy produced by selective laser melting of pre-alloyed powders causing the transformation of the metastable martensite in a biphasic α-β matrix resulting in an increase in ductility and a reduction in strength values. Sercombe *et al.* [37] performed solution treatment Ti-6Al-7Nb components that had been produced via selective laser melting (SLM) resulting in homogeneous structure. Vilaro *et al.* [38] analyzed as-fabricated and heat-treated microstructures of the Ti-6Al-4V

alloy processed by selective laser melting which exhibited high yield and ultimate strengths while the ductility is significantly improved.

Vrancken *et al*. [10] studied the different response of SLM parts on generally applied titanium heat treatments and distinguished the influence of time, temperature and cooling rate. However, they found that, due to the specific process conditions and hence specific microstructure, application of standard heat treatments shows that these treatments do not lead to the usual or expected results, SLM produced parts need to be treated differently than bulk alloy parts. Becker *et al*. [138] studied LaserCUSING (a selective laser melting (SLM) process that is capable of manufacturing parts by melting powder with heat input from a laser beam) processed Ti-6Al-4V on the combination of machine parameters and heat treatments to optimize material behavior while minimizing residual stresses and porosity defect. They found that LaserCUSING produced Ti-6Al-4V ELI is characterized by comparable hardness as well as better mechanical characteristics when subjected to appropriate heat treatments. Fan *et al*. [11] investigated the effects of process parameters of laser additive manufacturing (laser power, scanning speed, scanning direction) and heat treatment on the microstructure and properties of Ti-6Al-4V alloy forming parts under coaxial powder feeding. Through the solution and aging heat treatment, they observed that the original properties can be improved and the high performance can be obtained. They also stated that the solid solution and aging heat treatment can effectively improve the strength and plasticity of the deposited Ti-6Al-4V alloy, and its strength and plasticity exceed the requirements of the national standard of Ti-6Al-4V alloy castings and forgings with annealed state.

（a）Sedimentary state （b）950 ℃/AC/1 h+540 ℃/AC/ 4h （c）950 ℃/FC/1 h
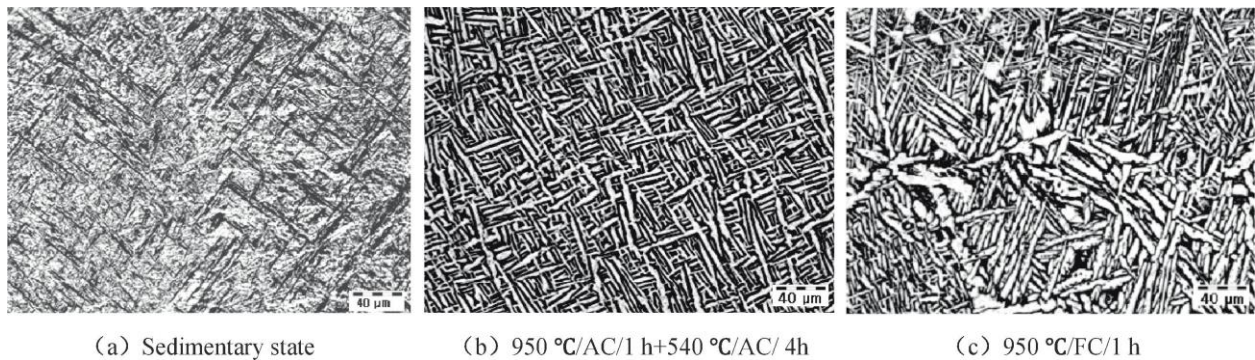
Fig. 2.30: Microstructure of 3D printing Ti-6Al-4V alloy under different states observed by Fan *et al*. [11].

Ahmadi *et al*. [12] applied two different heat treatment regime (below and above β-transus) to investigate their effects on the microstructure and mechanical properties of additively manufactured porous Ti-6Al-4V alloy. Although it was observed that heat

treatment substantially changes the microstructure of as-processed Ti6Al4V samples, they concluded that structure density of AM structures does not improve by heat treatment and in order to solve this problem other post treatments method like hot isostatic pressing (HIP) must be considered.
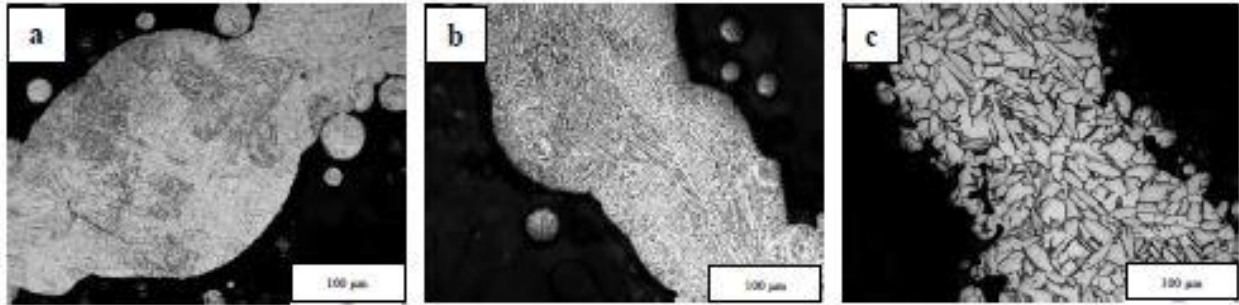
Fig. 2.31: Microstructure of a) as-processed, b) T800 and c) T1050, observed by Ahmadi *et al*. [12]

Yan *et al*. [13] studied the effect of thermo-mechanical treatment on the microstructure transformation and mechanical properties of SLM processed Ti-6Al-4V ELI alloy samples aiming to identify the appropriate treatment for biomedical or aeronautical applications, in order to improve the overall mechanical properties. They found that although as-built samples have a relatively higher microhardness, after HT up to 900°C, microstructure coarsening lead to a decrease of this microhardness. However, HT over 900°C contributes to an increase of the microhardness which reaches the highest value (after the as-built condition) at 1080°C due to the formation of a Widmanstatten structure upon cooling.
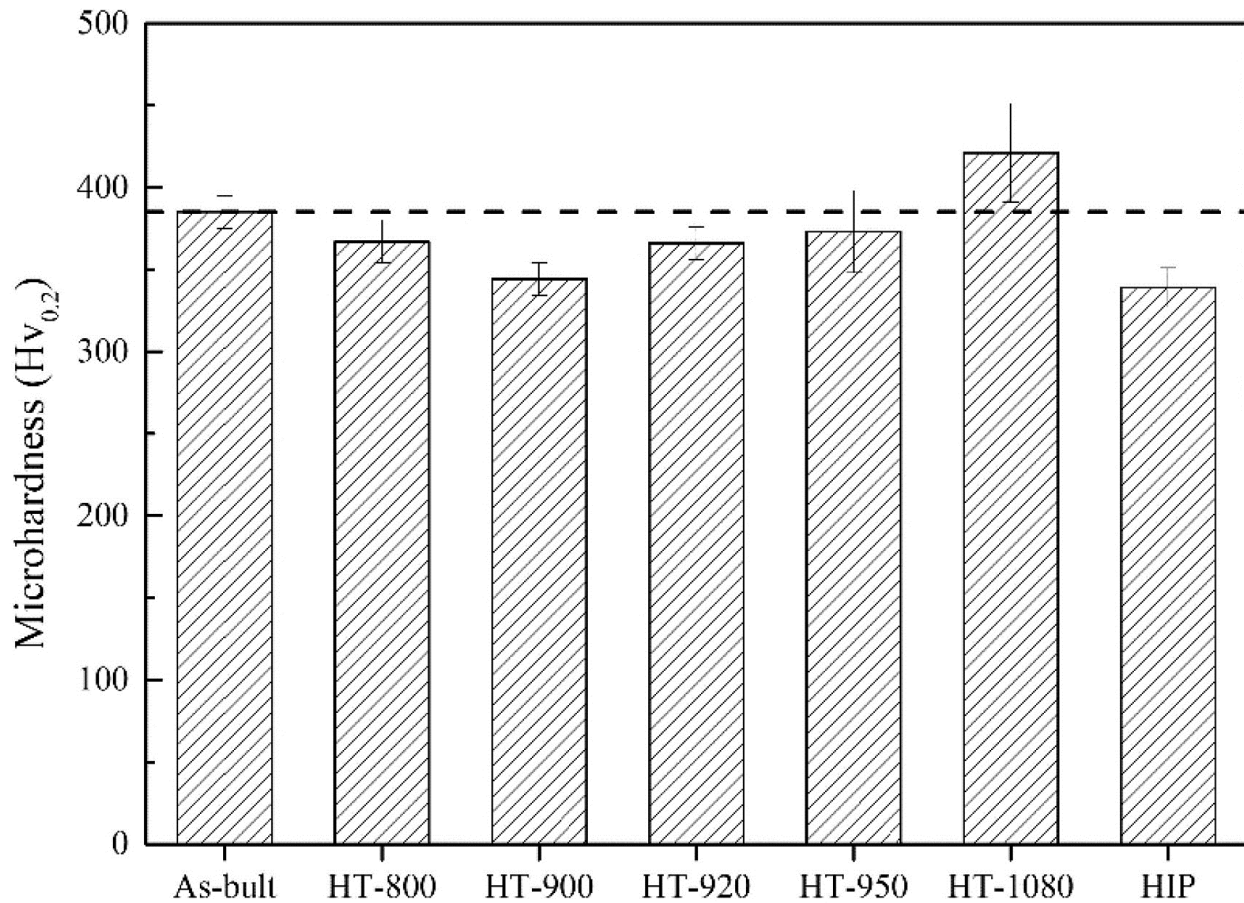
Fig. 2.32: Vickers microhardness of SLM samples following several thermo-mechanical treatments investigated by Yan *et al.* [13].

Galarraga *et al.* [14] investigated the effect of different heat treatments on the unique microstructure of the EBM Ti-6Al-4V ELI (Extra Low Interstitial) and its impact on mechanical properties. They found that It was observed that faster cooling rates after solution heat treatment produce a greater amount of α' martensitic phase, with water-cooling at a rate of 650°C/s resulting in a fully α' martensitic microstructure. However, increases in α lath thickness was found to have a detrimental effect on mechanical properties like an increase in α lath thickness from 0.62 to 2.9 μm reduced micro-hardness, YS, UTS, and elongation by 11%, 8.5%, 1.5%, and 26% respectively.
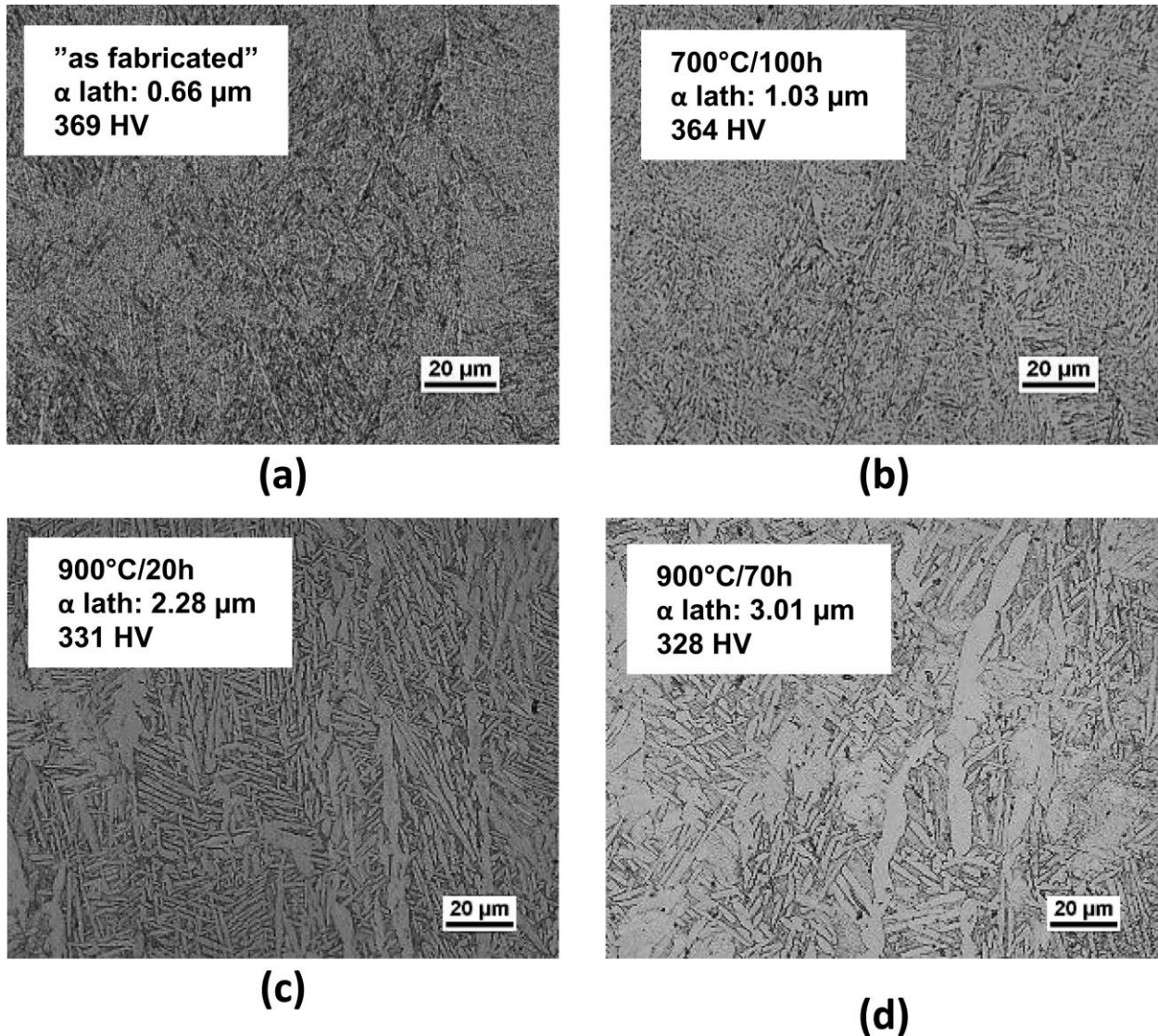
Fig. 2.33: Micrographs at 500X magnification for (a) as-fabricated, (b) annealed at 700°C for 100 h, (c) annealed at 900°C for 20 h, (d) annealed at 900°C for 70 h, investigated by Galarraga *et al.* [14].

2.7. The Current Work.

2.7.1. Depth-sensing time dependent deformation of AM Ti-6Al-4V alloy

Consistency of mechanical properties and microstructures in the additive manufacturing is still a critical issue. Since Ti-6Al-4V alloy is a two-phase alloy, mechanical properties can be significantly varied by tailored microstructure [21]. Having various cooling rates at different positions and distances from the built plate in different additive manufacturing methods, the microstructure, in particular formation of α, can vary a lot [22]. Deposition of layers with partial re-melting and solidification of previous layer and

cooling in various ways for various geometries adds complications to the processes. In spite of many studies in the literature to date, rate dependent plastic deformation of the Ti-6Al-4V alloy manufactured by the L-PBF method has not been studied at small scales with microstructural gradients.

In L-PBF method components are fabricated via directed energy and pre-deposited layer where energy source can be in the form of electron beam or laser [20]. Due to rotation of laser for each layer, L-PBF build materials ended up having net shape which often require subtractive machining. L-PBF heat transfer is highly dependent on relative laser/ gas direction which plays a significant role on melt pool formation and surface properties. Manufacturing design decisions including scan strategy, laser power, scanning speed etc. directly affects the microstructure of the fabricated parts as well as affect the resultant heat transfer. To reduce oxide formation along the surface, protect the melt pool from contamination, and to co-operate expelling spatter/ debris, inert shielding gas is employed during welding and laser based AM processes. It was observed that shielding gas like argon gas not only decreases spatter significantly but also stabilize the laser welding process via convection heat transfer and enhanced ionization-recombination [139, 81]. Kah *et. al.* investigated effects of various shielding gases on the microstructural and mechanical properties including ductility, tensile strength, hardness, pitting corrosion resistance on different metals and found significant improvement of mechanical properties [83]. The samples investigated in this research were fabricated in unidirectional scan direction (i.e. without rotating pattern in each layer like typical L-PBF process) in both parallel and perpendicular to the argon gas flow. The sample were also manufactured using different scan size which also affected the temperature gradient i.e. the thermal response. Due to variation of scan direction with respect to argon gas flow, the temperature gradient was found to be different for each sample [79] and therefore, it is required to assess the time –dependent deformation for these Ti-6Al-4V alloy samples fabricated at different manufacturing scan direction and scan sizes.

Considering the literature mentioned in this chapter, ambient-temperature creep response of an additively manufactured Ti-6Al-4V alloy and correlations between creep parameters (*i.e.* creep rate, creep stress exponent, indentation size effect) and additive manufacturing variables (*i.e.* scan directions and scan sizes) has not yet been documented. In this present research an instrumented (depth-sensing) indentation testing technique was employed to assess ambient-temperature creep and the corresponding mechanisms of an additively manufactured (AM) Ti-6Al-4V alloy. In addition, indentation size effect and microstructural assessments are studied in this research. Moreover, to this end, microstructural quantitative analyses (*i.e.* optical

microscopy (OM) and scanning electron microscopy (SEM)) are performed to assess microstructure of the AM Ti-6Al-4V alloy and the creep property correlations during the holding time as a function of indenter peak load.

The outcome of this research provide a baseline to study elevated-temperature creep of AM Ti-6Al-4V alloy and to compare the results with the conventionally made Ti-6Al-4V alloy. Most of the reported creep results in the literature till date are based upon traditional (uniaxial/ tensile) approach which could be destructive, time-consuming and tough-to-control (specially at the elevated temperatures) tests. In particular, on the AM aspect, a number of creep test coupons must be printed which could be a costly as well as time consuming task. Having said this, the present research promotes the application of the depth-sensing indentation testing technique, as a noble, reliable, convenient and non-destructive approach that can be performed on a small volume of material and can be used toward assessing time-dependent plastic deformation (creep) in AM materials at both ambient and elevated temperatures.

2.7.2. Effect of various heat treatment cycles on microstructure and micro-mechanical properties of AM Ti-6Al-4V alloy

Microstructure evolution and mechanical properties have been studied in various literature for Ti-6Al-4V alloys due to its versatility resulting from the good balance between mechanical properties, castability, plastic workability, heat treatability, and weldability [14]. Ti-6Al-4V has been applied in industry and studied in the laboratory in large, resulting in an extensive knowledgebase relative to other metal alloys fabricated by this additive manufacturing technology. Heat treatment of AM Ti-6Al-4V for various heat treatment technologies has been extensively studied with the purpose of relieving stress and achieving an equilibrium microstructure, eliminating the metastable α' martensite phase and obtaining a microstructure with exclusively α and β phases. However, for the L-PBF technology, the relation between microstructure and mechanical properties has been mainly limited to the as-fabricated condition. The L-PBF process, similarly to other AM processes, does not completely prevent the presence of porosity in the build. In order to mitigate the disadvantages caused by these defects, the effect of HIP treatment has been studied in numerous instances [68, 92, 140–142].

Since the relatively poor wear resistance of this alloy leads to excessive wear, mechanical and chemical instability, and implant loosening [143], various surface treatment methods, such as ion implantation, TiN coating, and thermal oxidation, have thus been proposed to improve the wear resistance by changing the nature of the surface.

With regard to basic properties of Ti alloy including the equilibrium phase diagram, physical and metallurgical properties, heat treatment process and metallographic structure, there are a lot of useful data can be acquired. A variety of microstructures can be tailored by different simple thermo-mechanical treatments at above and below β-transus on this $\alpha + \beta$ alloy. Therefore, it is required to assess the effect of various heat treatment on microstructure and micromechanical properties of AM $\alpha+\beta$ Ti-6Al-4V alloy.

While there are numerous data on the common Ti–6Al–4V alloy, very limited studies involving the microstructure and micro-mechanical characteristics of the Ti-6Al-4V alloy have been reported. The primary objective of this investigation is, therefore, to evaluate the effect of various heat treatment on microstructure and micromechanical properties of additively manufactured Ti-6Al-4V alloy. Indentation testing technique was applied to assess the micro-mechanical properties including stress distribution over the penetrated depth of the indenter. Vickers micro-hardness testing approach was used to verify the hardness after various heart treatment approach.

Ti-6Al-4V is an $\alpha+\beta$ alloy where α and β microstructural phases coexist at room temperature. The $\alpha+\beta$ alloys are interesting as they combine both the strength of α alloys with the ductility of β alloys, and their microstructures and properties can be varied widely by appropriate heat treatments and thermomechanical processing [14]. The current study focuses on understanding the effect of various heat treatments on the unique microstructure of the L-PBF Ti-6Al-4V and its impact on microstructure and micro-mechanical properties. The heat treatments studied in this work were addressed using four various heat treatment approaches. The effect of water quenching, air cooling, furnace cooling, and ageing (precipitation hardening) heat treatments and subsequent formation of different microstructural phases and their impact on micro-mechanical properties were investigated.

Chapter III

3. Experimental Methodology

This section describes a brief background of the fabrication of the samples and the various methods used throughout this thesis; more detailed process and experimental parameters are given in the relevant manuscripts.

3.1. Additively Manufactured Ti-6Al-4V samples

The material studied in this thesis is an additively manufactured Ti-6Al-4V alloy fabricated via the L-PBF process in horizontal and vertical scan direction. Fig. 3.1 shows the scanning direction and size of the samples used in this research. For both X and Y scan direction, two rectangular samples with dimensions of 9.8×9.8×5.60 mm^3 (coded as *Big* sample and shown in Fig. 3.1(a) and 1(b)) and 4.8×4.8×5.5 mm^3 (coded as *Small* sample and shown in Fig. 3.1(c) and 1(d)) were prepared.
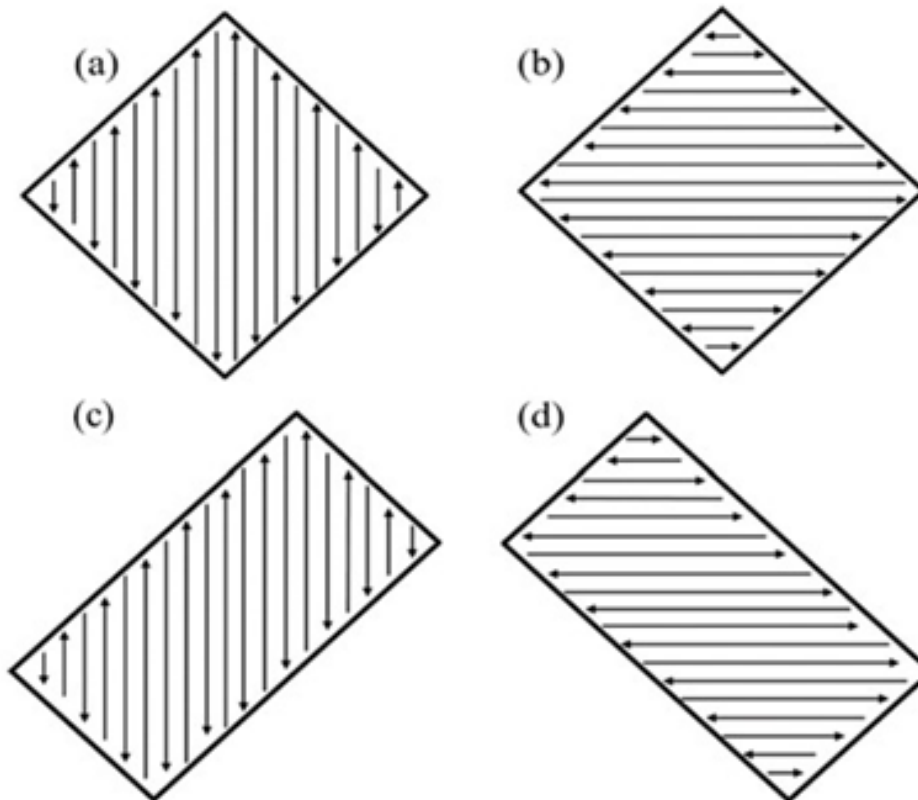
Fig. 3.1: Built direction and built size of samples of the additively manufactured Ti-6Al-4V alloy used in this study (a) CNPY-Big, (b) CNPX- Big, (c) CNPY- Small, (d) CNPX-small.

Scanning tracks for sample "Core X" were parallel to flow (argon) direction and samples were named as "Core No Post X-big" (CNPX-big) and "Core No Post X-small" (CNPX-small). Scanning tracks for sample "Core Y" were perpendicular to flow direction and for this research samples were named as "Core No Post Y-big" (CNPY-big) and "Core No Post Y-small" (CNPY-small). The term "No post" indicates that no post contour exposure was done on these specimens *i.e.* after fabrication of each layer, lasers re-melted the boundary of parts. Masoomi *et. al.* [79] have found that by decreasing build area of additively manufactured parts or using shorter tracks, the temperature gradient will decrease, and it will cause lower residual stress in the parts. In this research, parts with different volumes are chosen to demonstrate this effect. The process parameters chosen to fabricate parts is summarized in Table 3.1:

Table 3.1 - Parameters used for fabrication of Ti–6Al–4V parts

System	EOS M290
Substrate material	Ti-6Al-4V
Powder description	Gas-atomized, air-dried
Mean particle diameter	35 μm
Powder layer thickness	50 μm
Powder bed porosity	0.4
Laser spot diameter	100 μm
Laser power	170 W
Scan speed	1250 mm/s
Building volume	25 x 25 x 35 cm^3
Shielding gas type	Argon
Shielding gas inlet temperature	20^{0}C
Shielding gas inlet flow rate	0.25 m^3/s
Chamber wall temperature	20^{0}C

Fig. 3.2: EOS 290 3D printer used in this research to print the samples.

Prior to the instrumented indentation testing, the surfaces of the specimens were carefully ground with a series of progressively finer sand papers followed by fine polishing which resulted in scratch free mirror-like surface finish. A modified Kroll's reagent (5 ml HF, 15 ml HNO_3, and 80 ml distilled water) was used to reveal the microstructure. Microstructure and grain sizes of four specimens were then examined by Scanning Electron Microscope (SEM) and Optical Microscopy (OM).

Hysitron Ubi-1 Nanoindenter is a quasistatic instrumented indentation system for nanomechanical testing of nano/ micro-mechanical properties, including Young's modulus, fracture toughness, and hardness. It is ideal equipment for measuring micro-mechanical properties of coatings and thin films, as well as the spatial dependence of hardness and elastic modulus of materials. It's three-plate capacitive transducer is designed for a high displacement sensitivity and a low thermal drift.

In situ scanning probe microscopy (SPM) capabilities are also available which has enabled to capture image of sample surfaces before and after indentation. The

piezoelectric scanner used for SPM imaging is also highly capable for an automated micro-mechanical testing at multiple locations within an imaged/ scanned area. Creep, stress relaxation, and surface adhesion can also be investigated using closed-loop load- or displacement-controlled indentation modes. Analysis software accompanied with the system was used to calculate reduced moduli and hardnesses from unloading curves and measured tip area functions.

Fig. 3.3: Hysitron Ubi-1 Nanoindenter used in this project.

Table 3.2 - Hysitron Ubi-1 Nanoindenter specifications

Maximum Force	10 mN
Thermal Drift	< 0.05 nm/sec
Load Noise Floor	100 nN
Maximum Displacement	20 μm
Maximum Range of Piezoelectric Scanner	60 μm x 60 μm
Displacement Noise Floor	0.2 nm
Load Resolution	1 nN
Displacement Resolution	0.04 nm

Hysitron Ubi-1 Nanoindenter is an excellent tool to analyze the micro-mechanical properties of the materials and used throughout the research period. However, due to limited maximum loading capability (10 mN), limited maximum displacement (20 μm), and limited holding time capability, Hysitron Ubi-1 Nanoindenter is not an ideal equipment to analyze ambient temperature creep of high strength material like Ti-6Al-4V alloy which needs significantly longer holding time for creep deformation. Hence, the nano indenter G200, which can exert high maximum loading capability (500 mN), high maximum displacement (500 μm), and high holding time capability, was used only to investigate ambient temperature time dependent deformation of additively manufactured Ti-6Al-4V alloy.

Nano-Indenter G200 is one of the world's most precise, flexible, and user-friendly instrument for nanoscale mechanical testing for micro-to-nano range of loads and displacements. In nano indenter G200, electromagnetic actuation allows to achieve unparalleled dynamic range in force and displacement.

The Nano Indenter G200, a user friendly equipment, enables to deduce Young's modulus and hardness in compliance with ISO 14577. The G200 also enables to measure deformation over six orders of magnitude (in the range of nanometers to millimeters). The capabilities of the G200 are also extended to facilitate frequency-specific testing, quantitative scratch and wear testing, high-temperature testing, integrated probe-based imaging, expanded load capacity up to 10N, and customizable test protocols.

The Nano-Indenter G200 is an excellent tool to quantify the relationship between structure, properties, and performance of their materials quickly and easily with minimal sample preparation. Unique design of the nano-indenter G200 avoids lateral displacement artifacts and it is powered by electromagnetic actuation-based force trans-ducers to ensure accurate measurements. Benefits of the Nano-Indenter G200 design are including but not limited to convenient access to the entire sample tray, easy viewing of the sample position and the sample work area, excellent sample positioning accuracy, and simplicity in sample height adjustment to speed test throughput.
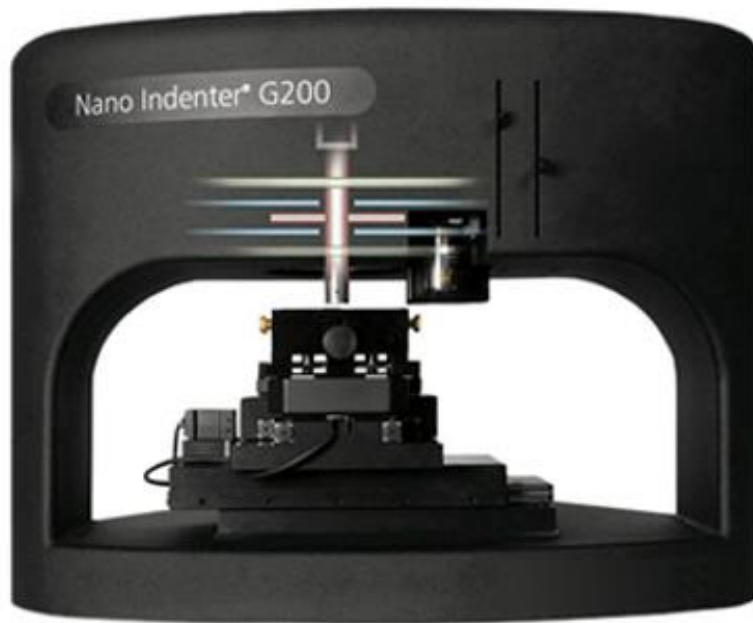
Fig. 3.4: U9820A Keysight Nano-Indenter G200.

Table 3.3 - Keysight Nano Indenter G200 specifications

Standard XP Indentation Head	
Displacement resolution	< 0.01 nm
Total indenter travel	1.5 mm
Maximum indentation depth	> 500 μm
Load application	Coil/magnet assembly
Displacement measurement	Capacitance gauge
Loading capability	
Maximum load (standard)	500 mN

Maximum load with DCM II option	30 mN
Maximum load with High Load option	10 N
Load resolution	50 nN
Contact force	< 1.0 μN
Load frame stiffness	~5 x 106 N/m

Indentation placement

Useable surface area	100 mm x 100 mm
Position control	Automated remote with mouse
Positioning accuracy	1 μm

Microscope

Video screen	25x (x objective mag.)
Objective	10x and 40x

DCM II Indentation Head Option

Displacement resolution	0.0002 nm (0.2 picometers)
Range of indenter travel	70 μm
Loading column mass	< 150 mg
Load application	Coil/magnet assembly
Displacement measurement	Capacitance gauge
Typical leaf spring stiffness	~100 N/m
Typical damping coefficient	0.02 Ns/m
Typical resonant frequency	120 Hz
Lateral stiffness	80,000 N/m

Loading capability

Maximum load	30 mN (13 gm)
Load resolution	3 nN (0.3 μgm)

Express Test Option

Time per indentation	Standard < 5.0 sec

LFM Option

Maximum lateral force	> 250 mN
Lateral resolution	< 2 μN
Maximum scratch distance	> 100mm
Scratch speed	100 nm/s up to 2 mm/s
High Load Option	
Maximum force	10 N
Load resolution	50 nN
Maximum indentation depth	≥ 500 μm
Displacement resolution	0.01 nm
Frame stiffness	≥ 5 x 106 N/m
NanoVision Option	
X-Y scan range	100 μm x 100 μm
Z scan range	Indentation head dependent
Positioning accuracy	≤ 2 nm
Resonant frequency	> 120 Hz
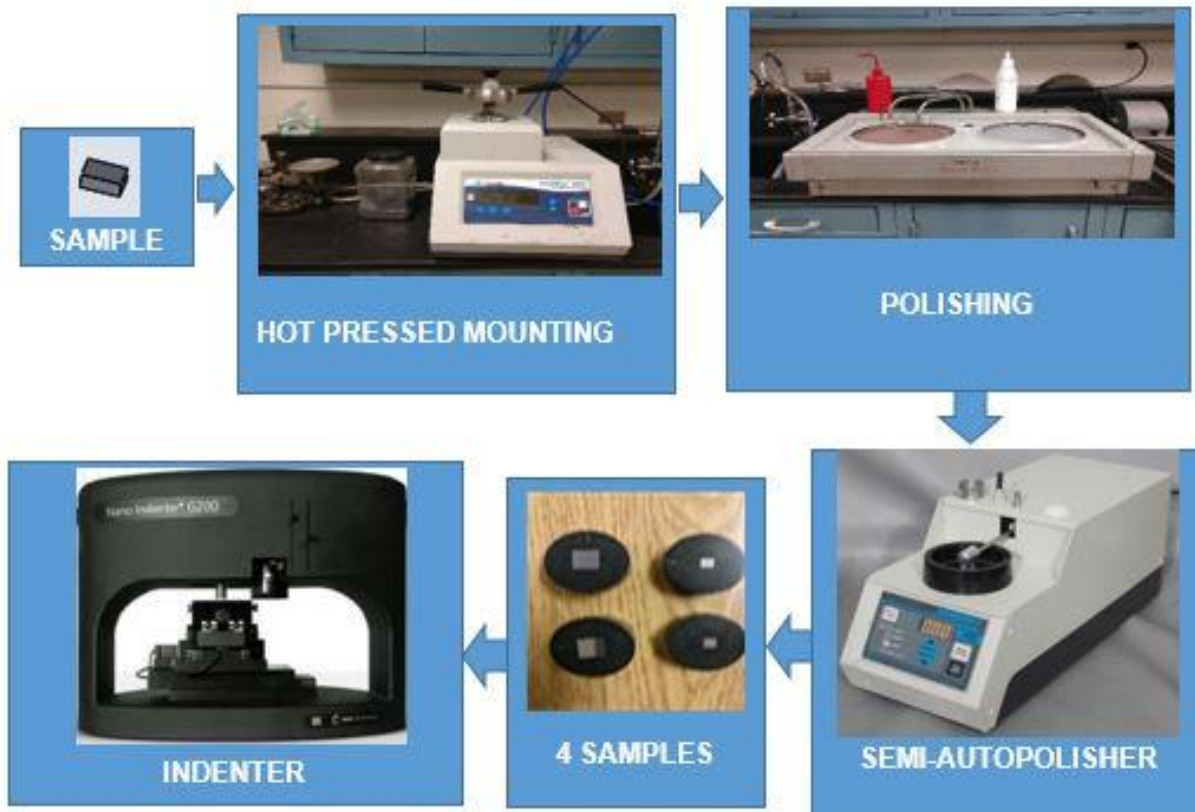
Fig. 3.5: Sample preparation for this research.

Before indentation testing, the microstructures of as-printed materials were analyzed using Scanning Electron Microscopy (SEM, QUANTA FEG 650) and Optical Microscopy (OM, MM500T).

Fig. 3.6: Optical Microscope (MM500T) employed in this study for microstructural assessments.

Fig. 3.7: QUANTA FEG 650 Scanning Electron Microscope used in this thesis.

3.2. Instrumented Indentation Creep

3.2.1. Introduction

Traditional uniaxial creep testing involves homogeneous loading of the complete gauge length of the sample, usually lasts between a few hundred and several thousand hours which results in homogenized value of σ_{ind} [144]. However, during a depth-sensing (instrumented indentation) creep testing, substantial and complex tri-axial stresses in the GPa ranges are generated beneath the indenter. This phenomenon could eventually induce significant creep deformation in the materials even at room temperature, unlike traditional uniaxial creep which is only observable at elevated temperatures. It is notable mentioning that non-homogeneous tri-axial stress states and a constantly growing deformation volume under the indenter during an indentation creep test could result in a deformation response rather different from that observed during conventional uniaxial

creep testing. The dynamics of the deformation in the indentation test are quite different in comparison to conventional uniaxial creep. Under the indenter, the deformed volume encompasses the previously undeformed material by continuous expansion. Material under the indenter being strained is very likely to expand the cavity with a hydrostatic core where no deformation was happening along with expanding plastic/ elastic boundary region. It is established that time dependent deformation process depends on rate of proceeding elastic/ boundary into the material [123].

During instrumented indentation, a fine scale indenter is used to load a sample in a controlled way, while the displacement is continuously recorded. The outcome of the test is indentation load versus indentation depth (see Fig. 3.9). The well-established procedure of Oliver and Pharr [99] was used to loading and unloading curves to deduce the hardness and modulus of the tested material.

In this thesis, depth-sensing indentation creep tests with dual stage scheme (loading followed by constant load holding) were performed at ambient temperature (298 K) using a U9820A Keysight Nano-Indenter G200 (shown in Fig. 3.4). A self-similar pyramidal Berkovich diamond indenter [145], [146] with a face angle of 65.3° was in this thesis.
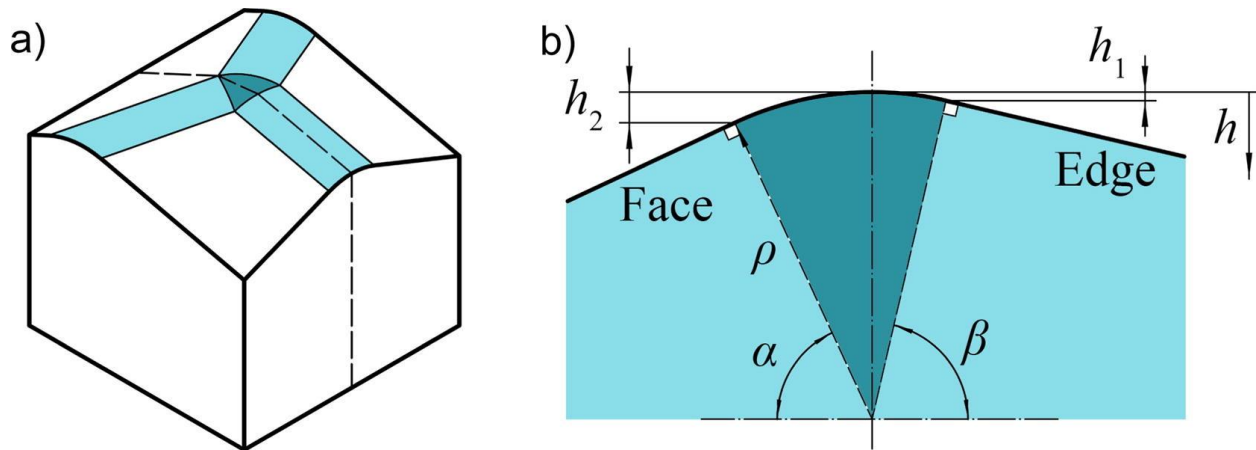
Fig. 3.8: Geometrical model of diamond Berkovich indenter with a consideration of tip and edge radii: (a) 3D shape of indenter apex; (b) 2D cross-section intersected along the dotted line shown in (a) [147].
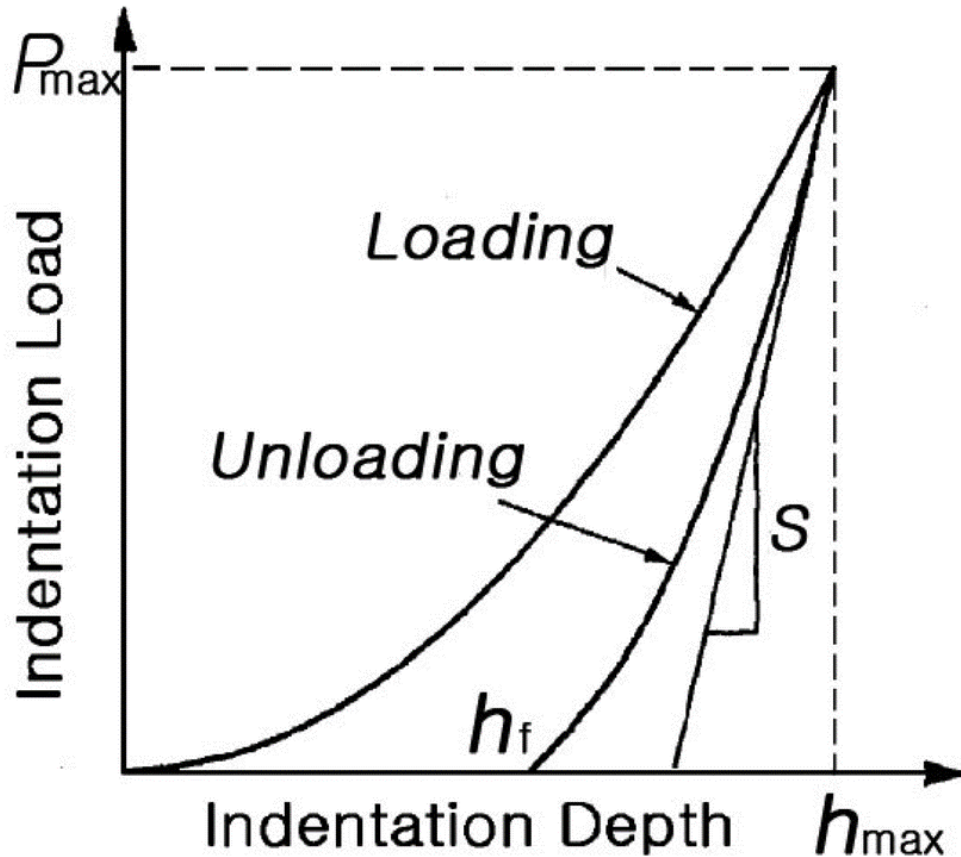
Fig. 3.9: Indentation *P-h* curve [148].

Indentation creep tests were performed at three constant peak loads of 250 mN, 350 mN, and 450 mN. Loading rate was set at 10 mN/s. Upon reaching to the peak load, the load was held constant for 400 s which is considered as creep time. The purpose of the dwell phase is to allow the material to 'creep out', i.e. to deform sufficiently for creep deformation to be insignificant during unloading. Creep rate will fall off with time, possibly due to decreasing contribution from primary creep. After 400 s, for the purpose of thermal drift corrections, the sample was unloaded to 10% of the peak load. Prior to indentation, thermal drift calibration was done to keep it under 0.05 nm/s, and each test was repeated five times to confirm reproducibility. The SEM and OM were used to assess the indentation morphology in terms of any possible sink-in and/ or pile-up. Figure 3.10 schematically shows the dual stage constant load rate constant load hold indentation creep performed in this project.
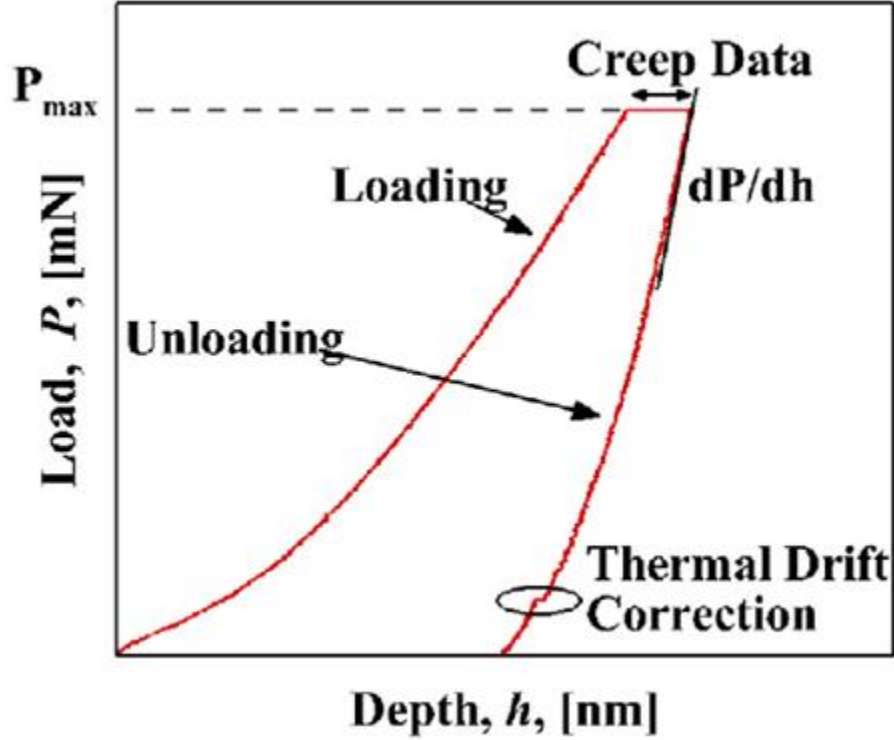
Fig. 3.10: Indentation *P-h* curve showing parts of curve used for creep, and thermal drift calculations [149].

3.2.2. Calculation Method

To analyze the time-dependent deformation behavior of a material by a depth-sensing indentation testing technique, it is required to mathematically represent the variation of indentation displacement as a function of time. With a Berkovich self-similar pyramidal indenter, experimental data of the holding stage was used to assess the creep behavior. In a depth-sensing self-similar instrumented indentation testing, the indentation strain rate can be written as [123, 150]:

$$\dot{\varepsilon}_{ind} = \frac{\dot{h}}{h} = \frac{1}{2}\frac{\dot{P}}{P} \tag{6}$$

Here, $\dot{\varepsilon}_{ind}$ is indentation strain rate, $\dot{h}$ is rate of indentation depth, h is the indentation displacement at a given time, $\dot{P}$ is loading rate, and P is indentation load. According to equation (6), under a constant indentation load rate test, indentation strain rate decreases with indentation depth. Radius of elastic/ plastic boundary is related with radius of indentation and hence, indentation strain rate is defined as instantaneous change in contact area divided by instantaneous contact area which is the direct measurement of

66

the progression of the elastic/ plastic boundary into material. Furthermore, for geometrically identical indenter, indentation strain rate is generally defined as instantaneous displacement rate of the time divided by instantaneous displacement as it is related with $\dot{A}/A$ [123].

Indentation stress can be calculated as [123, 150]:

$$\sigma_{ind} = \frac{P}{24.56 \times C(h + 0.06R)^2} \tag{7}$$

Here, P is indentation load, h is instantaneous contact depth, and R is the indenter tip radius due to blunting at tip which was 200 nm for the Berkovich indenter used in this research.

The creep rate $\dot{\varepsilon}$ of a crystalline metal is empirically described as [151]:

$$\dot{\varepsilon}_{ind} = \frac{AD_0 Gb}{kT}\left(\frac{b}{d}\right)^p \left(\frac{\sigma_{ind}}{G}\right)^n \exp\left(\frac{\Delta Q}{kT}\right) \tag{8}$$

Here, σ_{ind} is the indentation stress, A is a coefficient related to temperature and microstructure, D_0 is the diffusion coefficient, G is the shear modulus, ΔQ is the activation energy for thermal-activated process, n is the stress exponent, p is the grain size exponent, k is the Boltzmann constant, T is the temperature, d is the grain size, and b is the Burgers vector.

At a constant temperature, the steady-state creep rate relation is further simplified as [151, 152]:

$$\dot{\varepsilon}_{ind} = B\sigma_{ind}^n \tag{9}$$

Here, B is a constant.

At isothermal conditions, n can be ascertained by determining the slope of a $\ln(\dot{\varepsilon})$ versus $\ln(\sigma)$ plot in the steady state creep condition using following equation [151, 152]:

$$n = \frac{\partial \ln \dot{\varepsilon}_{ind}}{\partial \ln \sigma_{ind}} \tag{10}$$

The average indentation hardness can be written as [151, 152]:

$$H_{ind} = \frac{P_{ind}}{A(h_c)} \tag{11}$$

Here, h_c is instantaneous contact depth.

The elastic recovery parameters can be deduced from the following equation [151, 152]:

$$ERP = \frac{h_{max} - h_c}{h_{max}} \qquad (12)$$

Here, h_{max} is the maximum indentation depth and h_c is the contact depth.

3.3. Heat Treatment of additively manufactured Ti-6Al-4V alloy

In order to assess the effect of various post-heat treatment on microstructure and mechanical properties of the painted alloys, a separate set of the specimens were employed for the heat treatment operation. To assess the effect of various heat treatment on inner layer, CNPX-big samples were cut into half exactly at the middle from bottom surface to top. Four rectangular samples were thus prepared with dimensions of 9.8×4.9×5.60 mm³.

Heat treatment of the samples were executed in a KSL- 1100X furnace. We choose CNPX-Big to study for the heat treatment purpose. To this end, three different cooling regimes were applied. At first the samples were heated to 950⁰C (heating rate 15.8⁰C/min) and the samples were kept at the furnace for 1 h. Then one set of samples went through water quenching (WQ), one air cooling (AC), and one furnace cooling (FC). Air cooling was done by cooling the sample at the room temperature. Furnace cooling was done by turning off the heating (see Fig. 3.11).
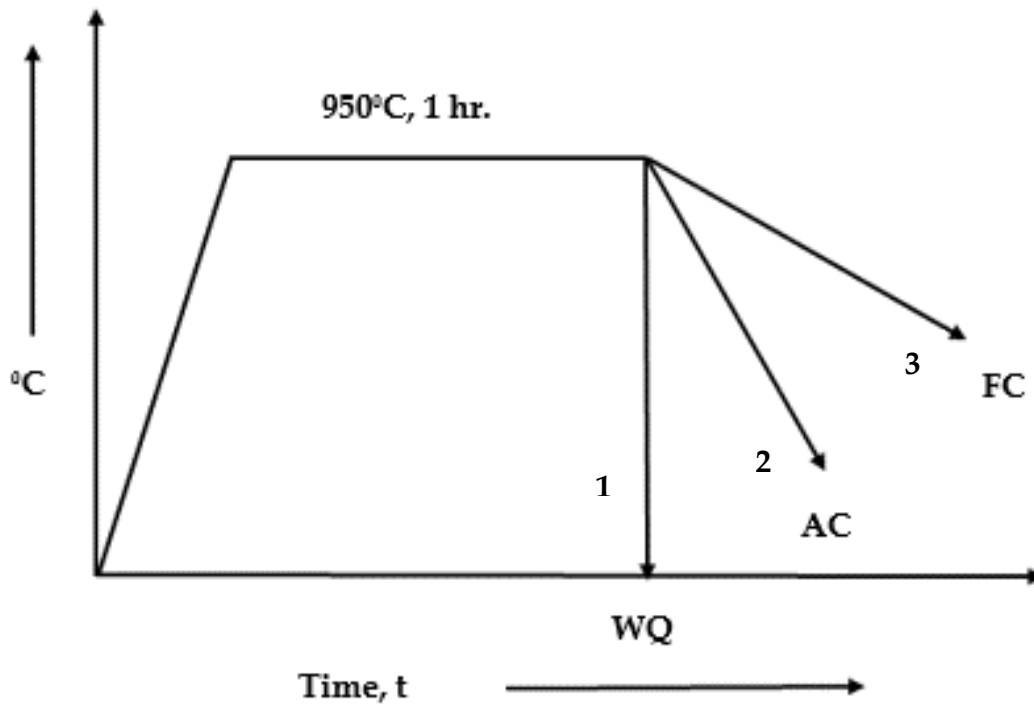
Fig. 3.11: Three different types of heat treatment: water quenching (WQ), air cooling (AC), and furnace cooling (FC).

A final sample was employed for aging (precipitation hardening) heat treatment. This was done to reveal the effect of aging heat structure on microstructure and mechanical property evolution. For this purpose, the sample was kept at the furnace for 1 hour at 950°C, then the sample undergoes water quenching. After that the furnace was heated to 540°C and the sample was kept at that temperature for 5 h and then air cooled. The schematic of the ageing is shown in the Fig. 3.12.
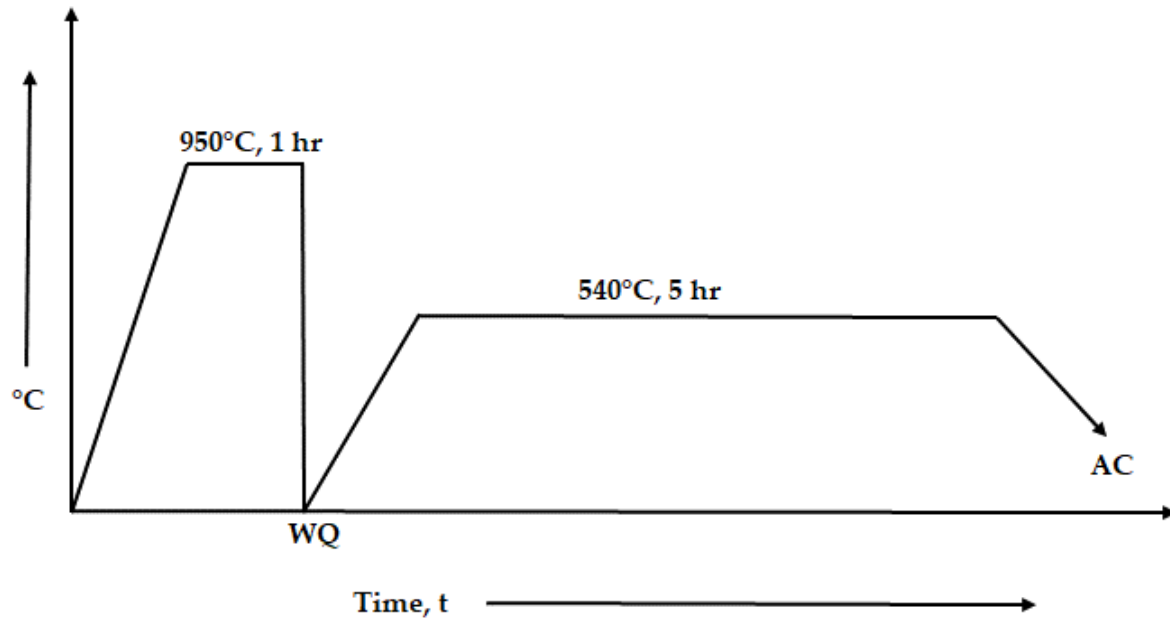
Fig. 3.12: Schematic of precipitation hardening of Ti-6Al-4V sample.

Following by these, micro-hardness tests were performed on all heat treated samples using a Vickers Hardness testing machine (HM 112 Mitutoyo) and depth sensing nanoindentation using Hysitron Ubi-1 nanoindenter. Nano indentation was performed with peak load of 10 mN. Loading rate was set at 2 mN/s. Upon reaching to the peak load, the load was held constant for 5 s. After 5 s, for the purpose of thermal drift corrections, the sample was unloaded to 10% of the peak load. Prior to the nano-indentation, thermal drift calibration was done to keep it under 0.05 nm/s, and each indentation test was repeated 25 times to confirm reproducibility. The SEM and OM were performed to study the indentation morphology. For micro-hardness testing, force of 4.9 N (0.5 KgF) was applied. The probe was in contact with the sample surface for 12 seconds for each indents performed to ascertain micro-hardness. Each plotted micro-hardness value is an average of 3 readings. For each sample, 25 positions were examined to confirm the reproducibility.

Fig. 3.13: KSL-1100X furnace used to perform heat treatment in this study.

Fig. 3.14: HM 112 Mitutoyo used to test micro-hardness in this project.

Chapter IV

4. Results and Discussions

The purpose of this chapter is to present and discuss the experimental results of this research. The results of the experiments include, ambient temperature creep parameters analysis (*i.e.* microstructural characterization, indentation creep response, creep stress exponent, indentation size effect etc.) across different scan size and scan direction, and effect of various heat treatment of additively manufactured Ti-6Al-4V alloy. The chapter is broken up into two sections investigation in the following ways:

1. Ambient temperature creep of AM Ti-6Al-4V alloy

2. Effect of various heat treatment of Ti-6Al-4V alloy

4.1. Ambient temperature creep of AM Ti-6Al-4V alloy

4.1.1. Microstructure

Because of the low to intermediate cooling rates experienced by Ti-6Al-4V alloy manufactured by L-PBF processes, an α-β lamellar structure associated with α-phase lamellae in a β-phase matrix is created. The α-lamellae are created by diffusion controlled nucleation and growth of α platelets into β-grains [153]. Size of α platelets is controlled by the cooling rate; an increased cooling rate lead to a decreased diffusion rate, which subsequently leads to decreased length and thickness of the α-lamellae associated with higher yield strength [154]. Fig. 4.1 shows the SEM micrograph consisting of the microstructures of CNPX-big and CNPY-small samples where the size of α colony is determined by the cooling rate from β phase and β grain size, while Fig. 4.2 (a) demonstrates the optical microscopy images of the microstructure of a CNPY-small sample which is showing scan tracks of additive manufacturing. Fig. 4.2 (b) depicts optical microscopy of indents along both the horizontal and vertical direction.

a

b
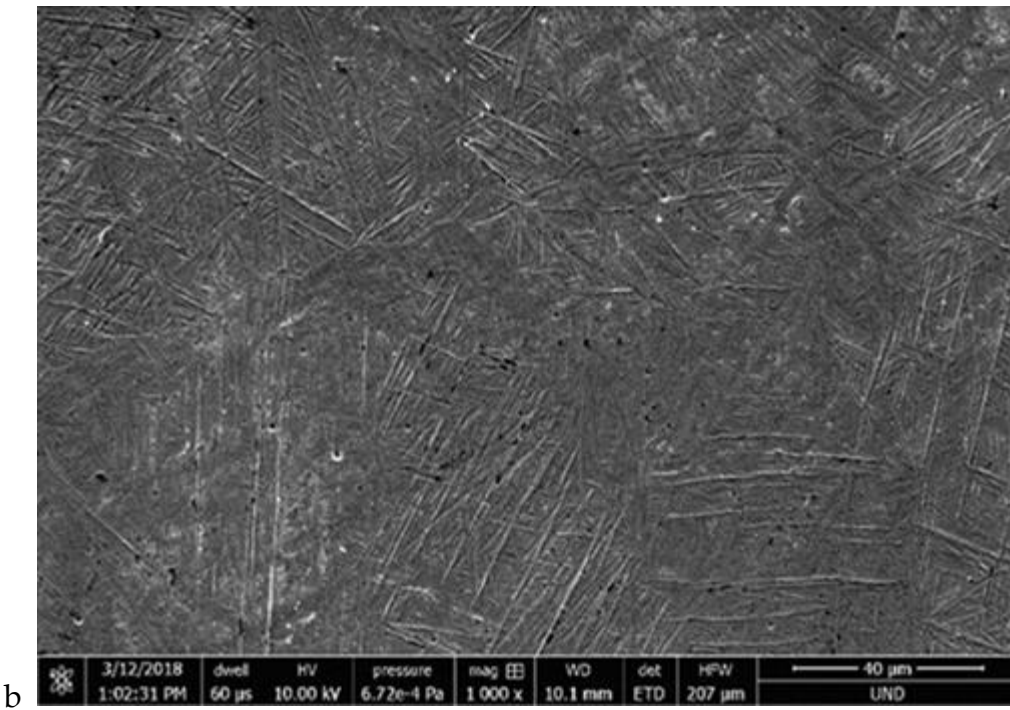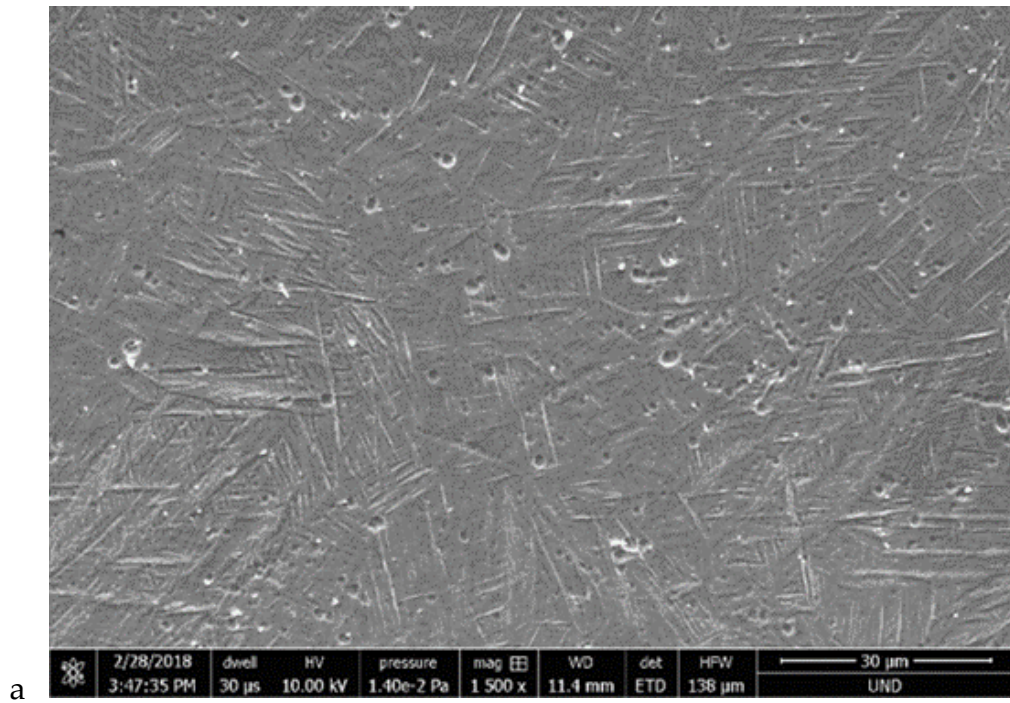
Fig. 4.1: SEM microstructure demonstrating (a) CNPX-big, (b) CNPY-small.
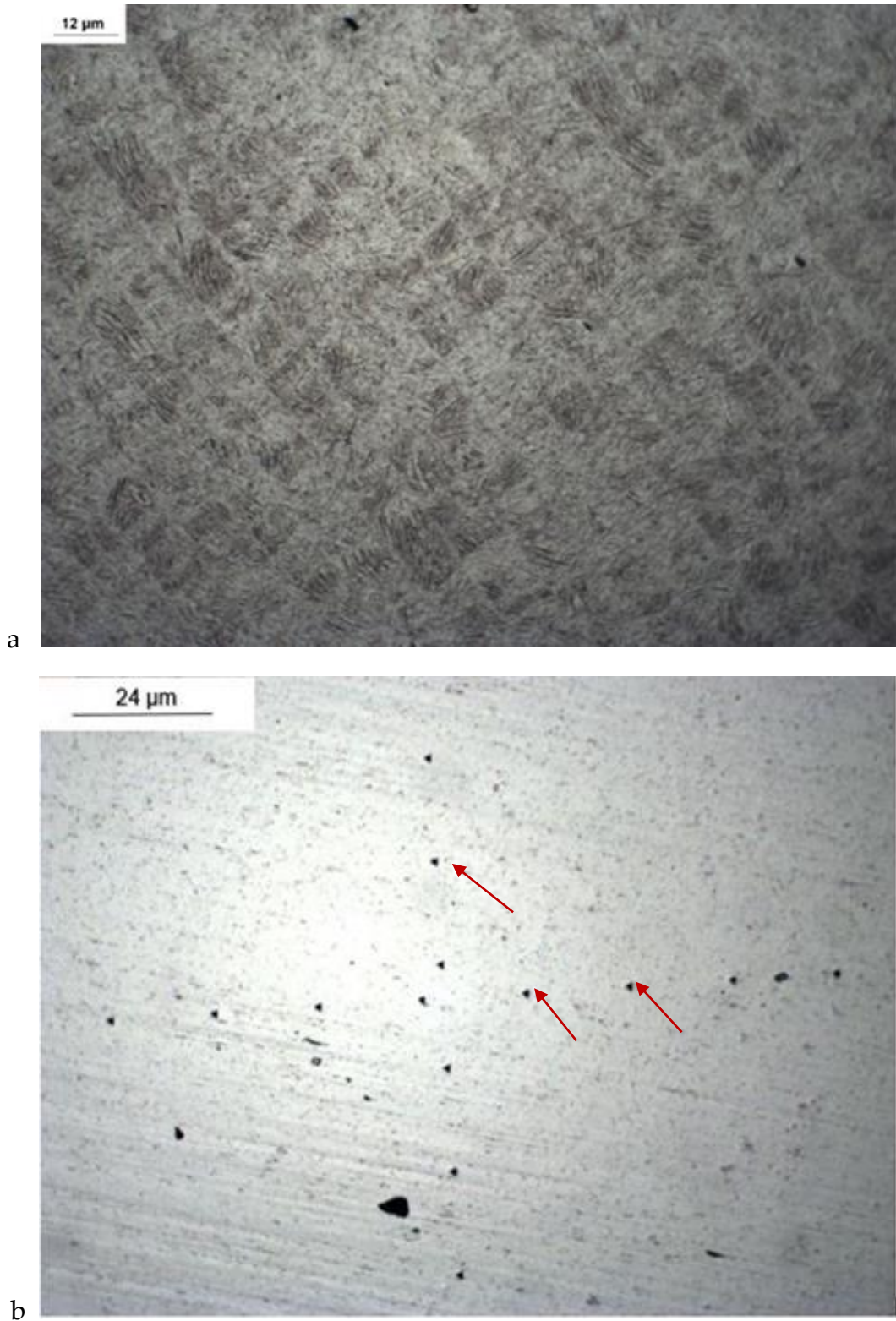
Fig. 4.2: Optical microscopy of microstructure consisting of (a) CNPY-small (b) indents of CNPY-big.

Fig. 4.3 shows a SEM micrograph of an indent made on the surface of specimen. Some sink-in effects are observed on the indented area of the specimen. In the sink-in phenomenon, it is observed that the flat sides of the impression is deformed inward around the indentation, which is a characteristic of elastic conical indentations [155]. According to Bolshakov and Pharr [156], while assessing pile-up or sink-in characteristics around the indenter, maximum indentation depth (h_m) and the final plastic depth upon unloading (h_f) are two expedient indicators. Sink-in behavior is a dominant factor when the ratio $\dfrac{h_f}{h_m}$ is less than a critical value (0.7), and material exhibits strain-hardening deformation behavior (*i.e.* ambient-temperature plastic deformation). Mohan *et al.* stated in the literature that the value of the A/A_{nom} determines the effect of pile-up or sink-in due to indentation near the tip. It was stated in the literature that if the ratio is lesser than unity, it indicates that sink-in has occurred with an actual contact area smaller than the nominal contact area and vice versa. [157]. Moreover, Elmustafa reported that strain rate sensitivity and work hardening influence the measure of pile-ups and sink-ins [158]. It was stated that rate-insensitive materials experience sink-in with the increase in the work hardening exponent and tend to pile-up in the absence of work hardening.
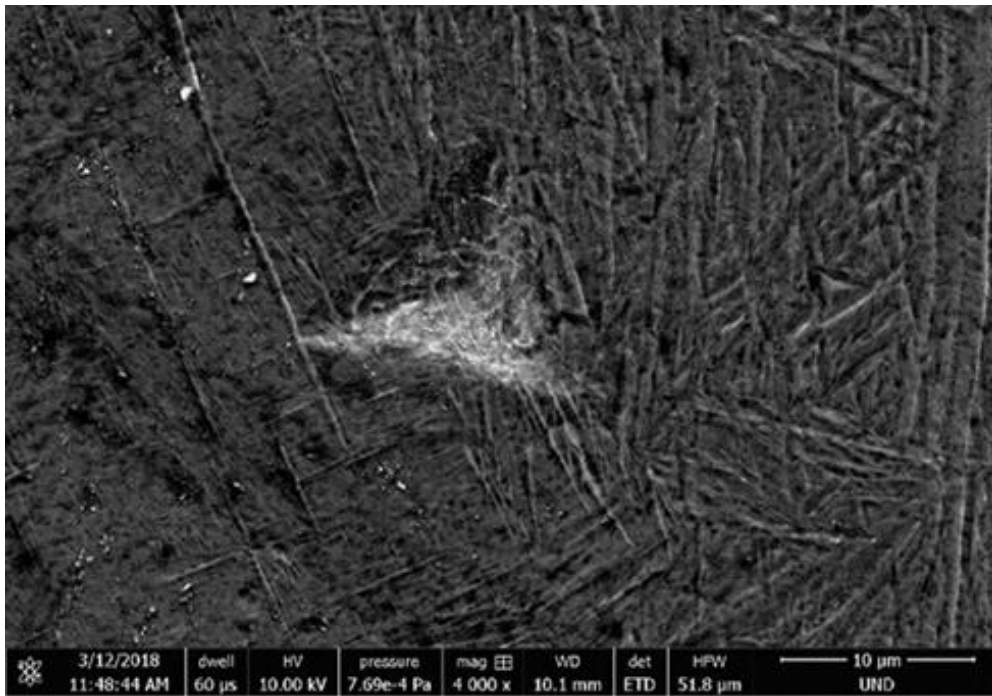
Fig. 4.3: Indentation morphology of Ti-6Al-4V for sample CNPY-small.

4.1.2. Indentation creep behavior

The load/ displacement (*P-h*) curves with a loading rate of 10 mN/s and holding time of 400 s for four samples at different maximum indenter loads of 250 mN, 350 mN, and 450 mN are demonstrated in Fig. 4.4. Load plateaus are observed at constant load holding stage and its width increases with increasing peak load. Stress distribution in the instrumented indentation technique is much more complex than conventional uniaxial tensile/ compressive creep tests, and at low displacement the maximum shear stress beneath the indenter exceeds the yield stress of the specimen (large tri-axial stresses in the range of some giga-Pascal) [159]. This phenomenon results in the occurrence of creep in the materials, including high melting-point materials, at ambient (room) temperatures, contrasting traditional creep tests which show creep mainly at elevated temperatures [160]. Specifically, in the Ti-6Al-4V alloy, ambient-temperature creep induced by prism and basal slip is reported [26].

a
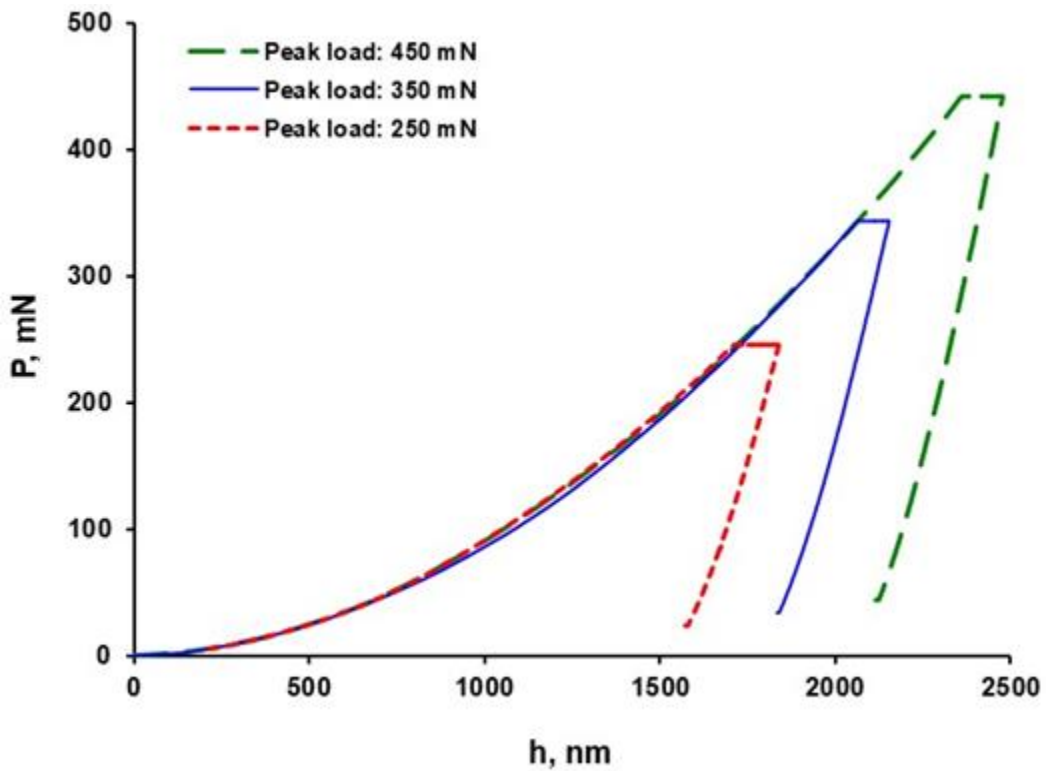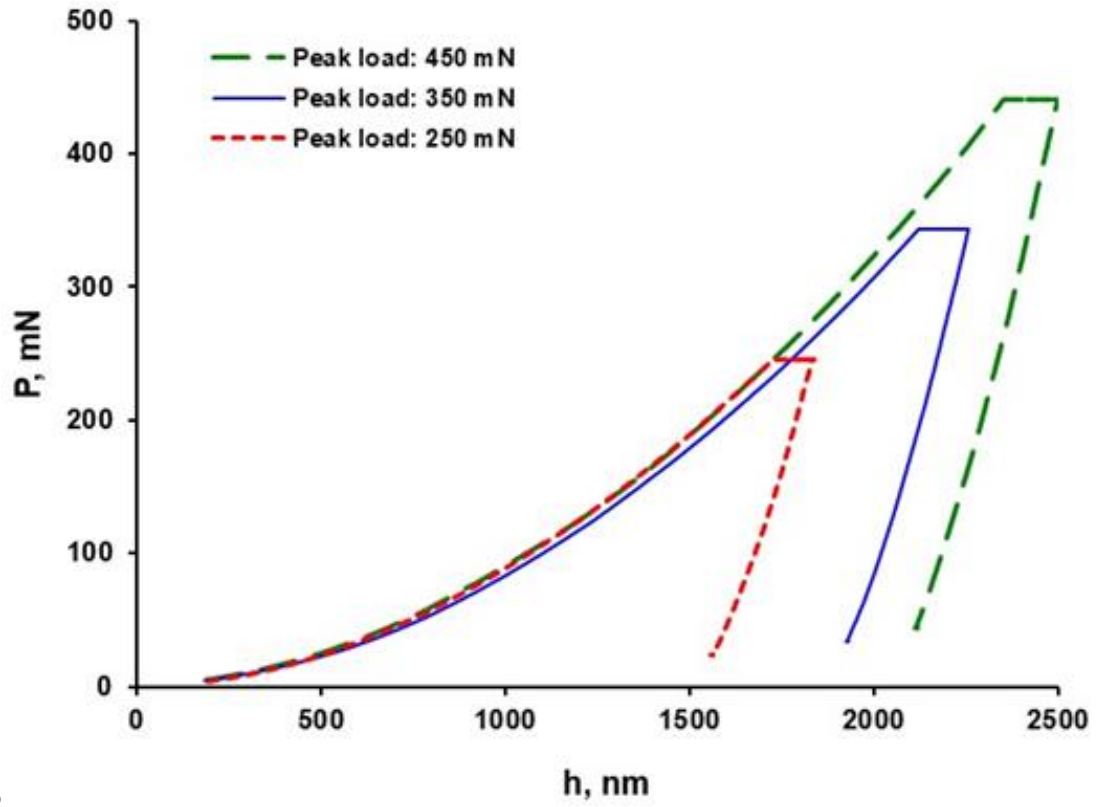
b
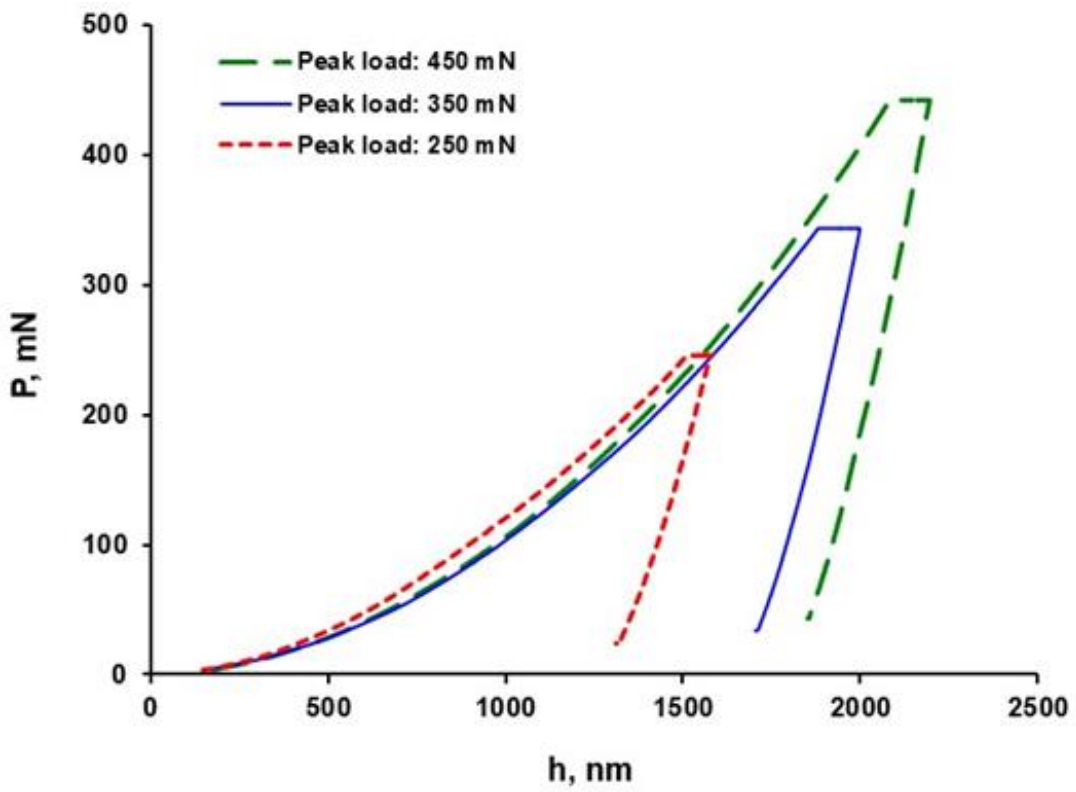
c
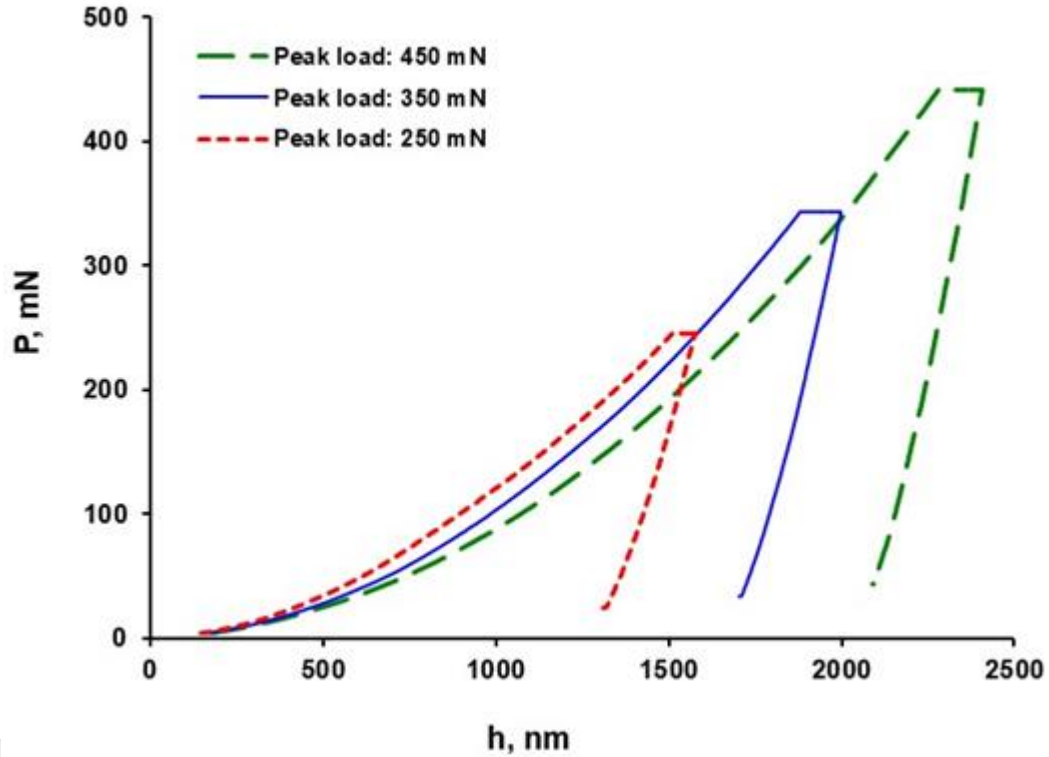
d

Fig. 4.4: Indentation load versus depth at different maximum indenter load at samples (a) CNPX_big (b) CNPX_small (c) CNPY_big (d) CNPY_small.

Alongside, stress states and volume of deformed material are essentially different in the uniaxial and nano-indentation creep techniques; a tri-axial non-homogeneous stress state and a continually growing deformation volume underneath the indenter are two important features of the nano-indentation testing approach.

From the variation of creep rate, the creep curve originating from the depth-sensing indentation can be divided into two separate zones: transient creep and steady-state creep [115]. Unlike traditional creep curves obtained from tensile/ compression testing, depth-sensing (instrumented) indentation testing does not have a third stage, or accelerated creep, since materials do not drastically fail under the indenter during indentation-based creep testing [116]. Due to high stress, the nucleated dislocations densified at nano-indentation are highly unstable during loading stage and tend to relax during the constant load-holding stage.

Fig. 4.5 depicts the variation of creep displacement and creep rate over time for a CNPX-big sample. At first a sharp decrease in creep rate is observed, which then reaches an

almost constant stage gradually. For instantaneous indentation depth, a sharp initial rise is observed, which transitions to a gradual increase over the holding time.
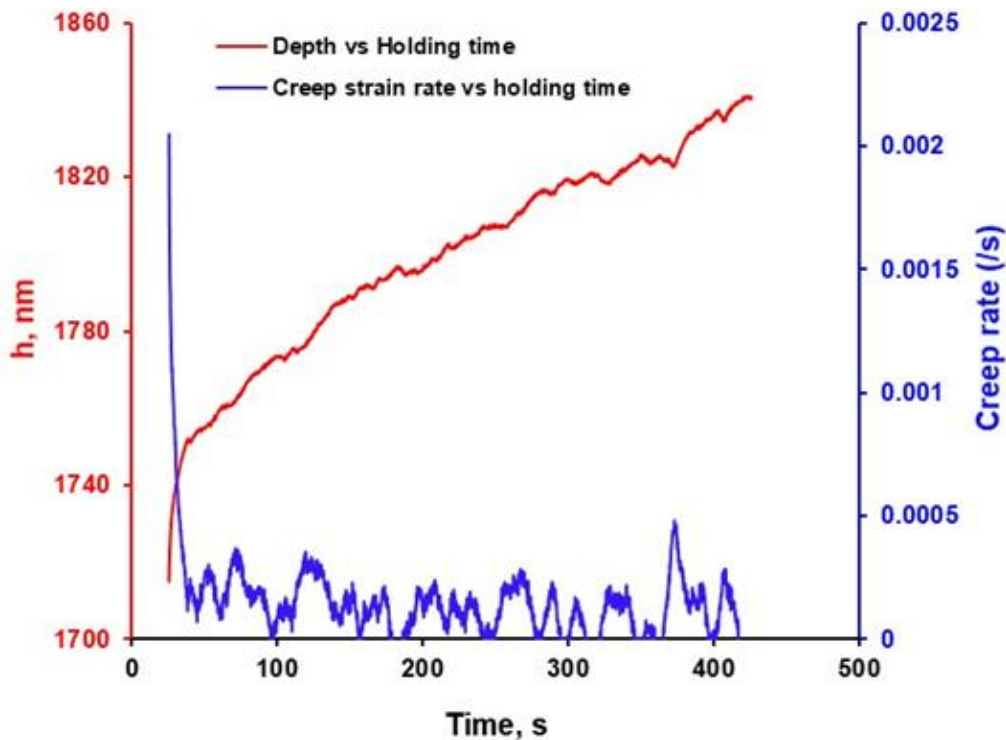
Fig. 4.5: Relationship between creep displacement with holding time and creep rate under peak load of 250 mN for CNPX-big with a holding time of 400 s.

The relationship between creep displacement and constant load holding time for Ti-6Al-4V alloy under different peak loads at different samples is plotted in Fig. 4.6. At the primary or transient creep stage all the curves experience an initial sharp rise and then as the indenter penetration continues within the specimen, the creep increases almost linearly at steady-state stage, which is similar to the uniaxial tensile/ compression creep. For all 4 samples, creep induced displacement is larger at higher peak loads (450 mN), which indicates that creep displacement depends on the indentation peak load (the larger the maximum indenter load, the higher the creep displacement will be). In the CNPX-big sample, the maximum displacements at the end of the dwell time were ~ 1890 nm, ~ 2200 nm, ~ 2500 nm for the maximum indenter loads of 250 mN, 350 mN, and 450 mN, respectively. In addition, samples with perpendicular scan direction seem to have lower creep displacement compared to their counterparts. From Fig. 4.6 it is found that, for the 450 mN peak load, creep displacement reaches ~ 2500 nm for both CNPX-big and CNPX-small samples and 2200 nm and 2400 nm for the CNPY-small and CNPY-big samples,

respectively, at the end of the holding stage. No definite pattern was found for creep displacement regarding different scan size at peak loads.
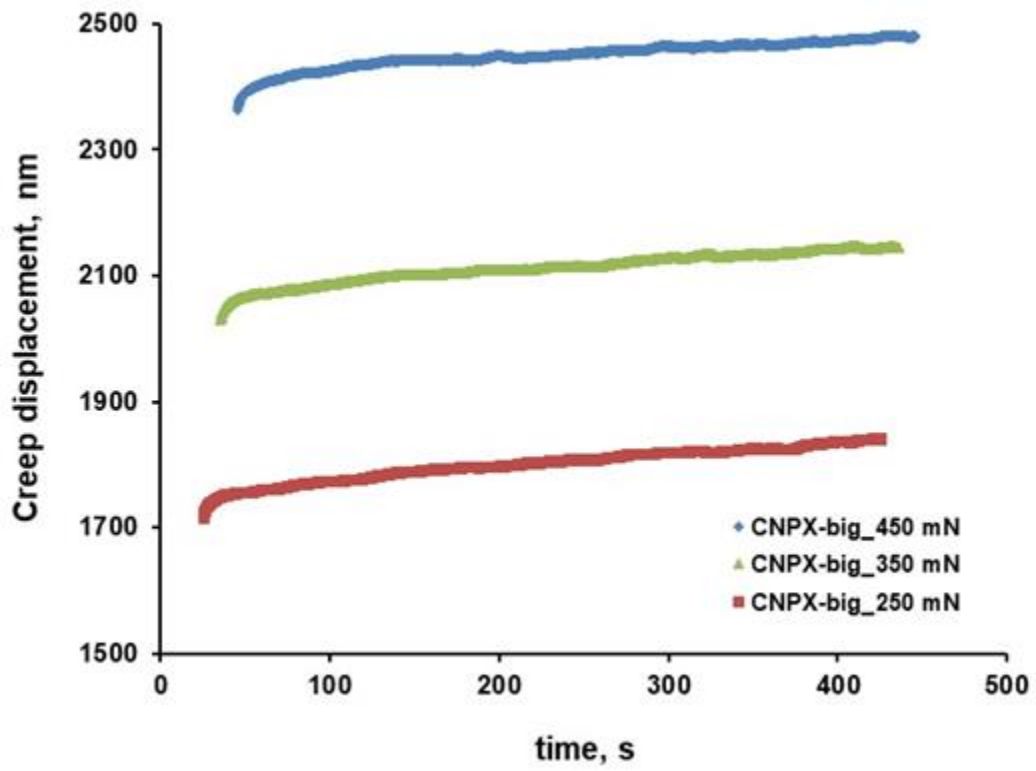
a
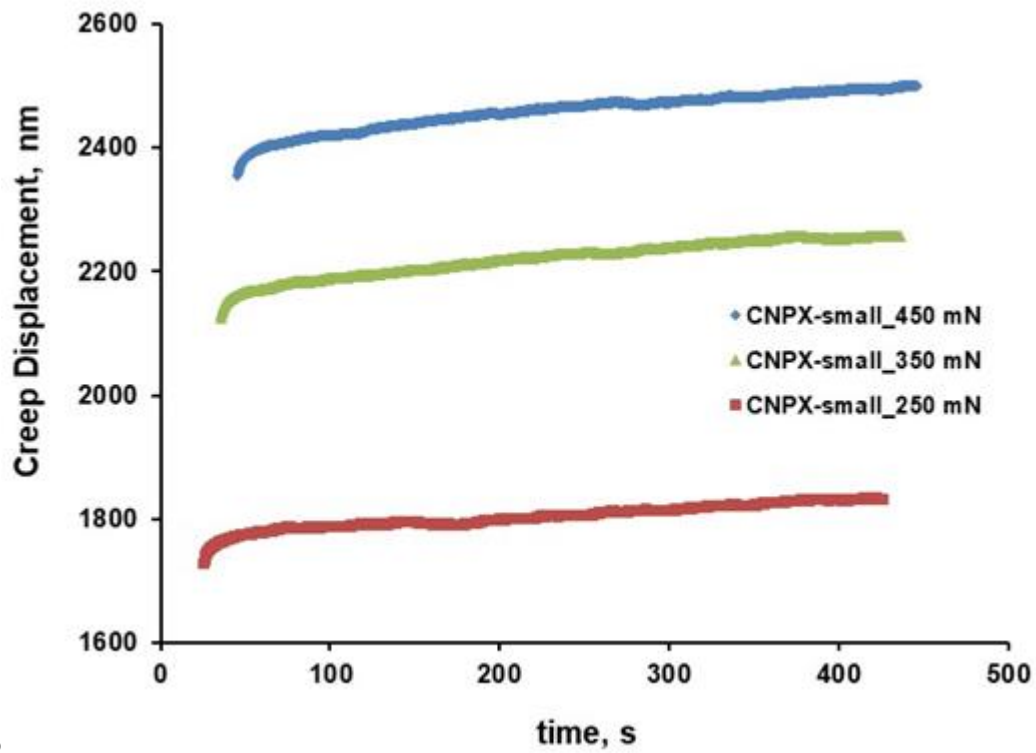
b
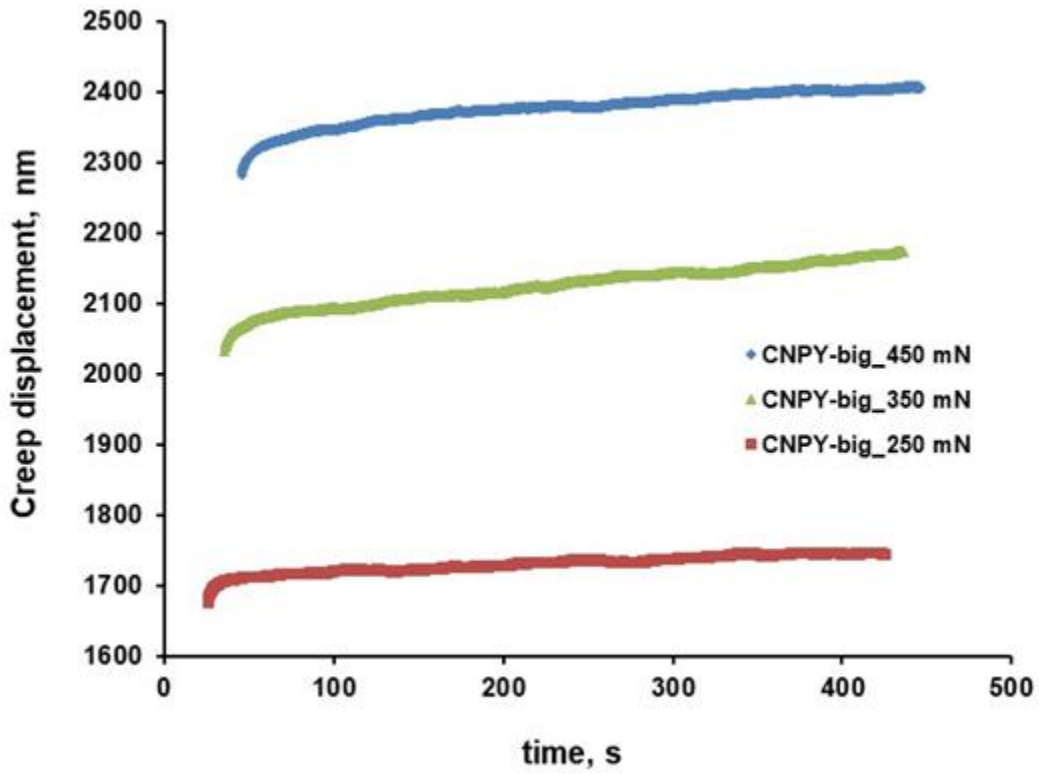
c
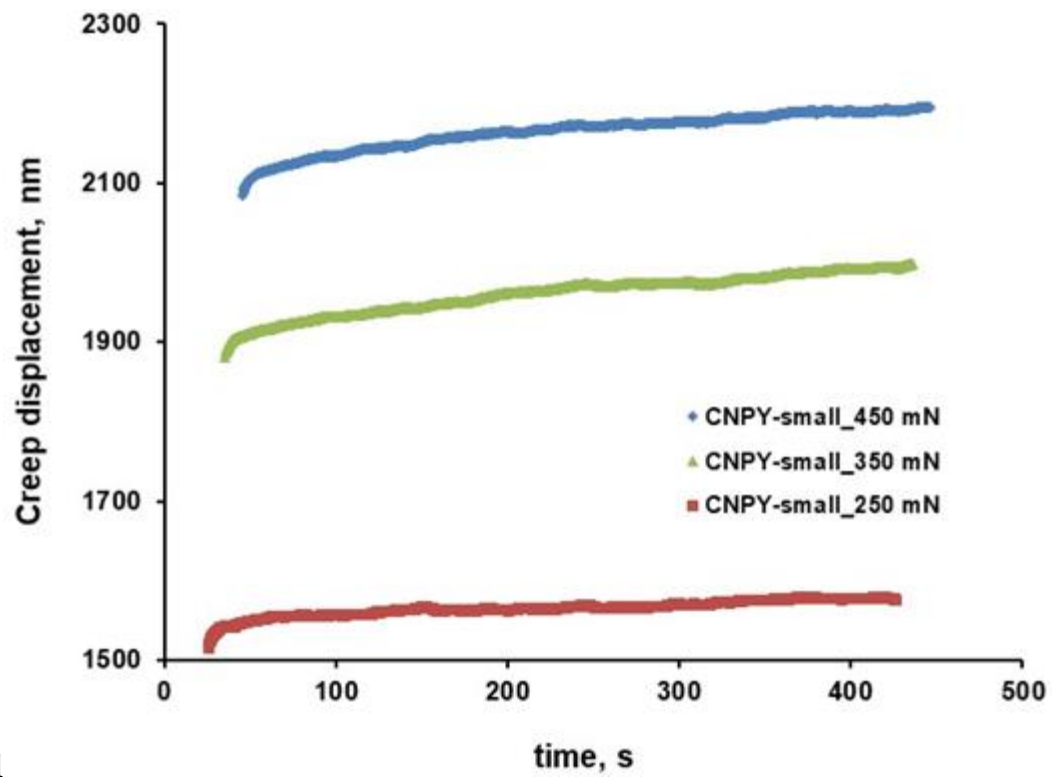
d

Fig. 4.6: Creep displacement vs Constant load holding time at different peak loads for
(a) CNPX-big, (b) CNPX-small, (c) CNPY-small, and (d) CNPY-big.

Indentation creep rates obtained using equation (6) were plotted against holding time, as shown in Fig. 4.7. With the increase in the dwell (holding) time, there is a sharp decrease (transient creep) then plateau trend (steady state creep) in the creep rate. For all four samples, at the loading stage, an initial sharp decrease in creep rate of up to ~ 0.00025 s^{-1} is observed, followed by a nearly steady creep rate at holding time. There are various instances of ambient temperature creep investigations of Ti/ Ti alloys through modelling and/ or traditional creep testing technique and it is difficult to compare the data obtained through traditional creep tests and nano/ micro-indentation creep tests. Harrison *et. al.* developed a numerical model for predicting ambient temperature time dependent strain accumulation for Ti-6Al-4V alloy and at 20°C temperature and at 892 MPa applied stress, ~ 0.17 ks^{-1} creep rate was found [29]. Kameyama *et. al.* investigated ambient temperature creep of commercially pure (CP) Ti manufactured by cold-rolling followed by annealing [7]. More the CP Ti was rolled, creep rate reduced more (38% to 12%) which consequently become almost constant after being rolled-and –annealed (26% creep rate). Neeraj *et al.* studied ambient temperature creep for various Ti alloys of different microstructures and compositions and creep strain was found in the ranges of ~ 0.0006 to ~ 0.03 [32]. Evans [30] studied cold creep of Ti-6Al-4V at different peak loads in the range of 900 MPa to 950 MPa and found strain in the range of ~ 0.04 to ~ 0.14.
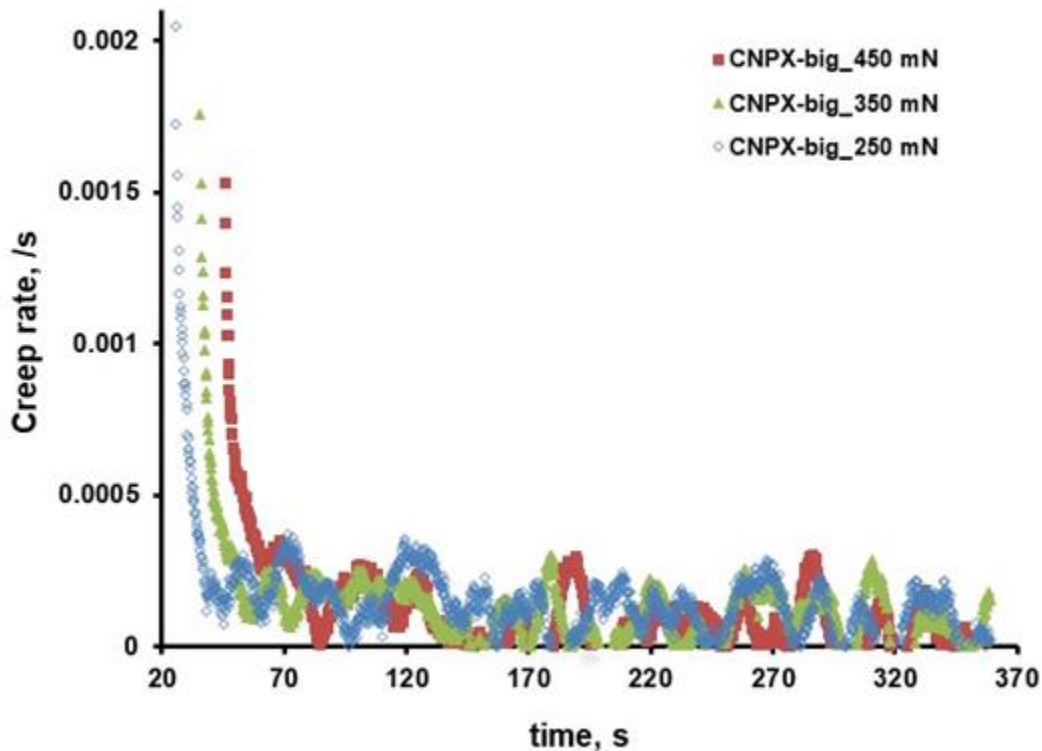
a
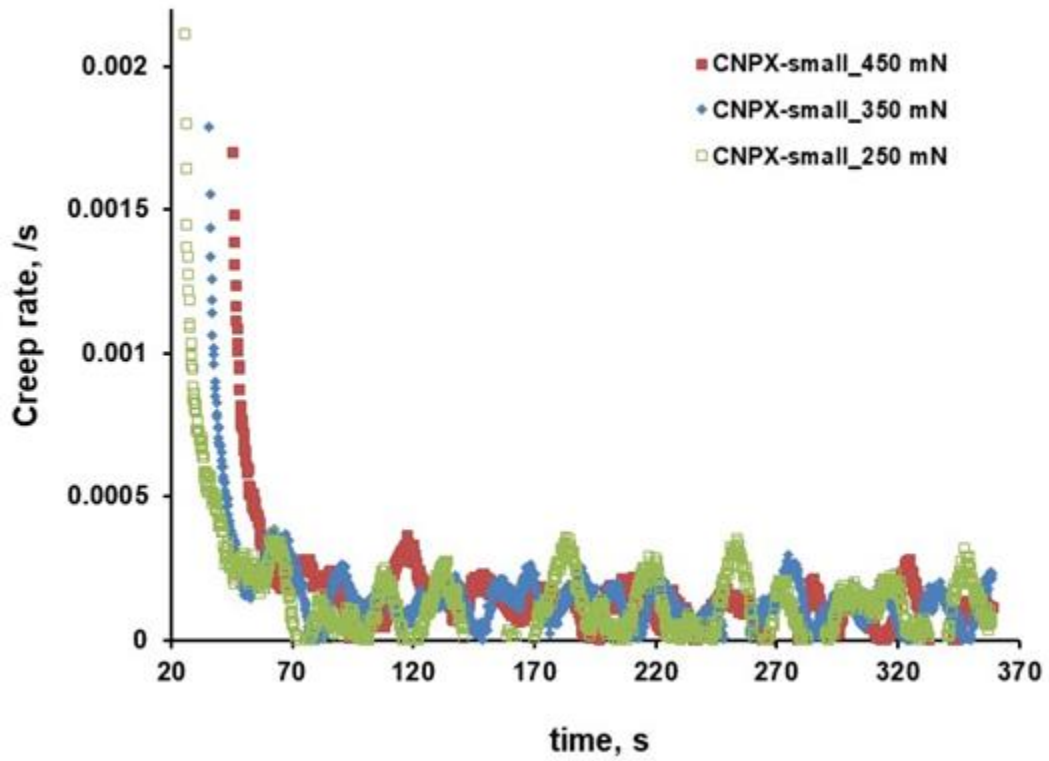
b
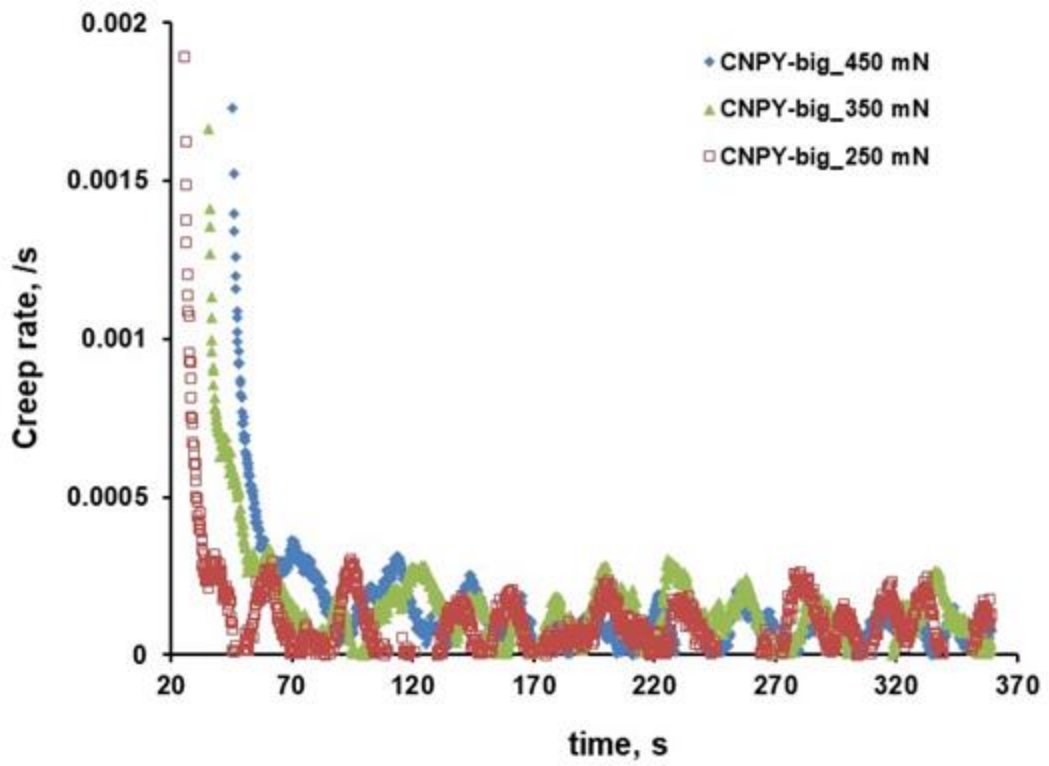
c
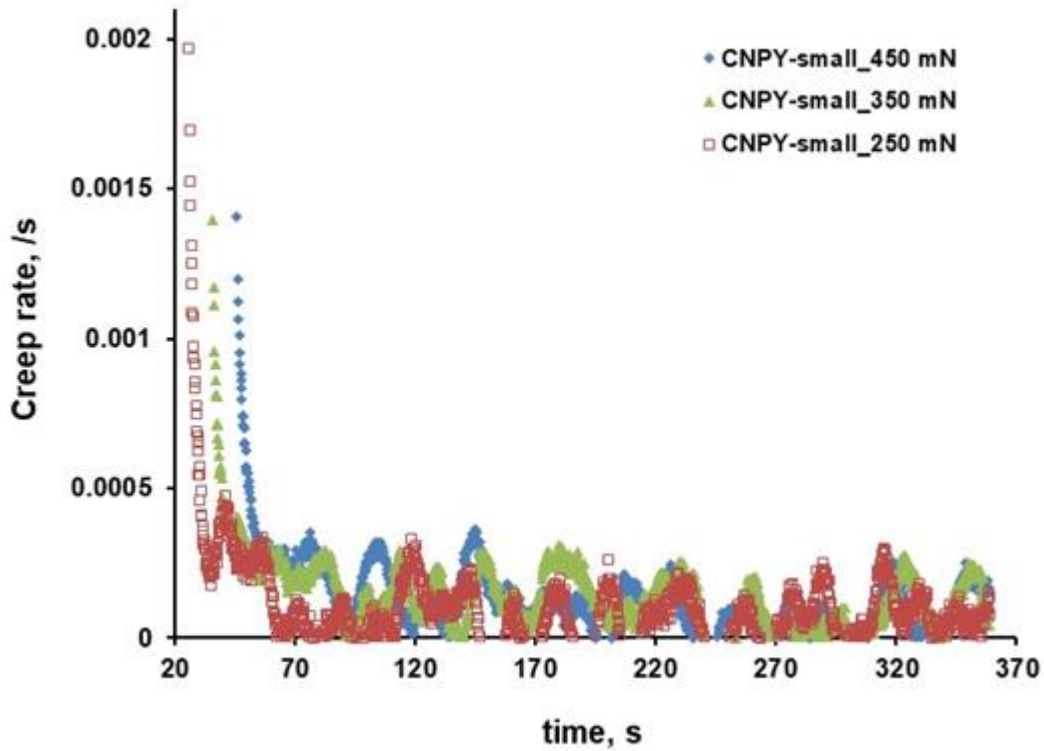
d

Fig. 4.7: Creep rate vs holding time at different maximum indenter load for samples (a) CNPX-big, (b) CNPX-small, (c) CNPY-big, (d) CNPY-small.

In case of crystalline materials under conventional uniaxial tension/ compression, work hardening and increased dislocation density are the reasons behind gradually decreasing creep rates. Secondary, or steady state, creep zones undergoes a dynamic recovery of work hardening by a "softening" effect [161, 162]. From Fig. 4.7, it is found that as the indentation peak load increases, more time is required to start this dynamic recovery, or softening process. As the maximum indenter load increases, the time required to reach the peak load at a constant loading rate of 10 mN/s increases. That is, ample time would be available for the plastic deformation to occur (consume) in the loading stage (the plastic region underneath the indenter gradually increases as indentation depth increases). As a result, less creep is observed in the holding stage, which postpones the dynamic recovery process. Considering creep rate *vs* indentation depth (*h*) curve as shown in Fig. 4.8, it is observed that during the loading stage of all four sample types, creep rate decreases sharply with increasing indentation depth; the shallower the indentation depth, the higher the creep rate. This is followed by an almost constant creep rate in holding stage for all the four samples. From the Fig. 4.8 it is observed that vertically

scanned samples *i.e.* samples having vertical (Y-axis) laser track movement experienced slightly more creep rate than their horizontally scanned counter parts. The reason of this variation of creep rate between horizontally and vertically scanned samples might be attributed to the thermal response during manufacturing of the samples [163, 164]. Alongside, samples with scanning track parallel to flow of argon gas experienced more heat due to temperature convection which results in lower thermal gradient. Whereas, samples with perpendicular/ vertical scanning track experienced less heat which results in lower temperature gradient.

a

b

c

d
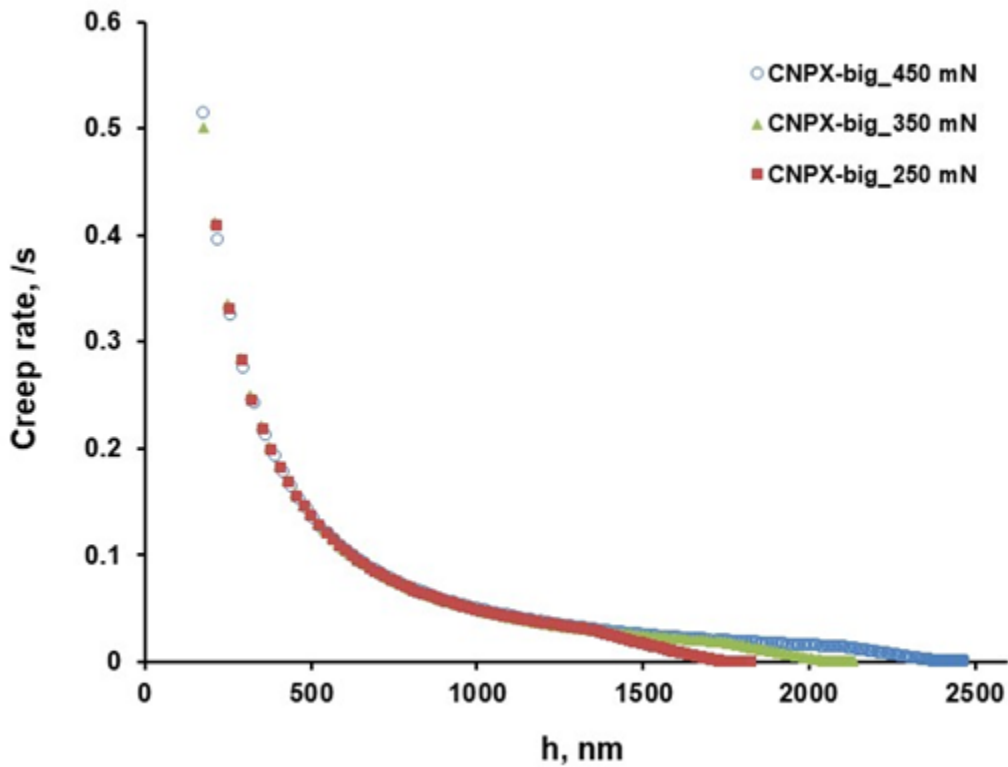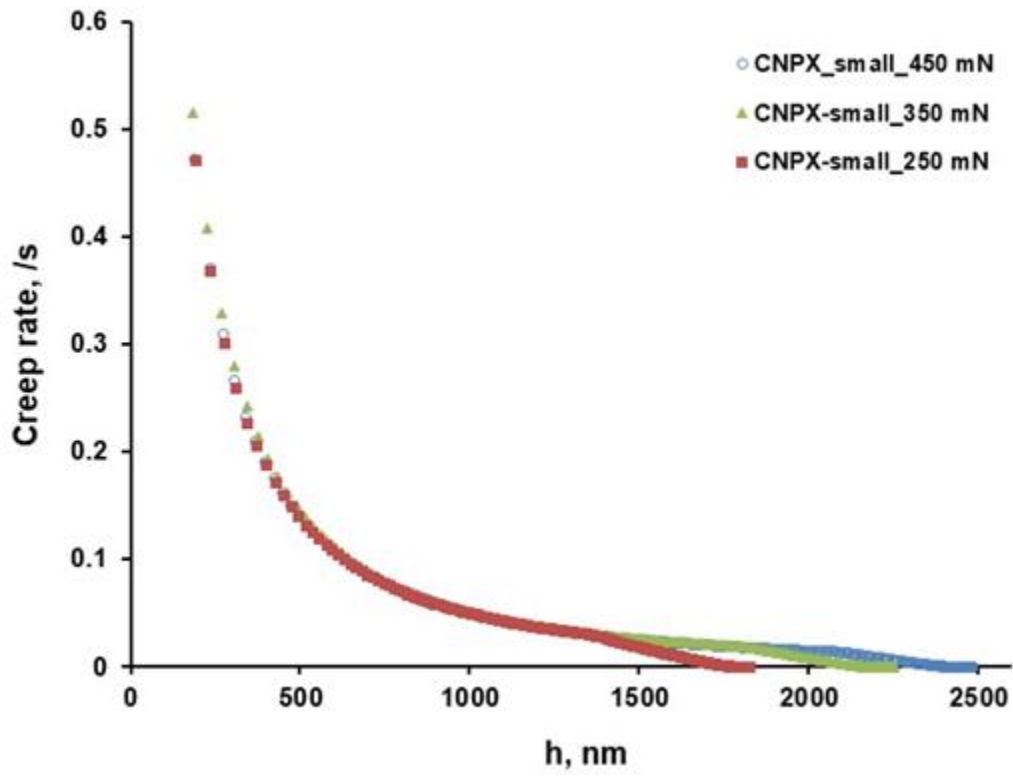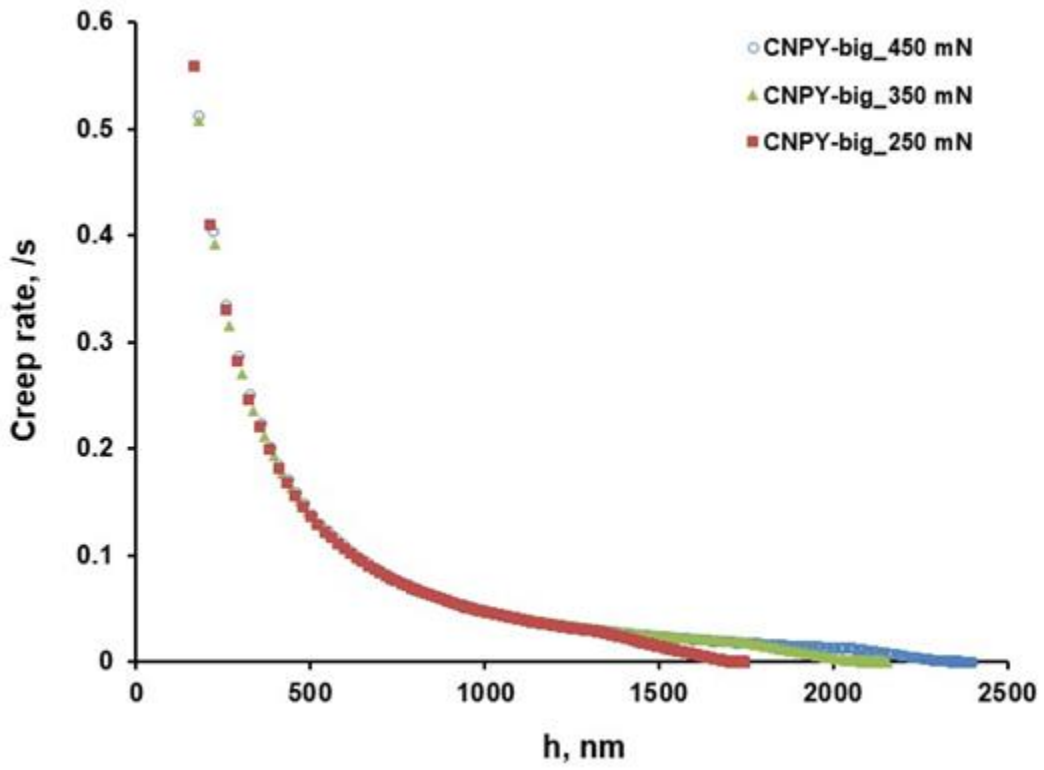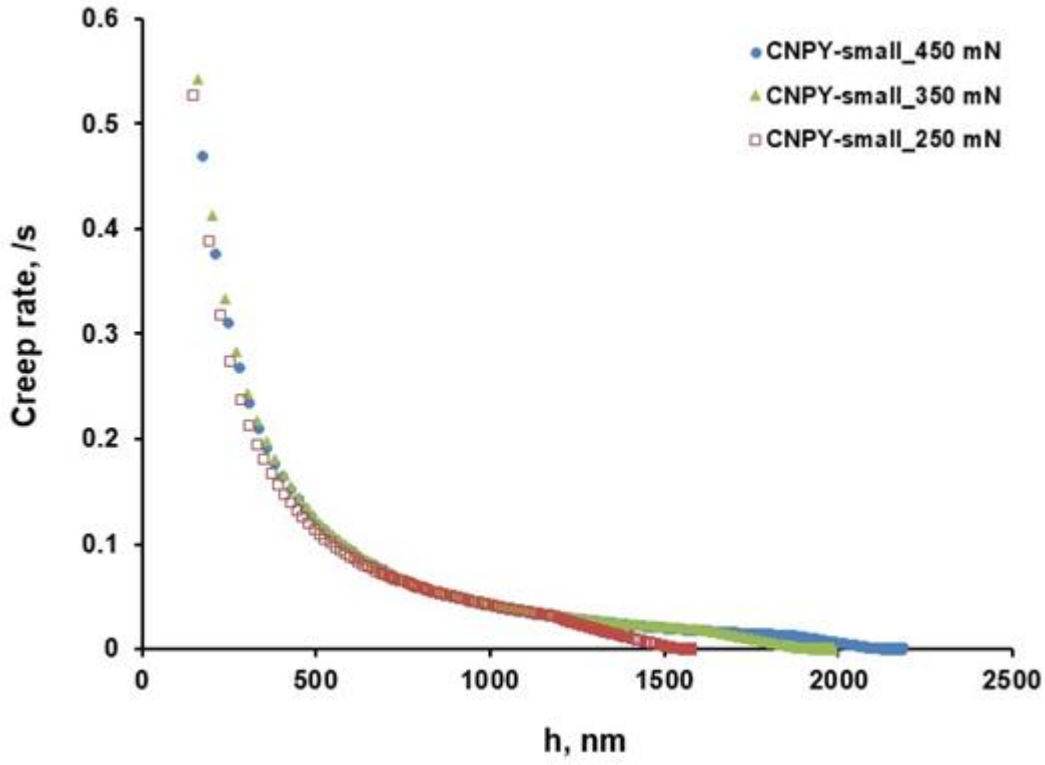
Fig. 4.8: Creep rate vs indentation depth for samples (a) CNPX-big (b) CNPX-small (c) CNPY-big (d) CNPY-small.

4.1.3. Creep stress exponent

The creep stress exponent (n) is used to predict the creep behavior in order to demonstrate creep stability and the dominant creep mechanism during instrumented indentation tests [165]. The creep stress exponents were derived from the slope of ln $\dot{\varepsilon}_{ind}$ versus ln σ_{ind} curves using equations (6), (7) and (10) in the secondary or steady-state creep zone. The creep stress exponent (n) depends on the indention peak load. Since the creep stress exponent (n) is greater than 3 for all samples, the indentation creep mechanism is attributed to dislocation creep [166].

Therefore, dislocation movement dominates the secondary stage *i.e.* steady-state creep in the printed Ti-6Al-4V materials at ambient (room) temperature. This is in agreement with the findings of Ma *et al.* [23] and Liu *et al.* [115], who mentioned dislocation climb as the controlling steady-state creep mechanism for Ti-10V-2Fe-3Al alloy and coarse-grained Ti, respectively. However, though the principal mechanism causing indentation creep is dislocation slip, it has been reported that various other dislocation behaviors, such as

dislocation climb and dislocation nodes, dominate the secondary stage of creep under different peak loads, leading to scattered n values [159].

From Fig. 4.9 depicting creep stress exponent (n) across different samples for different peak loads, it is observed that, in both small and large horizontally scanned samples, the creep stress exponent (n) increases as the indentation peak load increases. There is a small increase in creep stress exponent (n) from the maximum indenter load of 250 mN to 350 mN. When the maximum indenter load is 450 mN, a sudden increase in creep stress exponent is observed in both CNPY-small and CNPY-big samples. From the values of creep stress exponents observed from Fig. 4.9, it is observed that CNPX (horizontally scanned samples) are more ductile than CNPY (vertically scanned samples).
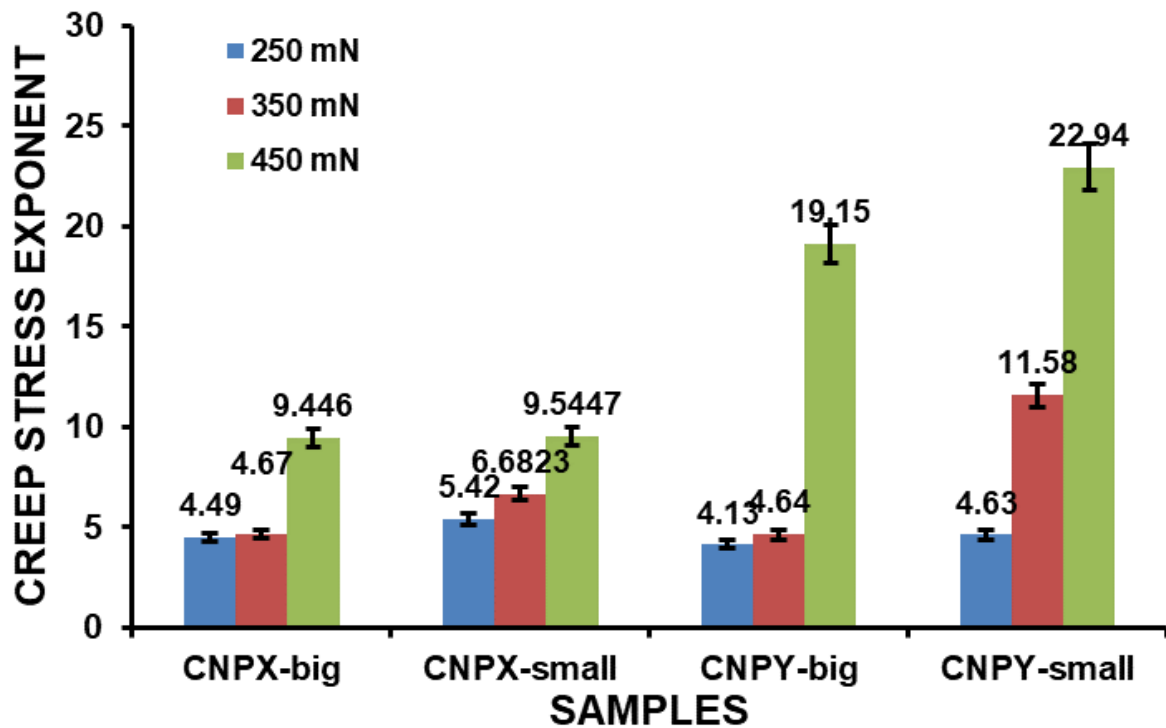
Fig. 4.9: Creep stress exponent (n) across different samples for different peak loads.

The smallest n-value of the studied Ti-6Al-4V alloy was recorded as 4.13 for the CNPY-big sample at 250 mN indentation peak load and highest n-value was recorded as 22.94 for the CNPY-small sample at 450 mN indentation peak load. For the 250 mN and 350 mN maximum indenter loads, n values were discovered to be around ~ 4.5 to ~ 6.5. The measured n-values in the current thesis are in fairly good agreement with results reported by Kral *et al.* [8], who examined the effect of plastic deformation in coarse-grained (CG)

and ultrafine-grained (UFG) Ti-6Al-4V fabricated by multiaxial forging at 648 K - 698 K at stresses ranging from 300 MPa to 600 MPa. In their observation, creep stress exponent (n) for CG alloy was reported as 17, and that of UFG found was measured to be approximately 4. Kral *et al.* [8], using a nano-indentation technique in the UFG and annealed Ti-6Al-4V alloys, reported creep stress exponents of approximately 4 to 5.

4.1.4. Indentation size effect (ISE)

In a depth-sensing (instrumented) indentation test, the representative strain increases with increasing indentation size. Indentation size effect (ISE) is defined as an occurrence where indentation hardness or indentation stress varies as a function of indentation depth or impression size [167]–[169]. The ISE is generally attributed to geometrically necessary dislocations (GNDs) by "mechanism-based gradient plasticity theory" in the plastic zone under indents due to strain [5], [170–172]. Polishing the deformation layer at sub-surface levels may also bestow indentation size effect. The GNDs are nucleated in the material to accommodate the lattice rotation due to indenter penetration. This produces extra dislocation in comparison to uniformly strained material in a very small area just below the indenter. Hence, GNDs may be aligned along non-easy slip crystals, resulting in fundamentally different burger vectors and mobility acting as barriers to ordinary dislocations. Large amounts of GNDs collectively produces strain gradient or work hardening underneath the indenter. Higher indentation loading rate and density of GNDs generates large strain gradients and work hardening effect. Voyiadjis *et al.* [173] examined indentation experiments on various single and polycrystalline materials and came to the conclusion that indentation depth, temperature, and deformation rate all plays vital roles in the strain gradient. Voyiadjis *et al.* [174] also described the effect of grain boundaries (GB) on the dislocation movement pattern during nanoindentation. Unlike the single crystalline metals, the GNDs movements are blocked by grain boundaries in polycrystalline materials, which generate a dislocation pile-up against the GB. As a result, a local hardening is generated in the nanoindentation response due to the GB resistance. The GNDs can move to the next grain when the stress concentration induced by dislocation pile-up reaches a critical value with the nanoindentation response following the conventional size effect pattern. Babu *et al.* investigated nanomechanical behavior for conventionally built Ti-6Al-4V alloy and found strong indentation size effects with gradual decreases of nano-hardness and Young's modulus with the increase

of indentation depth [175]. From Fig. 4.10 showing the indentation stress *vs* indentation displacement curve, strong indentation size effects are observed for the additively manufactured Ti-6Al-4V alloy. In all four sample types with different scan sizes and scan directions, the higher the maximum indenter load, the larger the indentation displacement observed.

a

b

c

d
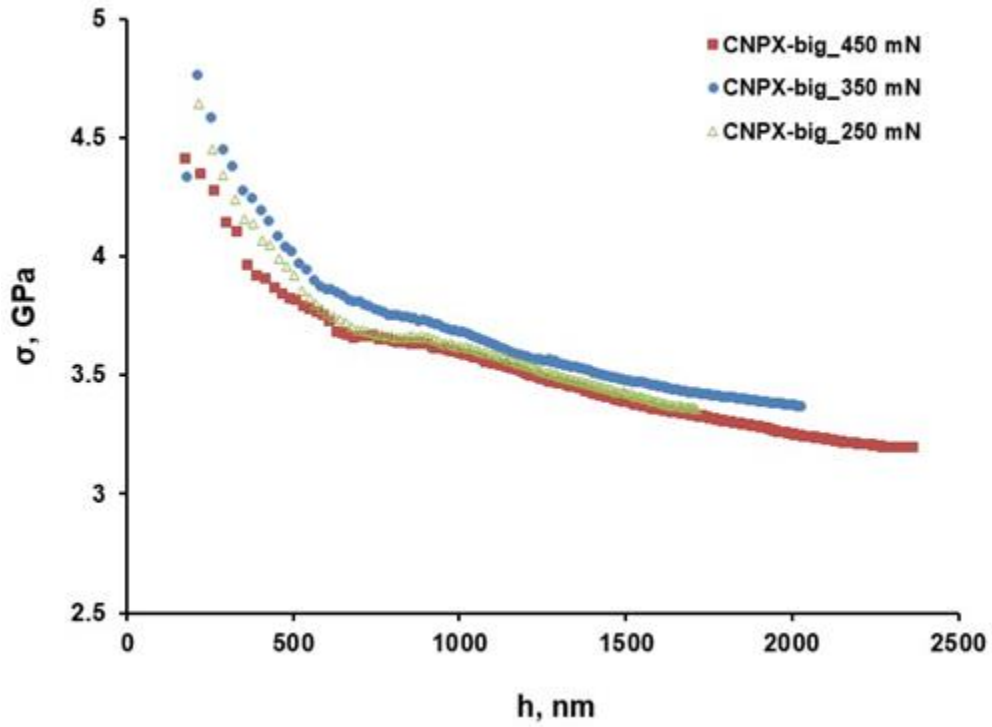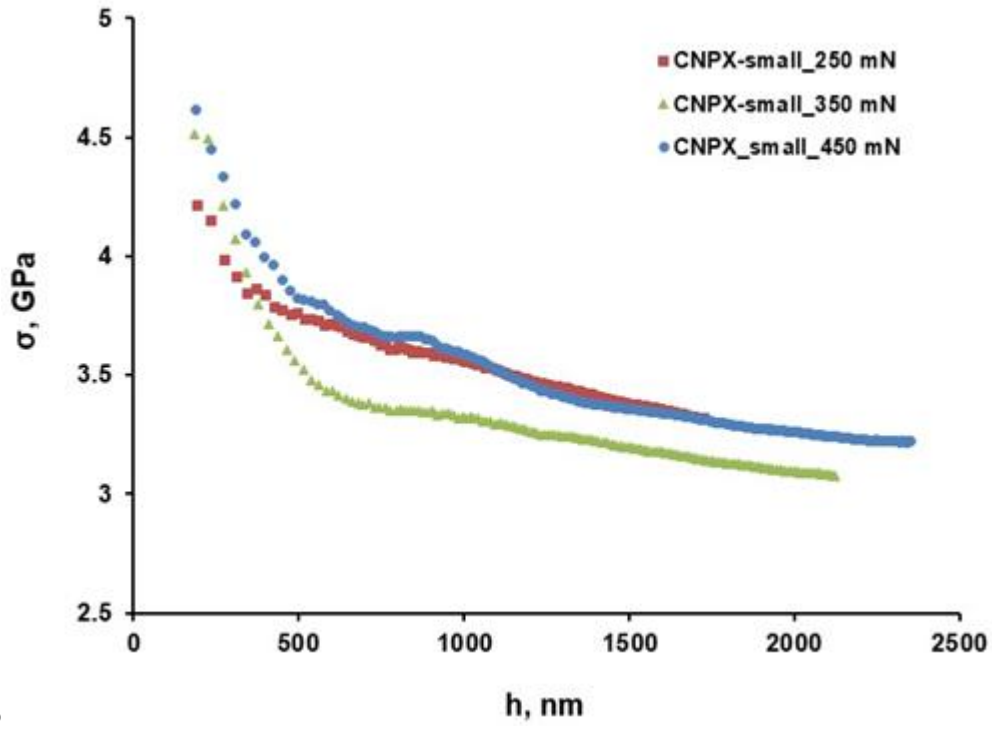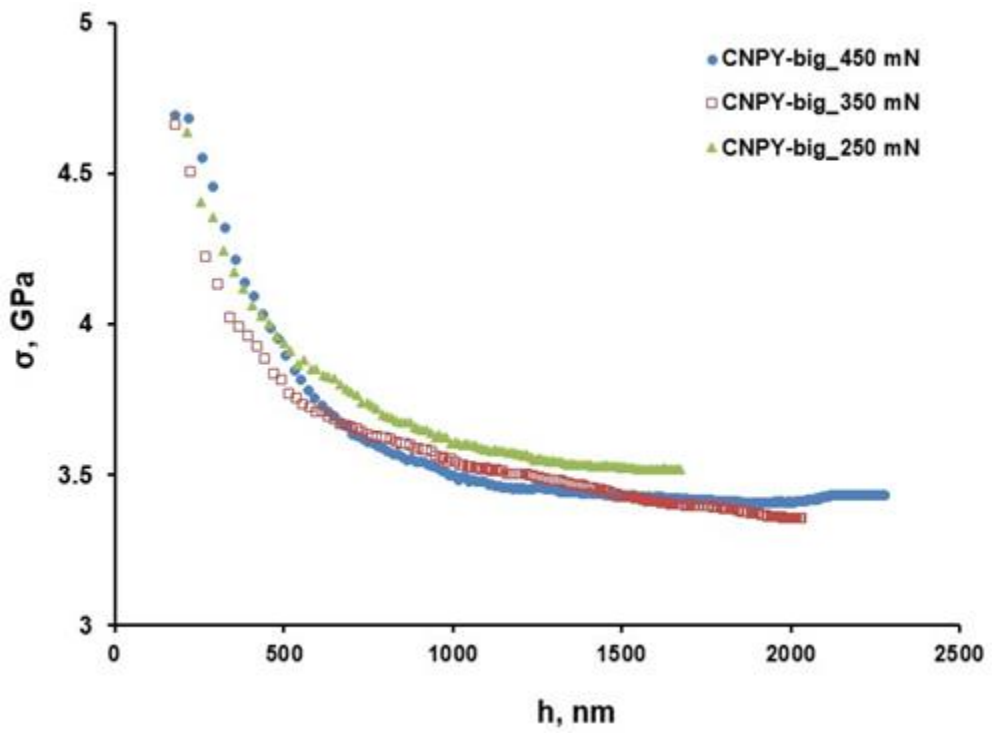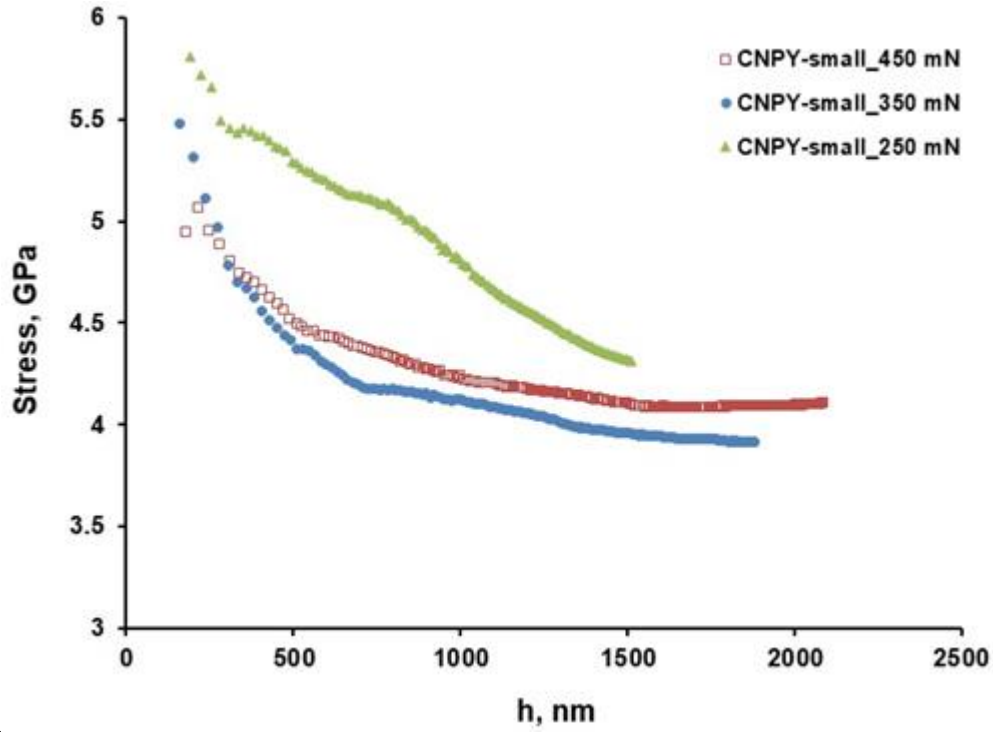
Fig. 4.10: Indentation size effect (ISE) under different maximum indenter loads for sample (a) CNPX-big, (b) CNPX-small, (c) CNPY-big, (d) CNPY-small.

4.2. Effect of various heat treatment cycles of Ti-6Al-4V alloy

4.2.1. Microstructure

Cooling rate, time, and temperature are the main parameters of heat treatment which affect the final microstructure of the Ti-6Al-4V alloy. In this study the samples were solutionized at 950°C for 1 hour with the purpose of studying the effect of different cooling rate from below β- transus temperature on the resultant microstructure and micro-mechanical properties were studied. Various cooling rates produce different microstructure as shown in the continuous cooling transformation curve (CCT diagram) (see Fig. 4.11).
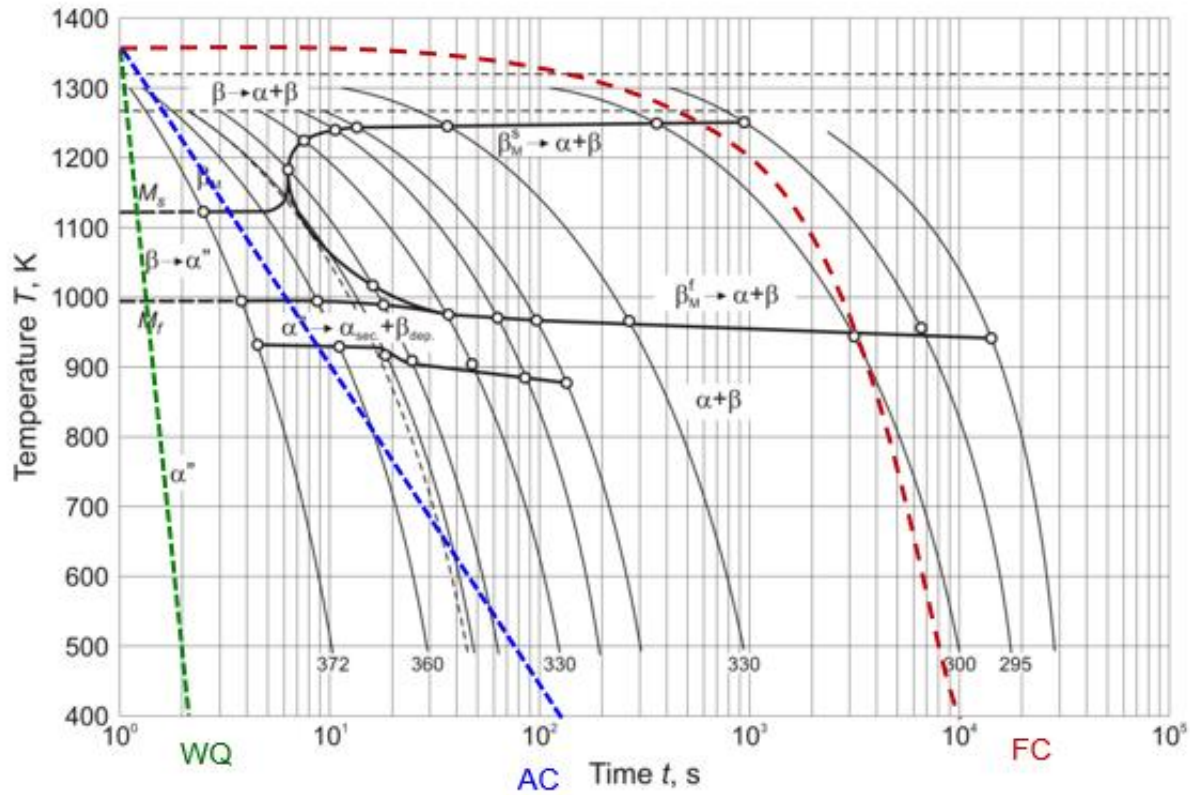
Fig. 4.11: CCT diagram for Ti-6Al-4V alloy showing cooling curves of three different cooling methods (water quenching, air cooling, and furnace cooling) [176].

Figs. 4.13 and 4.14 show the optical and scanning electron microscopy images of the Ti-6Al-4V alloy in the as-printed and heat treated conditions. In the as-printed samples, the size of α colony is determined by the cooling rate experienced during printing from β phase and β grain size. Additive manufactured α-β Ti-6Al-4V alloy is typically characterized with prior β grains that generates in an epitaxial way through several layers, consisting of grain boundary α, martensitic $\acute{\alpha}$, and α lath size [95, 177, 178]. The microstructures of the Ti-6Al-4V alloy can be typically described as primary α, secondary α, colony α, plate-like α, and hcp martensite (α''), acicular α, grain boundary α, basket-weave structure [179], and Widmanstätten structure [180]. The terms basket-weave structure, Widmanstätten structure, and acicular are often used to be interchanged [44]. In the Ti-6Al-4V alloy manufactured by the L-PBF processes, an α-β lamellar structure associated with α-phase lamellae in a β-phase matrix is created due to the low to intermediate cooling rates. The α-lamellae are created by diffusion controlled nucleation and growth of α platelets into β-grains [153]. In additively manufactured Ti-6Al-4V alloy,

94

size of these α platelets is controlled by the cooling rate; an increased cooling rate results in a decreased diffusion rate, which subsequently leads to decreased length and thickness of the α-lamellae associated with higher yield strength [154]. The prior β grain size is typically determined by the time the material is exposed to above β transus temperature, which is generally around 995 °C for the Ti-6Al-4V alloy [181].

Considering the cross-sectional microstructural morphology in Figs. 4.12 and 4.13, it is observed that the growth of the prior β grains is parallel to the scanning direction. It is further noticed that the columnar shape of the prior β grains is prolonged along the building direction *i.e.* along bottom surface to top surface. The columnar shape is formed by the epitaxial growth of the original β phase due to successive layer deposition and the temperature gradient along the building direction of the L-PBF process. Moreover, "No post" (*i.e.* partly re-melting the formed columnar grains by laser beams) treatment was performed while printing the samples resulting in the epitaxial growth of the grains [38].

It is quite possible to get an estimation of the mechanical properties of the different materials through microstructural characterization. The α colony size, a microstructural feature, is known to be most important mechanical properties since it correlates with the slip lengths of the material [182]. Smaller α colonies contributes to higher strength, and their size correlates with α lath and grain boundary α thickness. Prior β grain boundary determines the size of the α-colony. Faster cooling rate decreases the size of the α-colonies along with the size martensitic $\acute{\alpha}$, α laths, and grain boundary α. From Figs. 4.12 and 4.13, it is observed that the size of α colony is very fine in the PH sample rendering highest strength of all the heat treated samples, followed by AC, FC, as-printed, and WQ samples.

Thijs *et al* observed formation of intermetallic phase Ti_3Al precipitation at high heat input when the temperature reaches at 500°C-600°C [137]. Due to rapid solidification and the effect of heat by the scanning of following layers during printing operation, segregation of Al leading to the precipitation of an intermetallic Ti_3Al phase occurs at grain boundaries. Solubility of Al is very low in Ti and it causes solid solution strengthening along precipitation strengthening [183]. Due to short interaction times coupled with highly localized heat input, large thermal gradients exist during the process leading to build-up of thermal stresses. Alongside, rapid solidification leads to segregation phenomena along with the development of non-equilibrium process [10].

From Figs. 4.12 and 4.13, it appears that, after performing heat treating at 950°C, primary α became significantly coarser, slender, and shorter which is similar to the observation of Vrancken *et al.* [10]. The WQ sample is the softest one as this sample is solutionized and then water quenched. The expected state of material is known as supersaturated solid solution (SSSS). Upon holding for 1 h at 950 °C, various precipitates and strengthening phases are dissolved in the matrix and any segregation present in the alloy is reduced. Upon quenching, the SSSS which is in an un-equilibrium state is formed. Here, the atoms do not have time to diffuse to potential nucleation sites and therefore the precipitation do not form. Heating the α-β Ti-6Al-4V alloy to the solution treatment (solutionizing) temperature produces a higher ratio of β phase. This partitioning of phases is maintained by quenching which results in a soft microstructure. Besides, due to too fast cooling rate in the WQ sample, there will not be sufficient time available for the microstructural transformations which results in the formation of large density of entrapped gases, defects, voids, and porosities which adversely affect the strength of the material. Due to rapid cooling rate, upon water quenching, it is assumed that martensitic α'' is developed in prior β grains.

Subtransus heat treatment followed by air cooling and furnace cooling show almost similar microstructure evolution. In AC samples, soluntionizing at temperature 950⁰C strongly promoted grain growth, as clearly shown in Figs. 4.13(c) and 4.14(c). Due to a relatively higher cooling rate in comparison to the furnace cooling, the β phase is transformed in to a finer lamellar structure in the air cooled sample. When the heating temperature was increased to 950⁰C, a transformed β structure which is also known as bi-lamella structure started to appear in the air-cooled samples formed by secondary α laths precipitated in the β matrix [182]. The heat treatment did not eliminate the microstructural anisotropy and was accompanied with α'' decomposition, lamella growth and diffusion. The stable interwoven microstructure of the initial martensite severely hindered the grain growth.

In subtransus heat treatment followed by furnace cooling, due to low to intermediate cooling rate, α-lamellae are created by diffusion controlled nucleation and growth of α platelets into β-grains [184]. During subsequent heat treatment, the $\acute{\alpha}$ phase in the L-PBF fabricated Ti-6Al-4V alloy is expected to slow down the growth of new grains formed, leading to a fine $\alpha+\beta$ lamellar structure. After solutionizing, the $\acute{\alpha}$ phase was partially

decomposed but the prior $\acute{\alpha}$ phase is still clearly visible. As stated in different literature [185], the decrement of dislocation density in the α phase and the decomposition of the $\acute{\alpha}$ phase are the two prime microstructural changes observed during the stress-relief heat treatment. Typically, α colony is created from the β single-phase field during slow cooling after an annealing treatment and the prior β grain size restricts the initial α colony size. In the case of the L-PBF fabricated Ti-6Al-4V alloy, during subsequent subtransus treatment the initial acicular martensite $\acute{\alpha}$ gradually decomposes into $\alpha+\beta$ in the shape of colony containing parallel α lamellae. Vrancken *et al.* [10] had almost similar observation. Vrancken *et al.* [10] observed that after heat treating for 2 h at 780°C, followed by furnace cooling (FC), the fine martensitic structure has been transformed to a mixture of α and β, in which the α phase is present as fine needles. After conducting heat treatment below the β transus and at sufficiently low cooling rates, due to the formation of a layer of grain boundary α and the more aggressive etching of the $\alpha + \beta$ mixture as opposed to the original α', the prior β grains became even more visible. However, the microstructure no longer contained long columnar prior β grains after treatment above the β transus, indicating extensive grain growth of the SLM material, up to the point of semi-equiaxed β grains. Studies by Sercombe et al. [37] Vilaro et al. [38] have reported similar results regarding this microstructural transformation.

In the precipitation hardened (PH) sample, as shown in Figs. 4.12 (e) and 4.13 (e), both α and β phases compete with each other to coarsen simultaneously but effectively hindered each other's growth, leading to a compact microstructure. Moreover, some nano-sized particles are found to be dispersedly distributed on the α-laths and α phase grain boundaries of the air cooled sample (see Fig. 4.14). There are limited reports of these nano-size particles generated in SLM Ti-6Al-4V alloy in the literature till date. These nano-sized particles are identified as the nano-sized β particles [186]. The nano-sized β particles also were observed in the spark plasma sintering fabricated Ti-6Al-4V alloy after aging at 450 °C [187]. Zhang *et al.* [188] through XRD patterns concluded that the nano-sized particles are nanaosized β particles in α phase matrix. In the current research, it was observed that the cooling rate influences this decomposition of nano-sized particles, indicating these particles to be metastable and temperature sensitive. As showed in Fig. 4.14, during the furnace cooling, some of these nano-sized particles dissolved into the α-matrix, which is similar to the observation of Zhang *et al.* [188].
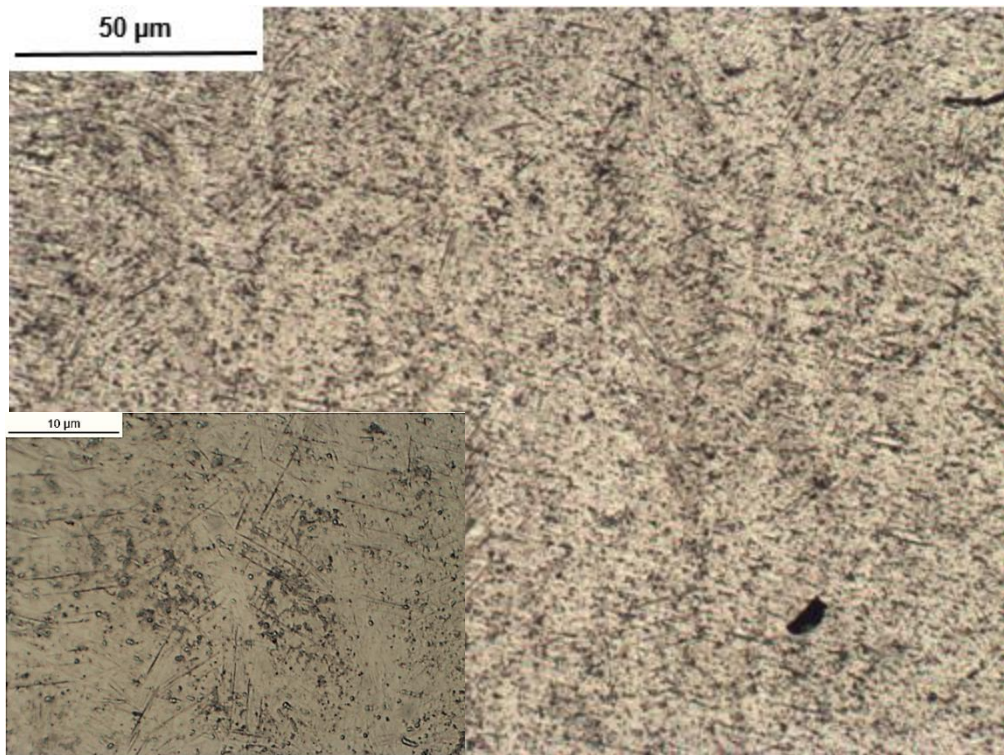
a
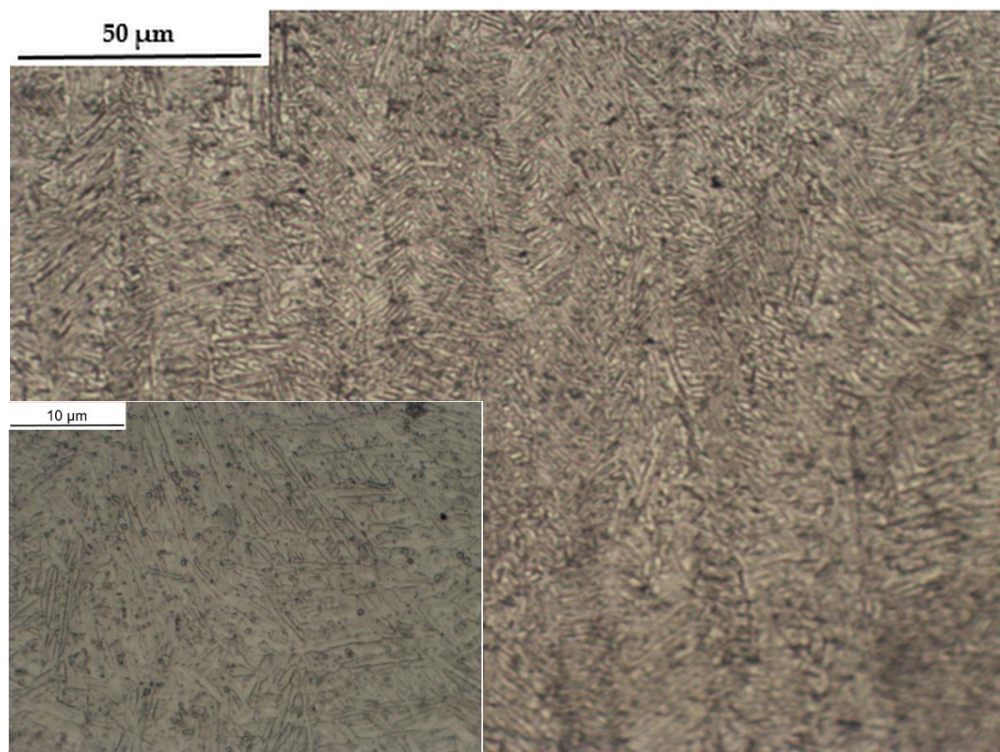
b
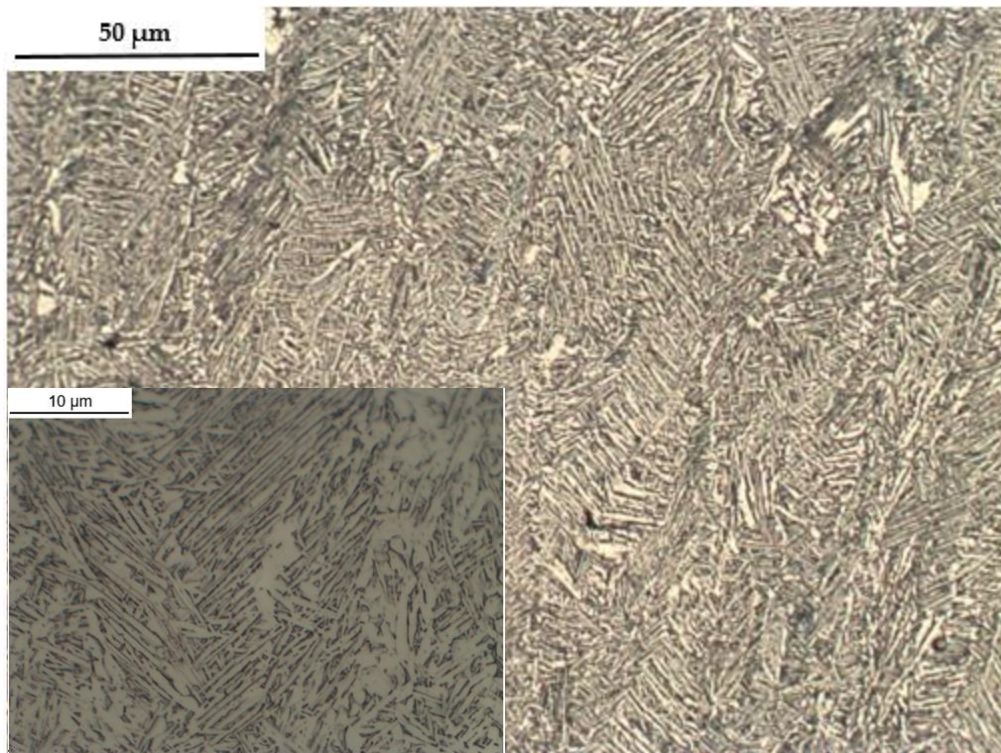
c
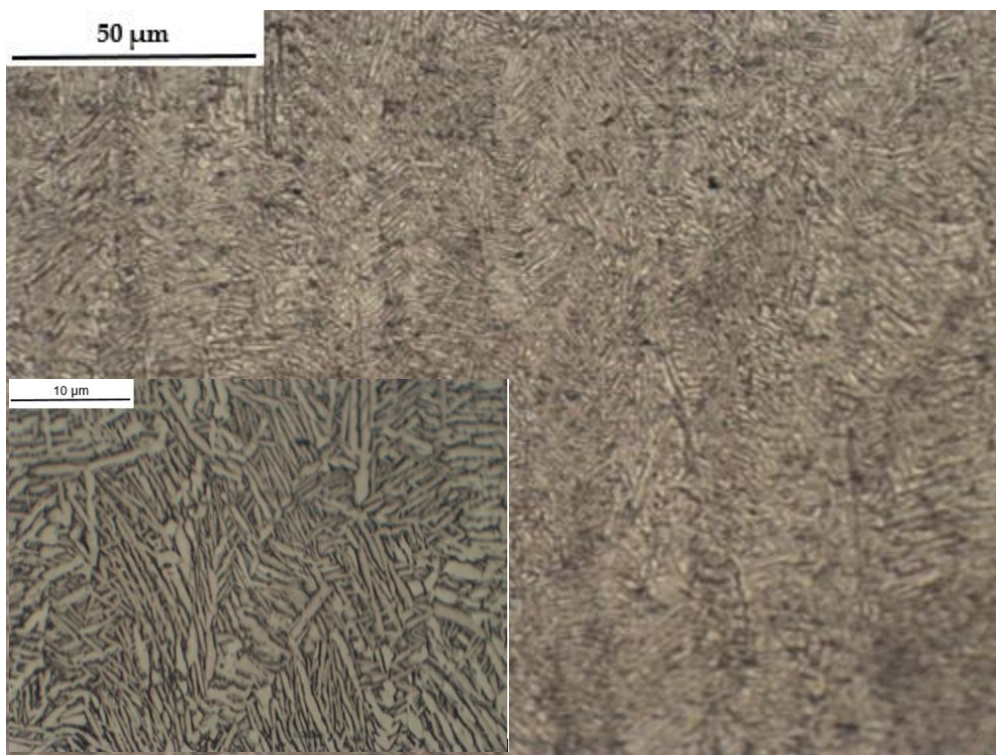
d
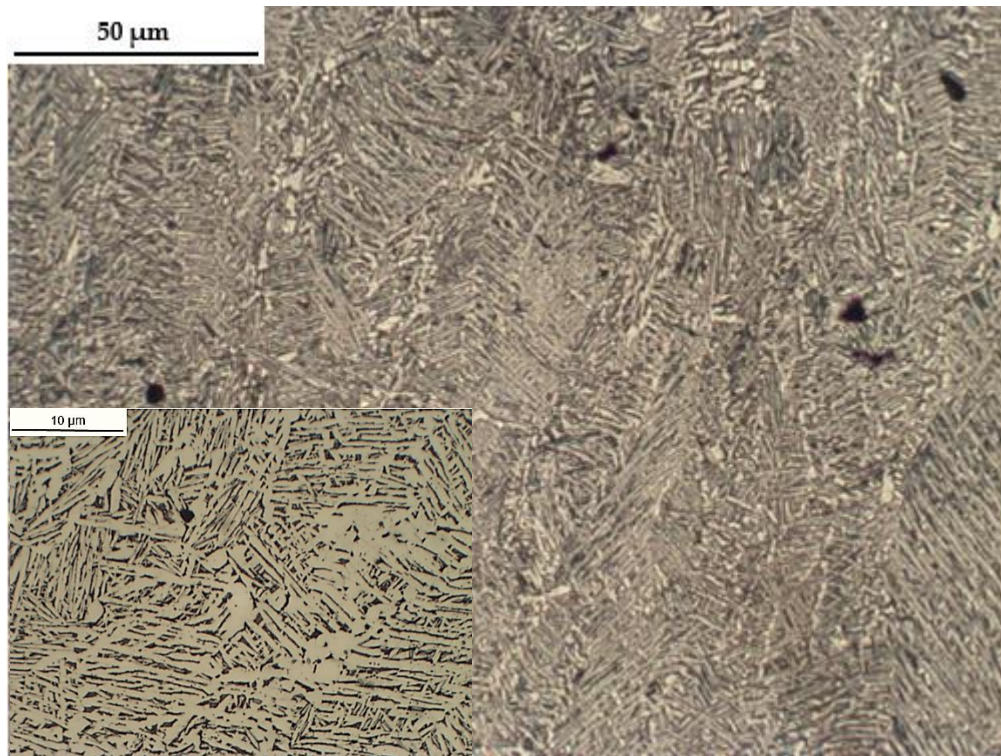
e

Fig. 4.12: Optical microscopy of (a) as-printed, (b) water quenched (WQ), (c) air cooled (AC), (d) furnace cooled (FC), and (e) aged (PH) microstructures.

a

b

c

Prior β grain boundary
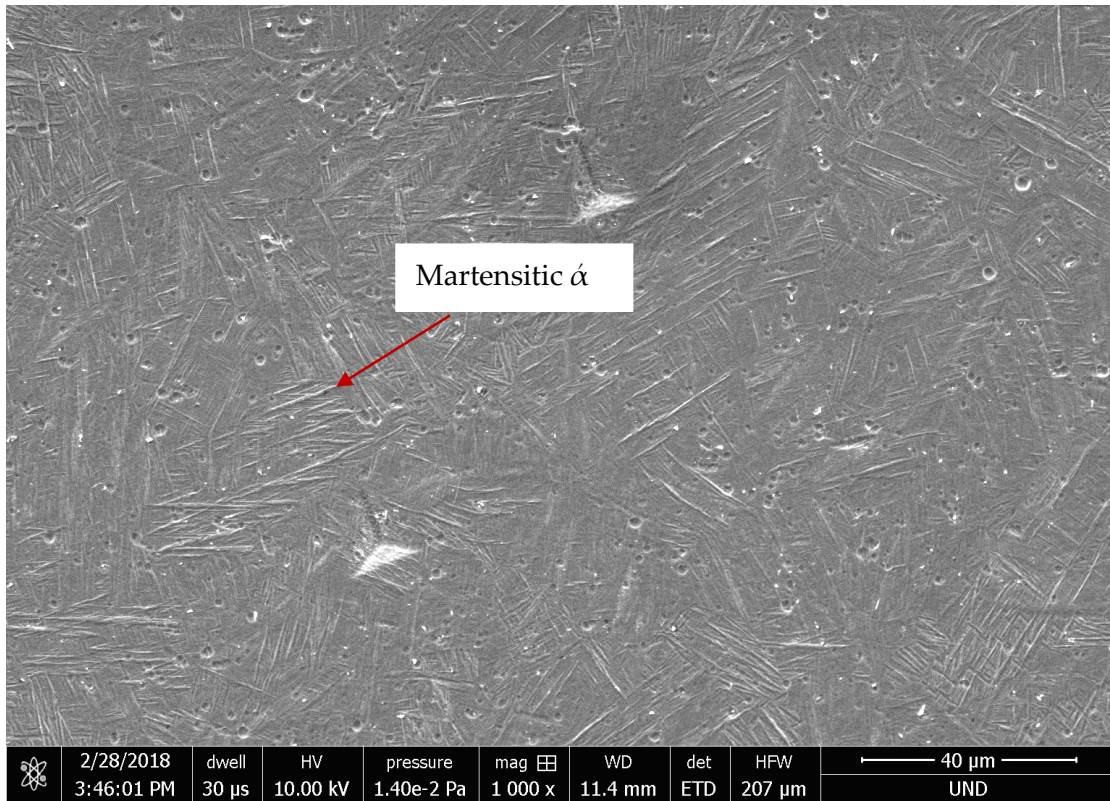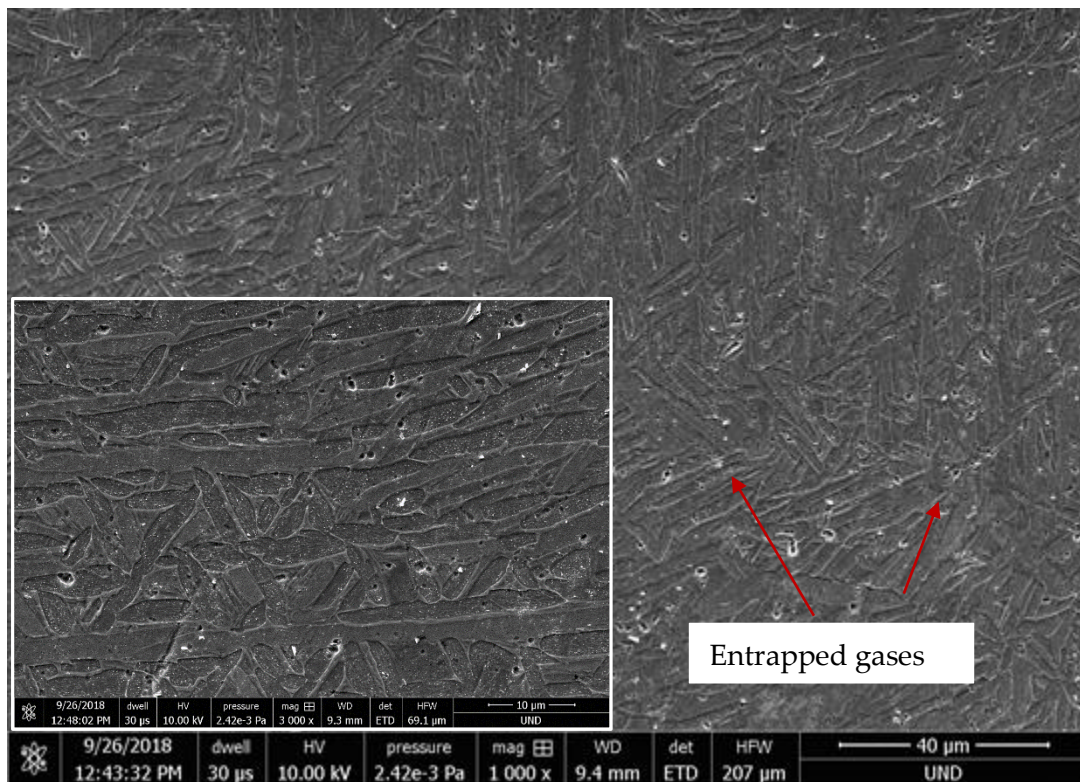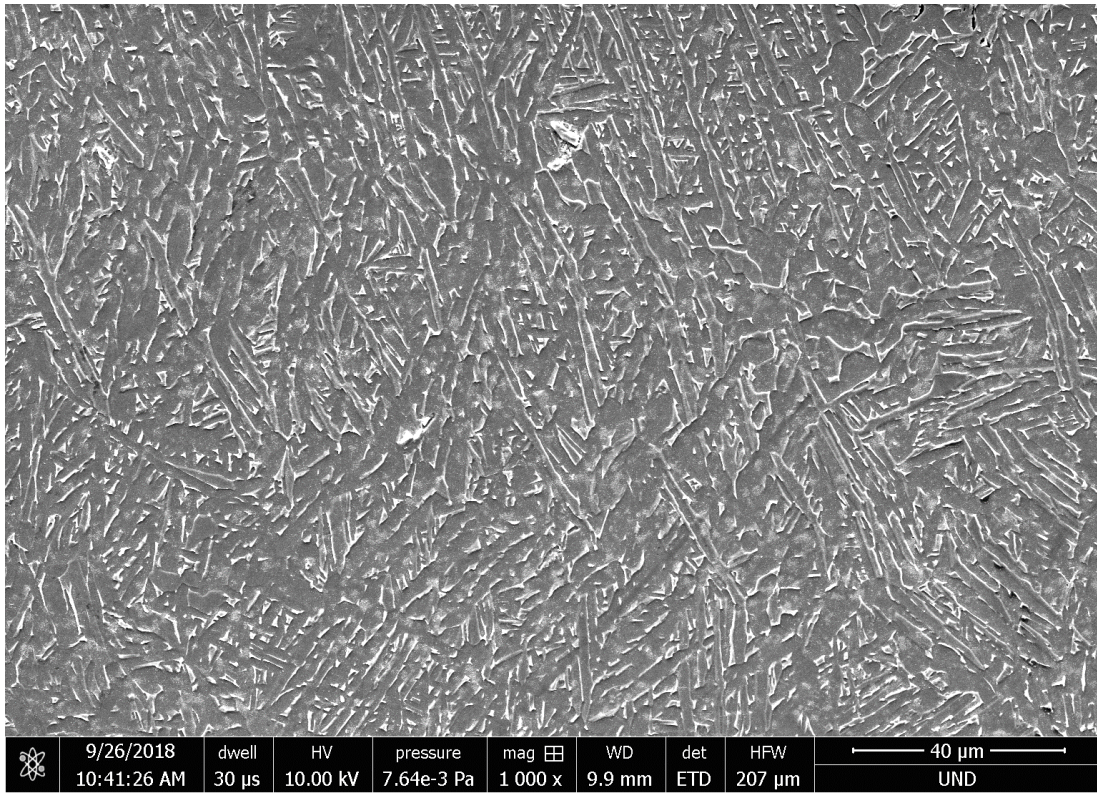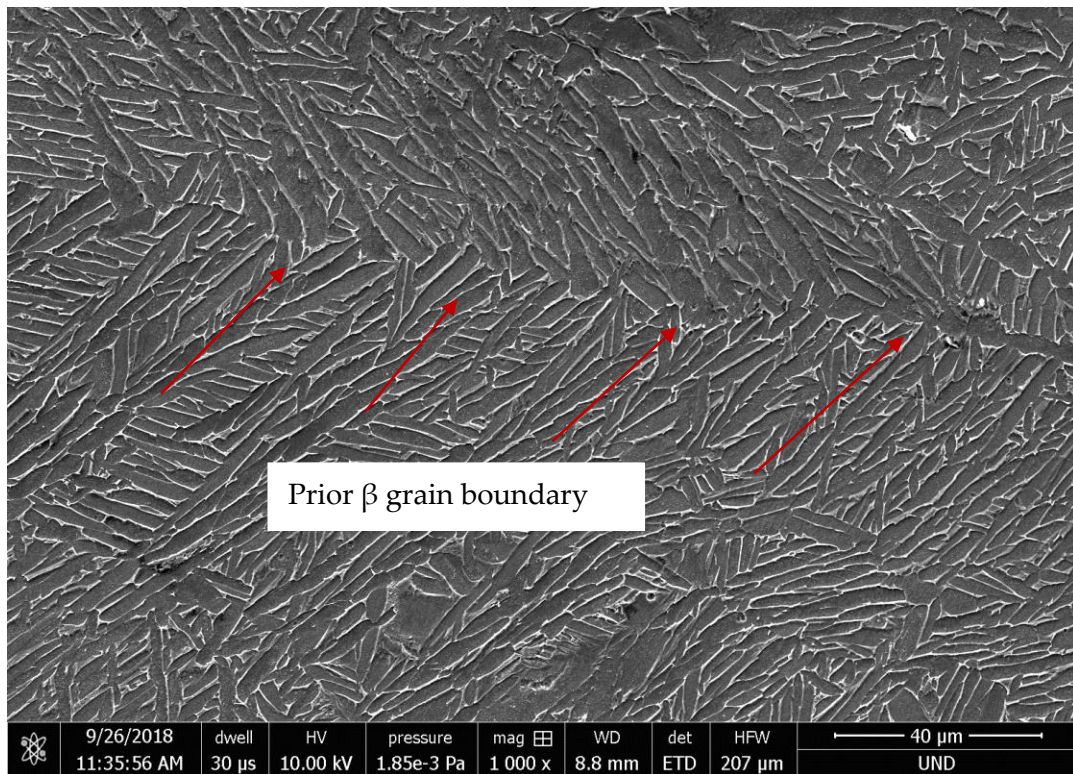
d
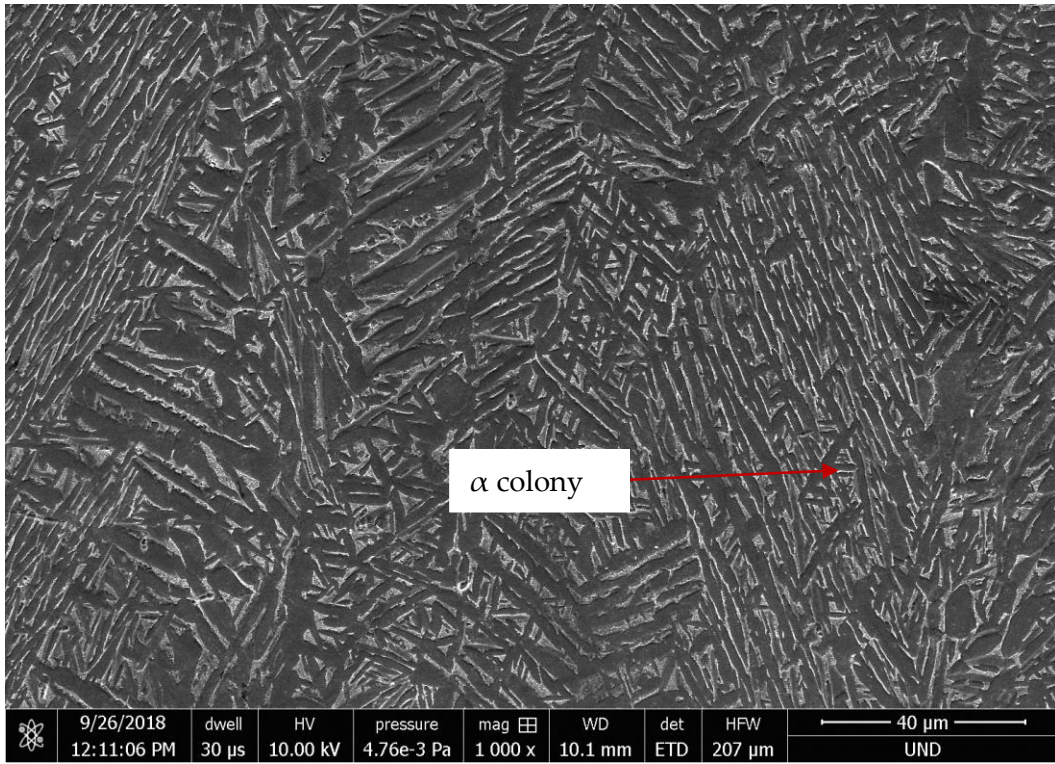
e

Fig. 4.13: SEM images of (a) as-printed, (b) water quenched (WQ), (c) air cooled (AC), (d) furnace cooled (FC), and (e) aged (PH) samples
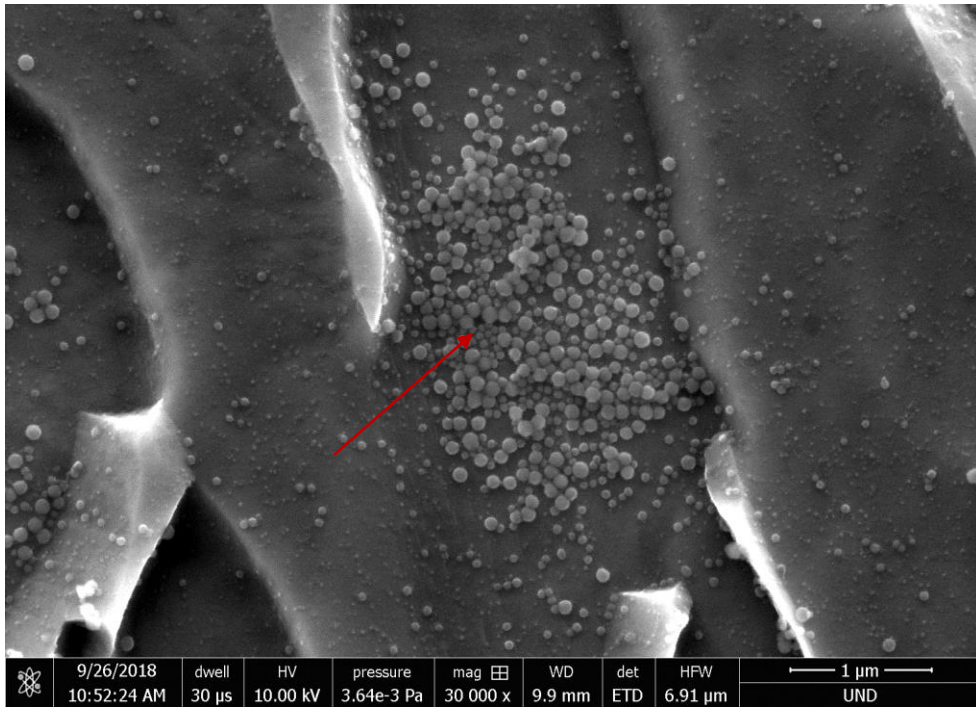
a
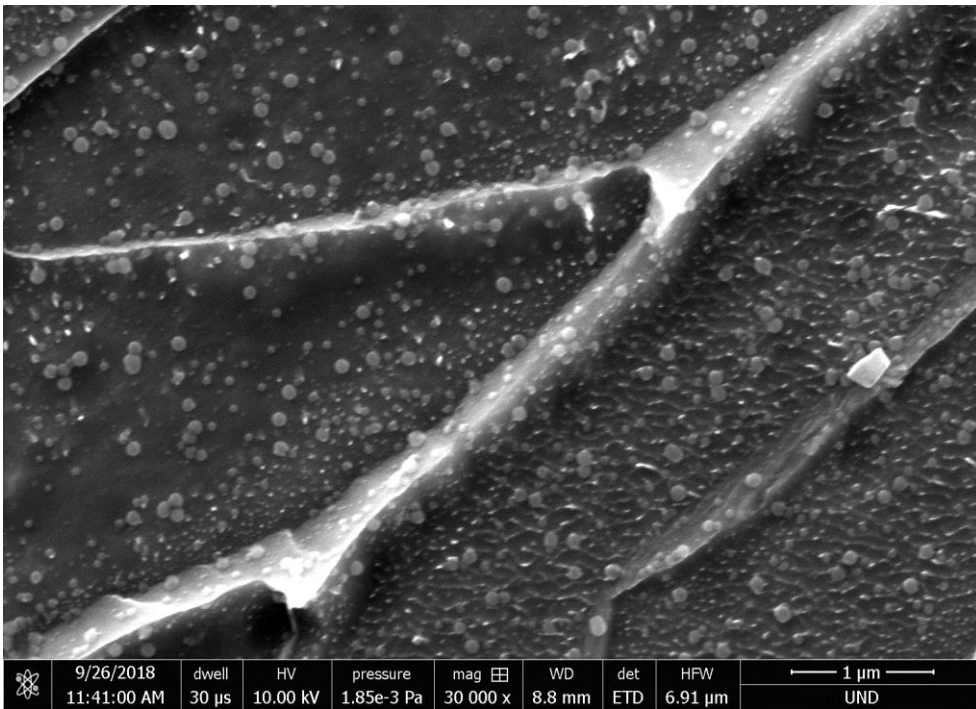
b

Fig. 4.14: (a) Nano-sized particles in air cooled sample in AC sample, (b) nano-sized particles being dissolved in FC samples

4.2.2. Microhardness

The Vickers microhardness evolution of the Ti-6Al-4V alloy produced by the L-PBF followed by various heat treatments is presented in Fig. 4.15. The as-received L-PBF Ti-6Al-4V sample consists of martensitic $\acute{\alpha}$ microstructure with an average hardness number of 358.63 $HV_{0.5}$. The microhardness values were increased for the AC and FC samples. With air cooling, average microhardness of 476.46 $HV_{0.5}$ and with furnace cooling, average microhardness of 389.91 $HV_{0.5}$ were measured. The micro-hardness of the water quenched sample (SSSS) was found to be the lowest with the average microhardness of 316.63 $HV_{0.5}$.

The average microhardness of the aged specimen (PH) was recorded as 527.67 $HV_{0.5}$ which is the highest measured hardness in the current experiments. In the aging heat treatment, both α and β phases tended to coarsen simultaneously but hindered each other's growth. This phenomenon led to compact microstructure resulted in increase in microhardness. Yan *et al.* [13], after heat treating SLM Ti-6Al-4V alloy at 800^0C, 900^0C, and 1080^0C, found Vickers microhardness of 367 $HV_{0.2}$, 344 $HV_{0.2}$, and 421 $HV_{0.2}$ respectively, which are in good agreement with the results obtained in this study. Furthermore, this variation in hardness is confirmed by the nanoindentation investigation of the as-printed and heat treated samples.
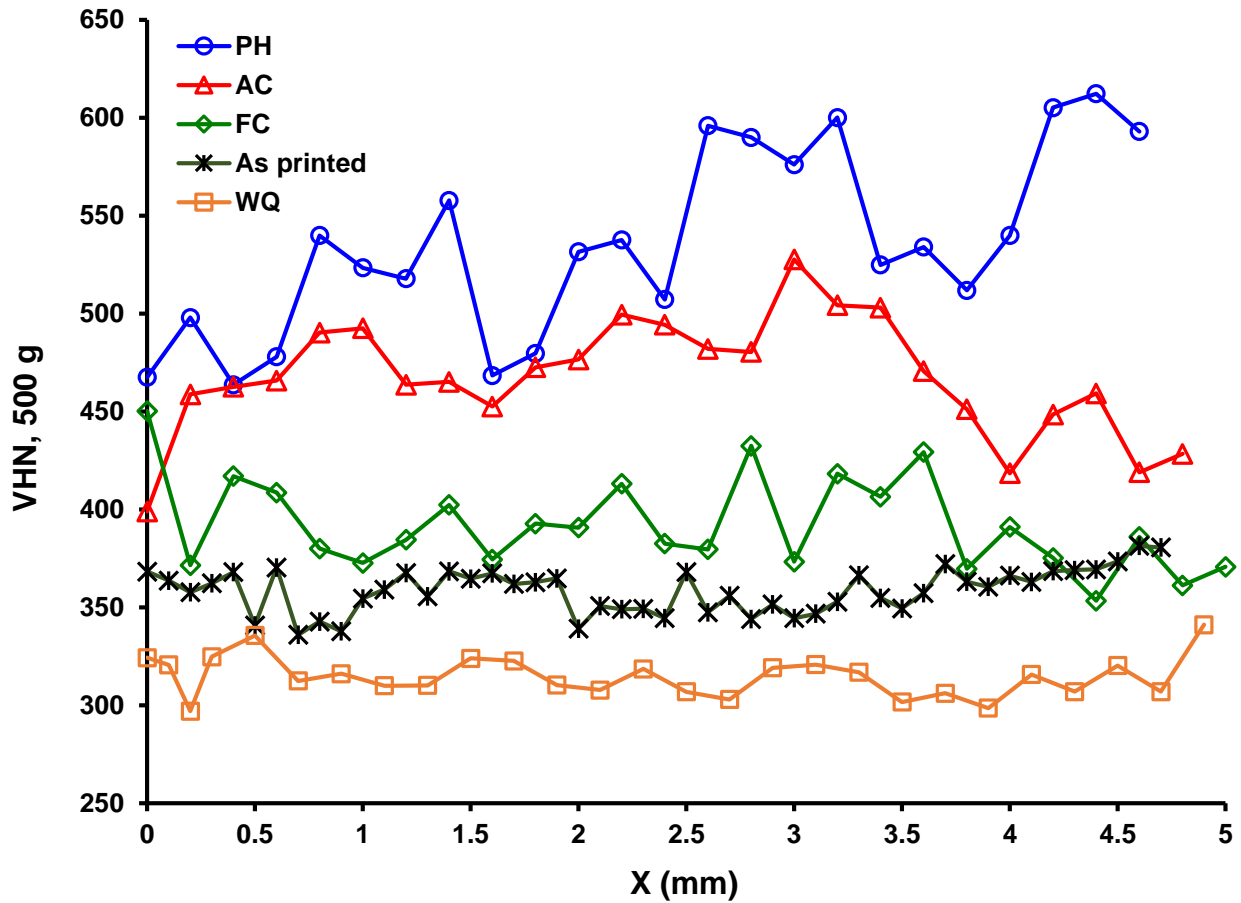
Fig. 4.15: Vickers microhardness of L-PBF Ti-6Al-4V alloy following as received sample and various heat treatments

4.2.3. Indentation responses

The load/ displacement (*P-h*) curves with a loading rate of 2 mN/s and holding time of 5 s for as-printed and heat treated samples at peak load of 10 mN are shown in Fig. 4.16. Load plateaus are observed at constant load holding stage and its instantaneous displacement variation with different types of heat treatment. Indenter displacements within the specimen, *h*, for the aged, air cooled, furnace cooled, as received, and water quenched samples are 120.87 nm, 148.02 nm, 189.18 nm, 222.89 nm, and 255.51 nm, respectively. The aged samples showed least indentation depth, consisting highest hardness of all the heat treated samples. The aged heat treated consisted of most compact α growth along the epitaxial way, resulting in less penetration of the indenter during penetration. The indentation depth is followed by air cooled, furnace cooled, and water quenched samples. The compact connected semi-equiaxed formation of α and martensitic $\acute{\alpha}$ in aged, air cooled, and furnace cooled sample is the reason behind their less

indentation penetration depth in compared with the as received sample. The less compact formation of α and $\acute{\alpha}$ in the water quenched sample due to incompatibility to complete full transformation during cooling along with presence of defects and entrapped gases led to large indentation penetration depths.
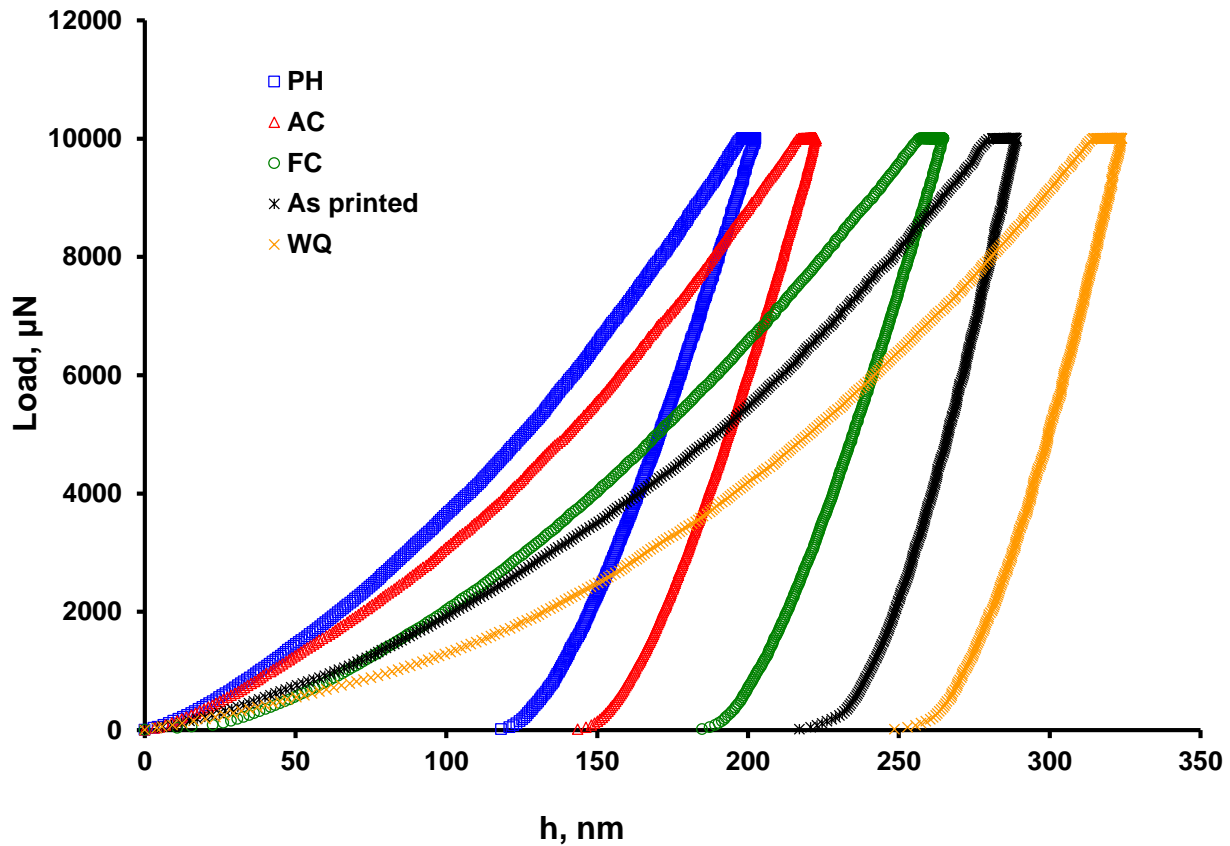
Fig. 4.16: *P-h* curves demonstrating indentation response of as received sample and various heat treated samples.

Plasticity index is defined as ratio of indentation hardness to reduced modulus of elasticity [189]. Reduced modulus of elasticity represents the elastic deformation that occurs in both sample and indenter tip. Fig. 4.17 shows the plasticity index of different heat treated samples. H and E_r is calculated using Eqs. (11) & (1) respectively. Considering the H/E_r measured through the nanoindentation, the WQ sample possesses the lowest value. The hardness and elastic modulus is directly related to the damage variable (*i.e.* defects volume fraction) which is assumed to be higher in the WQ specimen as compared with the other samples. This fact is further supported by the elastic recovery parameters (ERP) of the heat treated samples as shown in the Fig. 4.18. Fig. 4.18 shows the ERP of different heat treated samples using Eq. (12). ERP is a dimensionless index

which is closely related to the ratio between hardness and Young's modulus. ERP is lowest in the WQ sample confirming this as the softest microstructure.
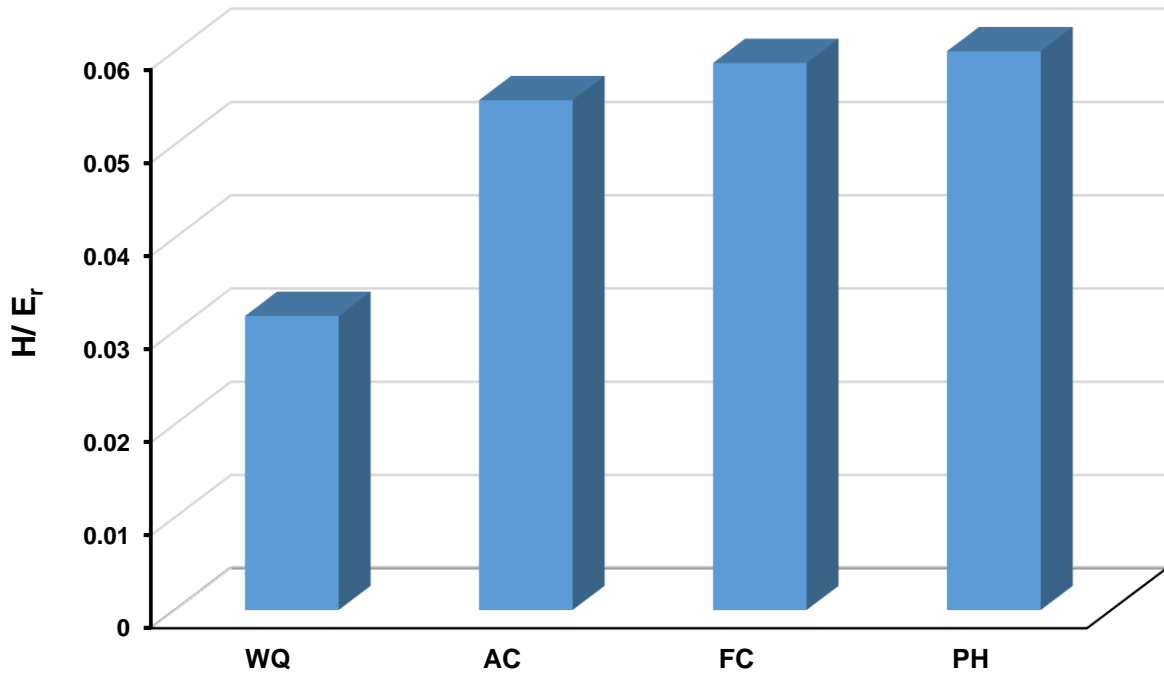
Fig. 4.17: Variation of plasticity index across different heat treated samples.
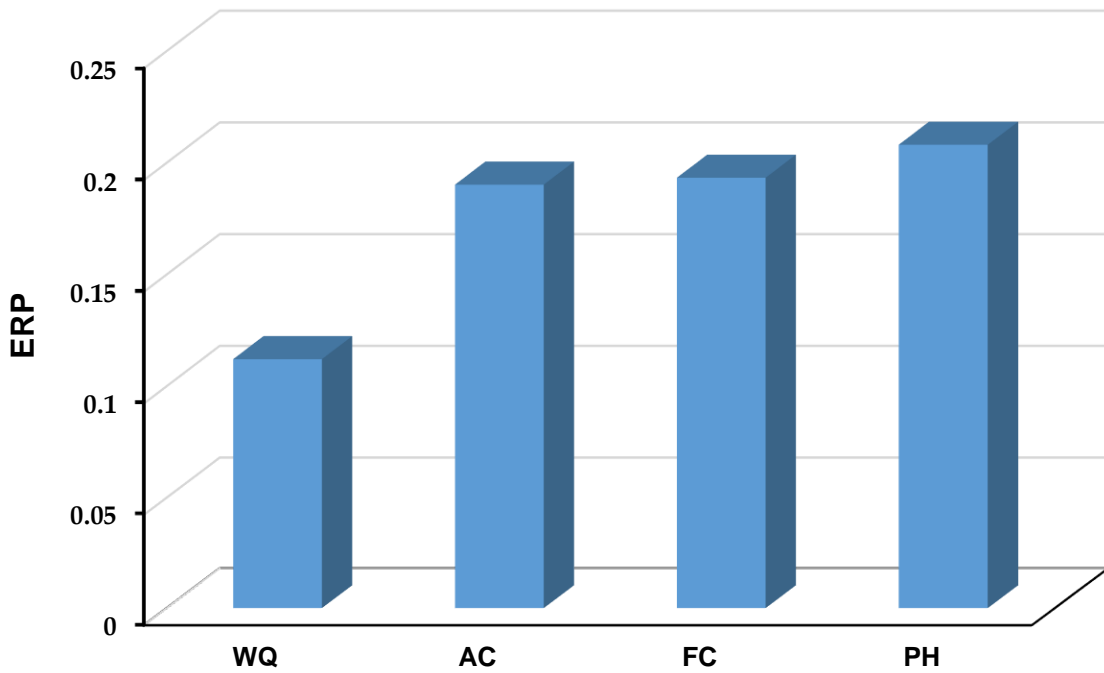
Fig. 4.18: Elastic recovery parameters (ERP) of the heat treated samples.

4.2.4. Indentation Size Effect (ISE)

Fig. 4.19 demonstrates the indentation stress *vs* indentation displacement curve. Indentation stress was calculated by using Eq. (7). Strong indentation size effects are observed for the additively manufactured Ti-6Al-4V alloy in as-printed and heat treated conditions. From Fig. 4.19, it is observed that all the heat treated samples experience a sharp decline of the indentation stress in shallower depth, which almost become constant at deeper depth, demonstrating a strong size effect for the heat treated samples. All the four heat treated samples exhibited more size effects in compared to the as-printed sample. As shown in the micrographs of the heat treated samples, the aged heat treated sample contains most compact growth of α, resulting in experiencing highest indentation stress of all the samples, followed by air cooled, furnace cooled, as received, and water quenched sample.
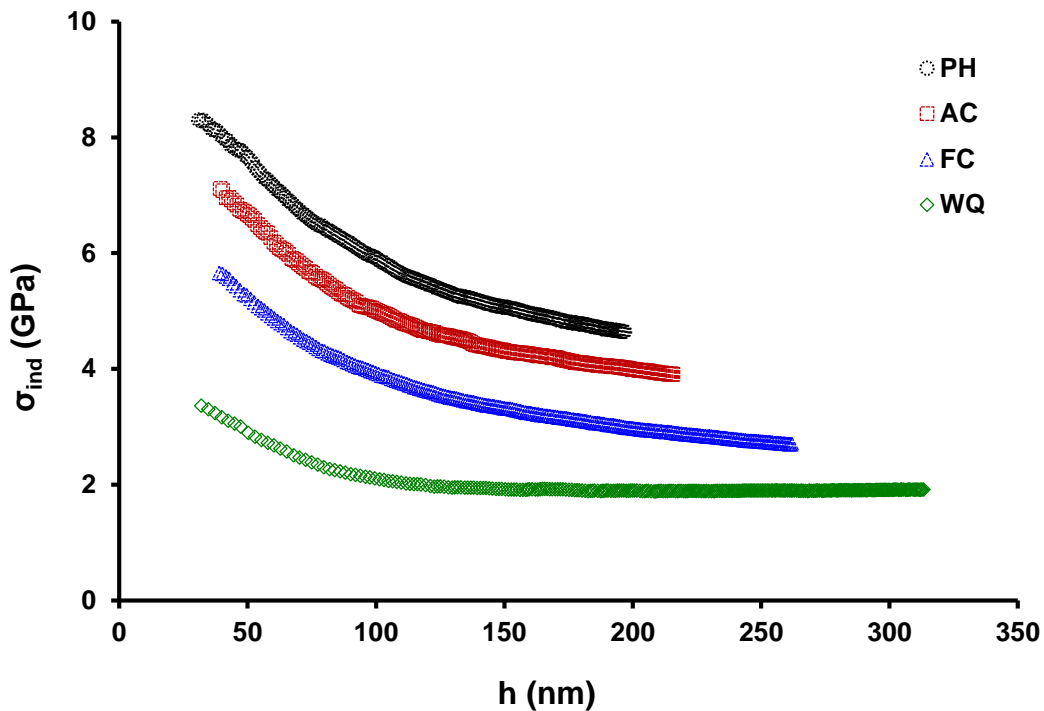
Fig. 4.19: Indentation size effect of as received and heat treated samples.

In order to further assess indentation size effect according to the Nix-Gao model [190], H_{ind} was calculated using Eq. (11) and was plotted against $1/h$ as shown in Fig. 4.20 for different heat treated sample. Since Nix-Gao model is not reliable at depth shallower than 100 nm [190], hardness at shallower indentation depth was ignored here. Hardness at

depth greater 100 nm showed depth dependency *i.e.* all the heat treated samples experienced indentation size effects.
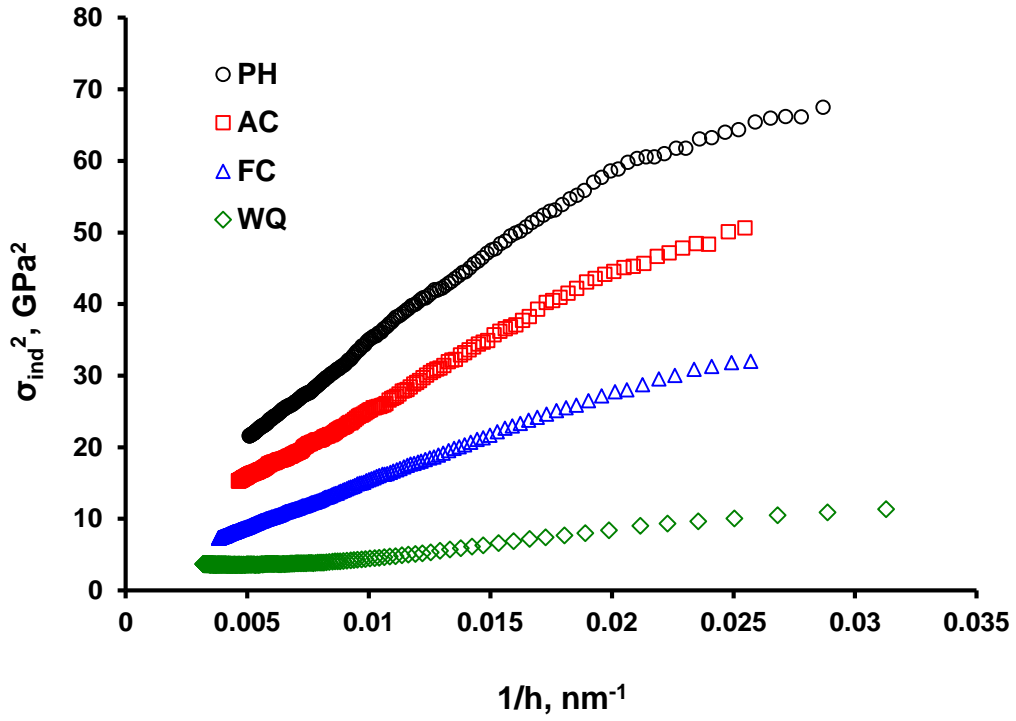
Fig. 4.20: Indentation size effect measured for different heat treated samples.

Chapter V

5. Conclusions and Future Work

The goal of this research was to assess ambient temperature depth-sensing indentation creep behavior of an additive manufactured Ti-6Al-4V alloy at different scan sizes and scan directions and to examine the effect of various cooling rates on the microstructure and micromechanical properties of a Ti-6Al-4V alloy, processed via laser powder bed fusion (L-PBF) technique. The depth-sensing (instrumented) indentation testing technique (*i.e.* micro/ nano-indentation), a reliable, convenient, and non-destructive testing technique, was applied to examine the microstructure/ mechanical property correlation. To evaluate microstructure/ processing parameter/ property correlations in the additive manufacture Ti-6Al-4V alloy, microstructural quantitative analyses (*i.e.* optical microscopy and scanning electron microscopy) were performed as well.

5.1. Ambient temperature creep of AM Ti-6Al-4V alloy

- Some sink-in effects are observed on the indented area where the flat sides of the impression deformed inward around the indentation.
- Creep parameters (creep rate and creep stress exponent) are dependent upon indentation load and dwelling time during constant-load holding stage.
- Tri-axial non-homogeneous stress state and a continually growing deformation volume underneath the indenter causes creep of Ti-6Al-4V materials at ambient temperature.
- Dislocation movement (*i.e.* power-law creep) dominates the secondary stage of indentation creep in the printed Ti-6Al-4V materials at ambient (room) temperature.
- Indentation creep curves experienced an initial sharp rise at the primary or transient creep stage and then the creep increases almost linearly at steady-state stage just like conventional uniaxial creep.
- A clear indentation size effect (ISE) response primarily attributed to the Geometrically Necessary Dislocations (GNDs) was found in the indentation stress versus indentation depth graphs.
- Vertically scanned samples experienced slightly more creep rate in comparison to their horizontally scanned counter parts.

- Indentation depth was slightly higher in horizontally scanned samples in compared to their counter parts indicating they have experienced slightly more creep.

5.2. Effect of various cooling methods after heat treatment of AM Ti-6Al-4V alloy

- After cooling the samples followed by solutionizing treatment at 950°C, primary α became significantly coarser, slender, and shorter, connected with each other to form compact structure.

- The WQ sample is the softest one as this sample is solutionized and then water quenched and upon quenching, the Super Saturated Solid Solution (SSSS) which is in an un-equilibrium state is formed.

- The intermetallic Ti$_3$Al precipitates disappeared from the microstructure of samples during solutionizing but reappear after air cooling and furnace cooling.

- In the precipitation hardened samples, both the α and β tended to coarsen simultaneously however hindered each other's growth. This results in the formation of compact microstructure consisting of highest micro-hardness of all the heat treated samples, followed by air cooled and furnace cooled samples.

- Due to high cooling rate in the WQ sample, lack of sufficient time available for the microstructural transformations results in large density of entrapped gases, defects, voids, and porosities which adversely affect the strength of the material.

- A clear Indentation Size Effect (ISE) response primarily attributed to the GNDs was observed in the indentation stress versus indentation depth graphs in heat treated samples.

5.3. Future work

The following future works are recommended to assess the ambient temperature creep and effect of various cooling methods for L-PBF fabricated Ti-6Al-4V alloy:

- Depth-sensing creep of conventionally manufactured Ti-6Al-4V alloy should be measured and compared against the obtained values in the present thesis.

- Instrumented creep of Ti-6Al-4V parts produced by other types of additive manufacturing should be assessed to reconfirm and establish depth sensing indentation as a regular approach to study creep of materials.

- Elevated temperature creep of AM Ti-6Al-4V can be performed to have a comprehensive understanding of the time-dependent plastic deformation of the material both at ambient and elevated temperature conditions.
- AM Ti-6Al-4V with different build parameters and orientations can be assessed to better understand the effect of print parameter on the response of the material.
- Microstructures of heat treated samples should be analyzed by X-ray diffraction (XRD) or Electron backscatter diffraction (EBSD) to properly investigate the formation of precipitations.
- Heat treatments of L-PBF Ti-6Al-4V with different print parameters and build conditions can be investigated.
- Micro/ nano- indentions can be employed to assess other types of micro-mechanical properties including residual stress measurements.
- Mathematical models can be developed to predict creep behavior and heat treatment response of the additive manufactured Ti-6Al-4V alloy.

Appendix

5.4. Equations used for calculating instrumented indentation parameters:

$$\frac{1}{E_r} = \frac{(1-v^2)}{E} + \frac{(1-v_i^2)}{E_i}$$

(1)

$$S = \frac{dP}{dh} = \frac{2}{\sqrt{\pi}} E_r \sqrt{A}$$

(2)

$$H = \frac{P_{max}}{A}$$

(3)

$$H = C_1 \sigma$$

(4)

$$\dot{\varepsilon}_u = C_2 \dot{\varepsilon}_\iota$$

(5)

$$\dot{\varepsilon}_{ind} = \frac{\dot{h}}{h} = \frac{1}{2} \frac{\dot{P}}{P}$$

(6)

$$\sigma_{ind} = \frac{P}{24.56 \times (h + 0.06R)^2}$$

(7)

$$\dot{\varepsilon}_{ind} = \frac{AD_0 Gb}{kT} \left(\frac{b}{d}\right)^p \left(\frac{\sigma_{ind}}{G}\right)^n \exp\left(\frac{\Delta Q}{kT}\right)$$

(8)

$$\dot{\varepsilon}_{ind} = B\sigma_{ind}^n$$

(9)

$$n = \frac{\partial \ln \dot{\varepsilon}_{ind}}{\partial \ln \sigma_{ind}}$$

(10)

$$H_{ind} = \frac{P_{ind}}{A(h_c)}$$

(11)

$$ERP = \frac{h_{max} - h_c}{h_{max}}$$

(12)

References

[1] D. M. Marsh, "Plastic Flow in Glass," *Proc. R. Soc. A Math. Phys. Eng. Sci.*, 1964.

[2] K. L. Johnson, "The correlation of indentation experiments," *J. Mech. Phys. Solids*, 1970.

[3] K.-H. Kim and Y.-C. Jeong, "Nanoindentation study of optically patterned surface relief grating of azobenzene polymers," *Opt. Express*, 2016.

[4] M. Es-Souni, "Creep behaviour and creep microstructures of a high-temperature titanium alloy Ti-5.8Al-4.0Sn-3.5Zr-0.7Nb-0.35Si-0.06C (Timetal 834): Part I. Primary and steady-state creep," *Mater. Charact.*, 2001.

[5] W. Ziaja, M. Motyka, K. Kubiak, and J. Sieniawski, "Primary creep behaviour of two-phase titanium alloy with various microstructure," *Arch. Metall. Mater.*, 2016.

[6] L. Badea, M. Surand, J. Ruau, and B. Viguier, "CREEP BEHAVIOR OF Ti-6Al-4V FROM 450 ° C TO 600 ° C," *U.P.B. Sci. Bull.*, 2014.

[7] T. Kameyama, T. Matsunaga, E. Sato, and K. Kuribayashi, "Suppression of ambient-temperature creep in CP-Ti by cold-rolling," *Mater. Sci. Eng. A*, 2009.

[8] P. Kral, J. Dvorak, S. Zherebtsov, G. Salishchev, M. Kvapilova, and V. Sklenicka, "Effect of severe plastic deformation on creep behaviour of a Ti-6Al-4V alloy," in *Journal of Materials Science*, 2013.

[9] B. D. Venkatesh, D. L. Chen, and S. D. Bhole, "Effect of heat treatment on mechanical properties of Ti-6Al-4V ELI alloy," *Mater. Sci. Eng. A*, 2009.

[10] B. Vrancken, L. Thijs, J.-P. Kruth, and J. Van Humbeeck, "Heat treatment of Ti6Al4V produced by Selective Laser Melting: Microstructure and mechanical properties," *J. Alloys Compd.*, 2012.

[11] Z. Fan and H. Feng, "Study on selective laser melting and heat treatment of Ti-6Al-4V alloy," *Results Phys.*, 2018.

[12] S. M. Ahmadi, R. K. Ashok Kumar Jain, A. A. Zadpoor, C. Ayas, and V. A. Popovich, "Effects of heat treatment on microstructure and mechanical behaviour of additive manufactured porous Ti6Al4V," *IOP Conf. Ser. Mater. Sci. Eng.*, 2018.

[13] X. Yan, S. Yin, C. Chen, C. Huang, R. Bolot, R. Lupoi, M. Kuang, W. Ma, C. Coddet, H. Liao, and M. Liu, "Effect of heat treatment on the phase transformation and mechanical properties of Ti6Al4V fabricated by selective laser melting," in Journal of Alloys and Compounds, 2018.

[14]   H. Galarraga, R. J. Warren, D. A. Lados, R. R. Dehoff, M. M. Kirka, and P. Nandwana, "Effects of heat treatments on microstructure and properties of Ti-6Al-4V ELI alloy fabricated by electron beam melting (EBM)," *Mater. Sci. Eng. A*, 2017.

[15]   C. Leyens and M. Peters, *Titanium an Titanium Alloys*. 2003.

[16]   B. V. Krishna, W. Xue, S. Bose, and A. Bandyopadhyay, "Engineered porous metals for implants," *JOM*. 2008.

[17]   I. H. Oh, N. Nomura, N. Masahashi, and S. Hanada, "Mechanical properties of porous titanium compacts prepared by powder sintering," *Scr. Mater.*, vol. 49, no. 12, pp. 1197–1202, 2003.

[18]   M. Niinomi, "Mechanical biocompatibilities of titanium alloys for biomedical applications," *Journal of the Mechanical Behavior of Biomedical Materials*, vol. 1, no. 1. pp. 30–42, 2008.

[19]   AZoM, "Titanium Alloys - Ti6Al4V Grade 5," *AZO Materials*, 2002. .

[20]   S. Bremen, W. Meiners, and A. Diatlov, "Selective Laser Melting. A manufacturing technology for the future?," *Laser Tech. J.*, vol. 9, pp. 33–38, 2012.

[21]   R. Filip, K. Kubiak, W. Ziaja, and J. Sieniawski, "The effect of microstructure on the mechanical properties of two-phase titanium alloys," in *Journal of Materials Processing Technology*, 2003, vol. 133, no. 1–2, pp. 84–89.

[22]   L. Ladani, "Local and Global Mechanical Behavior and Microstructure of Ti6Al4V Parts Built Using Electron Beam Melting Technology," *Metall. Mater. Trans. A Phys. Metall. Mater. Sci.*, vol. 46, no. 9, pp. 3835–3841, 2015.

[23]   X. Ma *et al.*, "Indenter load effects on creep deformation behavior for Ti-10V-2Fe-3Al alloy at room temperature," *J. Alloys Compd.*, 2017.

[24]   J. Kumar, S. G. S. Raman, and V. Kumar, "Creep–Fatigue Interactions in Ti-6Al-4V Alloy at Ambient Temperature," *Trans. Indian Inst. Met.*, 2016.

[25]   T. Matsunaga, T. Kameyama, K. Takahashi, and E. Sato, "Intragranular Deformation Mechanisms during Ambient-Temperature Creep in Hexagonal Close-Packed Metals," *Mater. Trans.*, 2009.

[26]   V. Hasija, S. Ghosh, M. J. Mills, and D. S. Joseph, "Deformation and creep modeling in polycrystalline Ti-6Al alloys," *Acta Mater.*, 2003.

[27]   M. J. R. Barboza *et al.*, "Creep behavior of Ti-6Al-4V and a comparison with titanium matrix composites," *Mater. Sci. Eng. A*, 2006.

[28]   E. Sato, T. Yamada, H. Tanaka, and I. Jimbo, "Categorization of ambient temperature creep behavior of metals and alloys on their crystallographic structures," *J. Japan Inst. Light Met.*, 2005.

[29]   W. J. Harrison, M. T. Whittaker, and R. J. Lancaster, "A model for time dependent strain accumulation and damage at low temperatures in Ti-6Al-4V," *Mater. Sci. Eng. A*, 2013.

[30]   W. J. Evans, "Time dependent effects in fatigue of titanium and nickel alloys," *Fatigue Fract. Eng. Mater. Struct.*, 2004.

[31]   H. Tanaka, T. Yamada, E. Sato, and I. Jimbo, "Distinguishing the ambient-temperature creep region in a deformation mechanism map of annealed CP-Ti," *Scr. Mater.*, 2006.

[32]   T. Neeraj, D. H. Hou, G. S. Daehn, and M. J. Mills, "Phenomenological and microstructural analysis of room temperature creep in titanium alloys," *Acta Mater.*, 2000.

[33]   N. Dai, J. Zhang, Y. Chen, and L.-C. Zhang, "Heat Treatment Degrading the Corrosion Resistance of Selective Laser Melted Ti-6Al-4V Alloy," *J. Electrochem. Soc.*, vol. 164, no. 7, pp. C428–C434, 2017.

[34]   N. Dai, J. Zhang, Y. Chen, and L.-C. Zhang, "Heat Treatment Degrading the Corrosion Resistance of Selective Laser Melted Ti-6Al-4V Alloy," *J. Electrochem. Soc.*, vol. 164, no. 7, 2017.

[35]   Q. Huang, X. Liu, X. Yang, R. Zhang, Z. Shen, and Q. Feng, "Specific heat treatment of selective laser melted Ti–6Al–4V for biomedical applications," *Front. Mater. Sci.*, vol. 9, no. 4, pp. 373–381, 2015.

[36]   L. Facchini, E. Magalini, P. Robotti, A. Molinari, S. Höges, and K. Wissenbach, "Ductility of a Ti-6Al-4V alloy produced by selective laser melting of prealloyed powders," *Rapid Prototyp. J.*, 2010.

[37]   T. Sercombe, N. Jones, R. Day, and A. Kop, "Heat treatment of Ti-6Al-7Nb components produced by selective laser melting," *Rapid Prototyp. J.*, 2008.

[38]   T. Vilaro, C. Colin, and J. D. Bartout, "As-fabricated and heat-treated microstructures of the Ti-6Al-4V alloy processed by selective laser melting," *Metall. Mater. Trans. A Phys. Metall. Mater. Sci.*, 2011.

[39]   C. Leyens and M. Peters, *Titanium and Titanium Alloys*. 2003.

[40]   B. V. Krishna, W. Xue, S. Bose, and A. Bandyopadhyay, "Engineered porous metals for implants," *JOM*, vol. 60, no. 5. pp. 45–48, 2008.

[41]   G. Z. Chen, D. J. Fray, and T. W. Farthing, "Direct electrochemical reduction of titanium dioxide to titanium in molten calcium chloride," *Nature*, vol. 407, no. 6802, pp. 361–364, 2000.

[42]   R. R. Boyer, "An overview on the use of titanium in the aerospace industry," *Materials Science and Engineering A*, vol. 213, no. 1–2. pp. 103–114, 1996.

[43]   R. T. Cole, E. J. Bateh, and J. Potter, "Fasteners for composite structures," *Composites*, vol. 13, no. 3, pp. 233–240, 1982.

[44]   I. P. Polmear, "Light Alloys - From Traditional Alloys to Nanocrystals," *Light Alloy.*, vol. 2, pp. 273–277, 2006.

[45]   G. Lütjering and J. C. Williams, "Special Properties and Applications of Titanium," in *Titanium*, 2007, pp. 383–415.

[46]   E. A. Bel'skaya and E. Y. Kulyamina, "Electrical resistivity of titanium in the temperature range from 290 to 1800 K," *High Temp.*, vol. 45, no. 6, pp. 785–796, 2007.

[47]   S. S. Al-Bermani, M. L. Blackmore, W. Zhang, and I. Todd, "The origin of microstructural diversity, texture, and mechanical properties in electron beam melted Ti-6Al-4V," *Metall. Mater. Trans. A Phys. Metall. Mater. Sci.*, vol. 41, no. 13, pp. 3422–3434, 2010.

[48]   F. Campbell, "Elements of metallurgy and engineering alloys," *ASM Int.*, vol. #05224G, p. 672, 2008.

[49]   W. G. Burgers, "On the process of transition of the cubic-body-centered modification into the hexagonal-close-packed modification of zirconium," *Physica*, vol. 1, no. 7–12, pp. 561–586, 1934.

[50]   T. Karthikeyan, S. Saroja, and M. Vijayalakshmi, "Evaluation of misorientation angle-axis set between variants during transformation of bcc to hcp phase obeying Burgers orientation relation," *Scr. Mater.*, vol. 55, no. 9, pp. 771–774, 2006.

[51]   M. R. Daymond, R. A. Holt, S. Cai, P. Mosbrucker, and S. C. Vogel, "Texture inheritance and variant selection through an hcp-bcc-hcp phase transformation," *Acta Mater.*, vol. 58, no. 11, pp. 4053–4066, 2010.

[52]   N. Gey, M. Humbert, M. J. Philippe, and Y. Combres, "Investigation of the α- and β- texture evolution of hot rolled Ti-64 products," *Mater. Sci. Eng. A*, vol. 219, no. 1–2, pp. 80–88, 1996.

[53]   G. C. Obasi, S. Birosca, J. Quinta da Fonseca, and M. Preuss, "Effect of β Grain Growth on Variant Selection and Texture Memory Effect during $\alpha \rightarrow \beta \rightarrow \alpha$ Phase

Transformation in Ti–6Al–4V," *Acta Mater.*, vol. 60, pp. 1048–1058, 2012.

[54]   R. Shi and Y. Wang, "Variant selection during α precipitation in Ti-6Al-4V under the influence of local stress - A simulation study," *Acta Mater.*, vol. 61, no. 16, pp. 6006–6024, 2013.

[55]   ASTM International, "Standard Specification for Titanium-6Aluminum-4Vanadium Alloy Castings for Surgical Implants (UNS R56406)," *Astm F1108-04*, vol. 04, no. Reapproved 2009, pp. 1–4, 2010.

[56]   C. Loier, G. Thauvin, A. Hazotte, and A. Simon, "Influence of deformation on the β→α+β transformation kinetics of Ti-6wt.%Al-4wt.%V alloy," *J. Less-Common Met.*, vol. 108, no. 2, pp. 295–312, 1985.

[57]   I. Polmear, *Light Alloys [Fourth edition]*, vol. 2. 1981.

[58]   F. Wang, S. Williams, P. Colegrove, and A. A. Antonysamy, "Microstructure and mechanical properties of wire and arc additive manufactured Ti-6Al-4V," *Metall. Mater. Trans. A Phys. Metall. Mater. Sci.*, vol. 44, no. 2, 2013.

[59]   M. Simonelli, Y. Y. Tse, and C. Tuck, "On the texture formation of selective laser melted Ti-6Al-4V," *Metall. Mater. Trans. A Phys. Metall. Mater. Sci.*, vol. 45, no. 6, pp. 2863–2872, 2014.

[60]   T. Furuhara, B. Poorganji, H. Abe, and T. Maki, "Dynamic recovery and recrystallization in titanium alloys by hot deformation," *JOM*, vol. 59, no. 1, pp. 64–67, 2007.

[61]   R. Ding and Z. X. Guo, "Microstructural evolution of a Ti-6Al-4V alloy during β-phase processing: Experimental and simulative investigations," *Mater. Sci. Eng. A*, vol. 365, no. 1–2, pp. 172–179, 2004.

[62]   P. Honarmandi and M. Aghaie-Khafri, "Hot Deformation Behavior of Ti–6Al–4V Alloy in β Phase Field and Low Strain Rate," *Metallogr. Microstruct. Anal.*, vol. 2, no. 1, pp. 13–20, 2012.

[63]   A. Pilchak and A. Bhattacharjee, "The Effect of Microstructure on Fatigue Crack Initiation in Ti-6Al-4V," *ICF12, Ottawa 2012*, vol. 2, pp. 1–10, 2013.

[64]   K. Muszka, M. Lopez-Pedrosa, K. Raszka, M. Thomas, W. M. Rainforth, and B. P. Wynne, "The Impact of Strain Reversal on Microstructure Evolution and Orientation Relationships in Ti-6Al-4V with an Initial Alpha Colony Microstructure," *Metall. Mater. Trans. A Phys. Metall. Mater. Sci.*, vol. 45, no. 13, pp. 5997–6007, 2014.

[65]   S. . Semiatin, V. Seetharaman, and I. Weiss, "Flow behavior and globularization

kinetics during hot working of Ti–6Al–4V with a colony alpha microstructure," *Mater. Sci. Eng. A*, vol. 263, no. 2, pp. 257–271, 1999.

[66] I. Weiss, F. H. Froes, D. Eylon, and G. E. Welsch, "Modification of alpha morphology in Ti-6Al-4V by thermomechanical processing," *Metall. Trans. A*, vol. 17, no. 11, pp. 1935–1947, 1986.

[67] R. K. Nalla, B. L. Boyce, J. P. Campbell, J. O. Peters, and R. O. Ritchie, "Influence of microstructure on high-cycle fatigue of Ti-6Al-4V: Bimodal vs. lamellar structures," in *Metallurgical and Materials Transactions A: Physical Metallurgy and Materials Science*, 2002, vol. 33, no. 3, pp. 899–918.

[68] H. K. Rafi, N. V. Karthik, H. Gong, T. L. Starr, and B. E. Stucker, "Microstructures and mechanical properties of Ti6Al4V parts fabricated by selective laser melting and electron beam melting," *J. Mater. Eng. Perform.*, vol. 22, no. 12, pp. 3872–3883, 2013.

[69] F. J. Humphreys and M. Hatherly, "Recrystallization and related annealing phenomenon," *Elsevier*, p. 710, 2004.

[70] S. Zaefferer, "A study of active deformation systems in titanium alloys: Dependence on alloy composition and correlation with deformation texture," *Mater. Sci. Eng. A*, vol. 344, no. 1–2, pp. 20–30, 2003.

[71] G. G. Yapici, I. Karaman, and Z. P. Luo, "Mechanical twinning and texture evolution in severely deformed Ti-6Al-4V at high temperatures," *Acta Mater.*, vol. 54, no. 14, pp. 3755–3771, 2006.

[72] R. J. McCabe, E. K. Cerreta, A. Misra, G. C. Kaschner, and C. N. Tomé, "Effects of texture, temperature and strain on the deformation modes of zirconium," *Philos. Mag.*, vol. 86, no. 23, pp. 3595–3611, 2006.

[73] S. L. Semiatin and T. R. Bieler, "Effect of texture changes on flow softening during hot working of Ti-6Al-4V," *Metall. Mater. Trans. A Phys. Metall. Mater. Sci.*, vol. 32, no. 7, p. 1871, 2001.

[74] D. G. L. Prakash *et al.*, "Deformation twinning in Ti-6Al-4V during low strain rate deformation to moderate strains at room temperature," *Mater. Sci. Eng. A*, vol. 527, no. 21–22, pp. 5734–5744, 2010.

[75] I. Karaman, G. G. Yapici, Y. I. Chumlyakov, and I. V. Kireeva, "Deformation twinning in difficult-to-work alloys during severe plastic deformation," *Mater. Sci. Eng. A*, vol. 410–411, pp. 243–247, 2005.

[76] J. Donoghue, "Hybrid Additive Manufacture and Deformation Processing for

Large Scale Near-Net Shape Manufacture of Titanium Aerospace Components," *Thesis*, p. 201, 2016.

[77]   M. Matsuda, S. Ii, Y. Kawamura, Y. Ikuhara, and M. Nishida, "Interaction between long period stacking order phase and deformation twin in rapidly solidified Mg97Zn1Y2alloy," *Mater. Sci. Eng. A*, vol. 386, no. 1–2, pp. 447–452, 2004.

[78]   L. Bian, S. M. Thompson, and N. Shamsaei, "Mechanical Properties and Microstructural Features of Direct Laser-Deposited Ti-6Al-4V," *JOM*. 2015.

[79]   M. Masoomi, J. W. Pegues, S. M. Thompson, and N. Shamsaei, "A numerical and experimental investigation of convective heat transfer during laser-powder bed fusion," *Addit. Manuf.*, vol. 22, 2018.

[80]   S. Ly, A. M. Rubenchik, S. A. Khairallah, G. Guss, and M. J. Matthews, "Metal vapor micro-jet controls material redistribution in laser powder bed fusion additive manufacturing," *Sci. Rep.*, 2017.

[81]   H. Wang, Y. Shi, S. Gong, and A. Duan, "Effect of assist gas flow on the gas shielding during laser deep penetration welding," *J. Mater. Process. Technol.*, vol. 184, no. 1–3, pp. 379–385, 2007.

[82]   A. M. Philo *et al.*, "A Study Into the Effects of Gas Flow Inlet Design of the Renishaw Am250 Laser Powder Bed Fusion Machine Using Computational Modelling," *Solid Free. Fabr. Symp.*, 2017.

[83]   P. Kah and J. Martikainen, "Influence of shielding gases in the welding of metals," *Int. J. Adv. Manuf. Technol.*, vol. 64, no. 9–12, pp. 1411–1421, 2013.

[84]   Y. Li and D. Gu, "Parametric analysis of thermal behavior during selective laser melting additive manufacturing of aluminum alloy powder," *Mater. Des.*, 2014.

[85]   D. Riedlbauer, M. Drexler, D. Drummer, P. Steinmann, and J. Mergheim, "Modelling, simulation and experimental validation of heat transfer in selective laser melting of the polymeric material PA12," *Comput. Mater. Sci.*, 2014.

[86]   P. Michaleris, "Modeling metal deposition in heat transfer analyses of additive manufacturing processes," *Finite Elem. Anal. Des.*, 2014.

[87]   Y. Li and D. Gu, "Thermal behavior during selective laser melting of commercially pure titanium powder: Numerical simulation and experimental study," *Addit. Manuf.*, 2014.

[88]   S. A. Khairallah, A. T. Anderson, A. Rubenchik, and W. E. King, "Laser powder-bed fusion additive manufacturing: Physics of complex melt flow and formation

mechanisms of pores, spatter, and denudation zones," *Acta Mater.*, 2016.

[89] H.-W. Mindt, M. Megahed, N. P. Lavery, A. Giordimaina, and S. G. R. Brown, "Verification of Numerically Calculated Cooling Rates of Powder Bed Additive Manufacturing," in *TMS 2016: 145th Annual Meeting & Exhibition: Supplemental Proceedings*, 2016.

[90] P. A. Kobryn and S. L. Semiatin, "The laser additive manufacture of Ti-6Al-4V," *JOM*, vol. 53, no. 9, pp. 40–42, 2001.

[91] A. A. Antonysamy, P. B. Prangnell, and J. Meyer, "Effect of Wall Thickness Transitions on Texture and Grain Structure in Additive Layer Manufacture (ALM) of Ti-6Al-4V," *Mater. Sci. Forum*, vol. 706–709, pp. 205–210, 2012.

[92] P. Edwards, A. O'Conner, and M. Ramulu, "Electron Beam Additive Manufacturing of Titanium Components: Properties and Performance," *J. Manuf. Sci. Eng.*, vol. 135, no. 6, p. 061016, 2013.

[93] B. Baufeld, O. Van Der Biest, and R. Gault, "Additive manufacturing of Ti – 6Al – 4V components by shaped metal deposition : Microstructure and mechanical properties," *Mater. Des.*, vol. 31, pp. 106–111, 2010.

[94] M. Simonelli, Y. Y. Tse, and C. Tuck, "On the texture formation of selective laser melted Ti-6Al-4V," *Metall. Mater. Trans. A Phys. Metall. Mater. Sci.*, vol. 45, no. 6, pp. 2863–2872, 2014.

[95] F. Wang, S. Williams, P. Colegrove, and A. A. Antonysamy, "Microstructure and mechanical properties of wire and arc additive manufactured Ti-6Al-4V," *Metall. Mater. Trans. A Phys. Metall. Mater. Sci.*, vol. 44, no. 2, pp. 968–977, 2013.

[96] M. Rappaz, S. A. David, J. M. Vitek, and L. A. Boatner, "Analysis of solidification microstructures in Fe-Ni-Cr single-crystal welds," *Metall. Trans. A*, vol. 21, no. 6, pp. 1767–1782, 1990.

[97] F. Martina, P. A. Colegrove, S. W. Williams, and J. Meyer, "Microstructure of Interpass Rolled Wire + Arc Additive Manufacturing Ti-6Al-4V Components," *Metall. Mater. Trans. A Phys. Metall. Mater. Sci.*, vol. 46, no. 12, pp. 6103–6118, 2015.

[98] J. B. Pethicai, R. Hutchings, and W. C. Oliver, "Hardness measurement at penetration depths as small as 20 nm," *Philos. Mag. A Phys. Condens. Matter, Struct. Defects Mech. Prop.*, 1983.

[99] W. Oliver and G. Pharr, "An improved technique for determining hardness and elastic modulus using load and displacement-sensing indentation systems," *J. Mater. Res.*, 1992.

[100] J. L. Loubet, J. M. Georges, O. Marchesini, and G. Meille, "Vickers Indentation Curves of Magnesium Oxide (MgO)," *J. Tribol.*, 1984.

[101] M. F. Doerner and W. D. Nix, "A method for interpreting the data from depth-sensing indentation instruments," *J. Mater. Res.*, 1986.

[102] G. M. Pharr and W. C. Oliver, "Measurement of Thin Film Mechanical Properties Using Nanoindentation," *MRS Bull.*, 1992.

[103] WESTBROOK JH and JORGENSEN PJ, "EFFECTS OF WATER DESORPTION ON INDENTATION MICROHARDNESS ANISOTROPY IN MINERALS," *Am. Mineral.*, 1968.

[104] M. Boussinesq, "Loiasis," *Ann. Trop. Med. Parasitol.*, 2006.

[105] I. N. Sneddon, "Boussinesq's problem for a rigid cone," *Math. Proc. Cambridge Philos. Soc.*, 1948.

[106] H. Hertz, "Ueber die Verdunstung der Flüssigkeiten, insbesondere des Quecksilbers, im luftleeren Raume," *Ann. Phys.*, 1882.

[107] A. E. H. Love, "The Stress Produced in a Semi-Infinite Solid by Pressure on Part of the Boundary," *Philos. Trans. R. Soc. A Math. Phys. Eng. Sci.*, 1929.

[108] D. Tabor, "A Simple Theory of Static and Dynamic Hardness," *Proc. R. Soc. A Math. Phys. Eng. Sci.*, 1948.

[109] N. A. Stilwell and D. Tabor, "Elastic recovery of conical indentations," *Proc. Phys. Soc.*, 1961.

[110] A. P. Bulychev, S. I., Alekhin, V. P., Shorshorov, M. H., Ternovskii, "Determining Young's modulus from the indentor penetration diagram," *Ind. Lab.*, 1975.

[111] S. I. Bulychev, V. P. Alekhin, M. K. Shorshorov, and A. P. Ternovskii, "Mechanical properties of materials studied from kinetic diagrams of load versus depth of impression during microimpression," *Strength Mater.*, 1976.

[112] S. I. Bulychev and V. N. Malyshev, "DETERMINATION OF THE POROSITY CHARACTERISTICS ON THE BASIS OF THE KINETIC MICROHARDNESS TEST.," *Phys. Chem. Mater. Treat.*, 1986.

[113] G. M. Pharr, W. C. Oliver, and F. R. Brotzen, "On the generality of the relationship among cantact stiffness,contact area, and elastic-modulus during indentation," *J. Mater. Res.*, 1992.

[114] A. K. Bhattacharya and W. D. Nix, "Finite element analysis of cone indentation," *Int. J. Solids Struct.*, 1991.

[115] X. Liu, Q. Zhang, X. Zhao, X. Yang, and L. Luo, "Ambient-temperature nanoindentation creep in ultrafine-grained titanium processed by ECAP," *Mater. Sci. Eng. A*, 2016.

[116] Y. Ma, G. J. Peng, D. H. Wen, and T. H. Zhang, "Nanoindentation creep behavior in a CoCrFeCuNi high-entropy alloy film with two different structure states," *Mater. Sci. Eng. A*, 2015.

[117] T. R. G. Kutty, C. Ganguly, and D. H. Sastry, "Development of creep curves from hot indentation hardness data," *Scr. Mater.*, 1996.

[118] S. P. Hannula, D. Stone, and C. Y. Li, "Determination of time-dependent plastic properties of metals by indentation load relaxation techniques," *Mater. Res. Soc. Electron. Packag. Mater. Sci. Symp.*, 1985.

[119] W. R. LaFontaine, B. Yost, R. D. Black, and C. Y. Li, "Indentation Load Relaxation Experiments With Indentation Depth in The Submicron Range," *J. Mater. Res.*, 1990.

[120] M. J. Mayo and W. D. Nix, "A micro-indentation study of superplasticity in Pb, Sn, and Sn-38 wt% Pb," *Acta Metall.*, 1988.

[121] H. M. Pollock, D. Maugis, and M. Barquins, "Characterization of Submicrometre Surface Layers by Indentation," *Am. Soc. Test. Mater.*, 1986.

[122] M. J. Mayo, R. W. Siegel, A. Narayanasamy, and W. D. Nix, "Mechanical properties of nanophase TiO2 as determined by nanoindentation," *J. Mater. Res.*, 1990.

[123] B. N. Lucas and W. C. Oliver, "Indentation power-law creep of high-purity indium," *Metall. Mater. Trans. A*, vol. 30, no. March, pp. 601–610, 1999.

[124] P. K. Chu and L. Li, "Characterization of amorphous and nanocrystalline carbon films," *Mater. Chem. Phys.*, 2006.

[125] S. Gollapudi, D. V. V. Satyanarayana, C. Phaniraj, and T. K. Nandy, "Transient creep in titanium alloys: Effect of stress, temperature and trace element concentration," *Mater. Sci. Eng. A*, 2012.

[126] V. M. C. A. De Oliveira *et al.*, "Short-term creep properties of Ti-6Al-4V alloy subjected to surface plasma carburizing process," *J. Mater. Res. Technol.*, 2015.

[127] W. J. Evans and G. F. Harrison, "Power law steady state creep in ??/?? titanium alloys," *J. Mater. Sci.*, 1983.

[128] S. Bremen, W. Meiners, and A. Diatlov, "Selective Laser Melting. A

manufacturing technology for the future?," *Laser Tech. J.*, 2012.

[129] M. A. Imam and C. M. Gilmore, "Room temperature creep of Ti-6AI-4V," *Metall. Trans. A*, 1979.

[130] T. Seshacharyulu, S. C. Medeiros, J. T. Morgan, J. C. Malas, W. G. Frazier, and Y. V. R. K. Prasad, "Hot deformation and microstructural damage mechanisms in extra-low interstitial (ELI) grade Ti-6Al-4V," *Mater. Sci. Eng. A*, 2000.

[131] M. D. Naughton and P. Tiernan, "Mechanical behaviour and superplastic forming capabilities of extra-low interstitial grade Ti-6Al-4V wire alloy with numerical verification," *Proc. Inst. Mech. Eng. Part L J. Mater. Des. Appl.*, 2007.

[132] W. Zhang, B. Wu, W. S. Zhao, D. X. Li, and M. L. Sui, "Formation of novel β-Ti martensites in Ti-6Al-4V under an electric-current-pulse heat treatment," *Mater. Sci. Eng. A*, 2006.

[133] J. Donachie and J. M, "Titanium – A Technical Guide," *ASM Int. 2nd Ed.*, 2000.

[134] M. T. Jovanović, S. Tadić, S. Zec, Z. Mišković, and I. Bobić, "The effect of annealing temperatures and cooling rates on microstructure and mechanical properties of investment cast Ti-6Al-4V alloy," *Mater. Des.*, 2006.

[135] W. Callister and D. Rethwisch, *Materials science and engineering: an introduction*. 2007.

[136] L. E. Murr *et al.*, "Microstructure and mechanical behavior of Ti-6Al-4V produced by rapid-layer manufacturing, for biomedical applications," *Journal of the Mechanical Behavior of Biomedical Materials*. 2009.

[137] L. Thijs, F. Verhaeghe, T. Craeghs, J. Van Humbeeck, and J. P. Kruth, "A study of the microstructural evolution during selective laser melting of Ti-6Al-4V," *Acta Mater.*, 2010.

[138] T. Becker, M. Van Rooyen, and D. Dimitrov, "HEAT TREATMENT OF TI-6AL-4V PRODUCED BY LASERCUSING," *South African J. Ind. Eng.*, 2015.

[139] S. Ly, A. M. Rubenchik, S. A. Khairallah, G. Guss, and M. J. Matthews, "Metal vapor micro-jet controls material redistribution in laser powder bed fusion additive manufacturing," *Sci. Rep.*, vol. 7, no. 1, 2017.

[140] L. Facchini, E. Magalini, P. Robotti, and A. Molinari, "Microstructure and mechanical properties of Ti-6Al-4V produced by electron beam melting of pre-alloyed powders," *Rapid Prototyp. J.*, 2009.

[141] N. Hrabe and T. Quinn, "Effects of processing on microstructure and mechanical

properties of a titanium alloy (Ti-6Al-4V) fabricated using electron beam melting (EBM), Part 2: Energy input, orientation, and location," *Mater. Sci. Eng. A*, 2013.

[142] L. E. Murr *et al.*, "Microstructures and mechanical properties of electron beam-rapid manufactured Ti-6Al-4V biomedical prototypes compared to wrought Ti-6Al-4V," *Mater. Charact.*, 2009.

[143] H. Guleryuz and H. Cimenoglu, "Surface modification of a Ti-6Al-4V alloy by thermal oxidation," *Surf. Coatings Technol.*, 2005.

[144] H. R. Voorhees and M. Prager, "Assessment And Use Of Creep-Rupture Properties," *ASM Handb. Mech. Test. Eval.*, vol. 8, pp. 383–397, 2000.

[145] A. C. Fischer-Cripps, "Nanoindentation," in *Nanoindentation*, 2011, pp. 21–38.

[146] E. Broitman, "Indentation Hardness Measurements at Macro-, Micro-, and Nanoscale: A Critical Overview," *Tribology Letters*, vol. 65, no. 1. 2017.

[147] W. J. Zong, D. Wu, and C. L. He, "Radius and angle determination of diamond Berkovich indenter," *Meas. J. Int. Meas. Confed.*, 2017.

[148] U. Ramamurty and J. Il Jang, "Nanoindentation for probing the mechanical behavior of molecular crystals-a review of the technique and how to use it," *CrystEngComm*, 2014.

[149] D. Verma, T. Qu, and V. Tomar, "Scale Dependence of the Mechanical Properties and Microstructure of Crustaceans Thin Films as Biomimetic Materials," *JOM*. 2015.

[150] W. H. Poisl, W. C. Oliver, and B. D. Fabes, "The relationship between indentation and uniaxial creep in amorphous selenium," *J. Mater. Res.*, vol. 10, no. 8, pp. 2024–2032, 1995.

[151] R. Goodall and T. W. Clyne, "A critical appraisal of the extraction of creep parameters from nanoindentation data obtained at room temperature," *Acta Mater.*, vol. 54, no. 20, pp. 5489–5499, 2006.

[152] L. Shen, W. C. D. Cheong, Y. L. Foo, and Z. Chen, "Nanoindentation creep of tin and aluminium: A comparative study between constant load and constant strain rate methods," *Mater. Sci. Eng. A*, vol. 532, pp. 505–510, 2012.

[153] M. Haghshenas, O. Totuk, M. Masoomi, S. M. Thompson, and N. Shamsaei, "Small-scale mechanical properties of additively manufactured Ti-6Al-4V," in *Solid Freeform Fabrication Symposium*, 2017.

[154] A. Łukaszek-Sołek *et al.*, "Microstructure and Phase Transformation of Ti-6Al-

4V," *Mater. Sci. Eng. A*, vol. 2, no. 1–2, pp. 27–30, 2013.

[155] M. Hardiman, T. J. Vaughan, and C. T. McCarthy, "The effects of pile-up, viscoelasticity and hydrostatic stress on polymer matrix nanoindentation," *Polym. Test.*, vol. 52, pp. 157–166, 2016.

[156] A. Bolshakov and G. M. Pharr, "Influences of pileup on the measurement of mechanical properties by load and depth sensing indentation techniques," *J. Mater. Res.*, vol. 13, no. 4, pp. 1049–1058, 1998.

[157] N. Mohan, J. Cheng, J. R. Greer, and a. Needleman, "Uniaxial tension of a class of compressible solids with plastic non-normality," *J. Appl. Mech. Trans. ASME*, 2013.

[158] A. A. Elmustafa, "Pile-up/sink-in of rate-sensitive nanoindentation creeping solids," *Model. Simul. Mater. Sci. Eng.*, 2007.

[159] W. B. Li, J. L. Henshall, R. M. Hooper, and K. E. Easterling, "The mechanisms of indentation creep," *Acta Metall. Mater.*, vol. 39, no. 12, pp. 3099–3110, 1991.

[160] B. G. Yoo, K. S. Kim, J. H. Oh, U. Ramamurty, and J. Il Jang, "Room temperature creep in amorphous alloys: Influence of initial strain and free volume," *Scr. Mater.*, vol. 63, no. 12, pp. 1205–1208, 2010.

[161] P. De Hey, J. Sietsma, and A. Van Den Beukel, "Structural disordering in amorphous Pd 40 Ni 40 P 20 induced by high temperature deformation," *Acta Mater.*, vol. 46, no. 16, pp. 5873–5882, 1998.

[162] C. Wang, Q. P. Cao, X. D. Wang, D. X. Zhang, S. X. Qu, and J. Z. Jiang, "Time-dependent shear transformation zone in thin film metallic glasses revealed by nanoindentation creep," *J. Alloys Compd.*, vol. 696, pp. 239–245, 2017.

[163] M. Masoomi, J. W. Pegues, S. M. Thompson, and N. Shamsaei, "A numerical and experimental investigation of convective heat transfer during laser-powder bed fusion," *Addit. Manuf.*, 2018.

[164] T. Bose and M. Rattan, "Effect of thermal gradation on steady state creep of functionally graded rotating disc," *Eur. J. Mech. A/Solids*, vol. 67, pp. 169–176, 2018.

[165] R. Schwaiger, B. Moser, M. Dao, N. Chollacoop, and S. Suresh, "Some critical experiments on the strain-rate sensitivity of nanocrystalline nickel," *Acta Mater.*, vol. 51, no. 17, pp. 5159–5172, 2003.

[166] M. W. Barsoum, "Fundamentals Of Ceramics," *Vasa*, p. 622, 2003.

[167] S. Ando, K. Nakamura, K. Takashima, and H. Tonda, "{1122} <1123> slip in

magnesium single crystal," *Japan Inst. Light Met.*, vol. 42, no. 12, pp. 765–771, 1992.

[168] M. Haghshenas, Y. Wang, Y. T. Cheng, and M. Gupta, "Indentation-based rate-dependent plastic deformation of polycrystalline pure magnesium," *Mater. Sci. Eng. A*, vol. 716, no. November 2017, pp. 63–71, 2018.

[169] N. A. Stelmashenko, M. G. Walls, L. M. Brown, and Y. V. Milman, "Microindentations on W and Mo oriented single crystals: An STM study," *Acta Metall. Mater.*, vol. 41, no. 10, pp. 2855–2865, 1993.

[170] Q. Ma and D. R. Clarke, "Size dependent hardness of silver single crystals," *J. Mater. Res.*, vol. 10, no. 4, pp. 853–863, 1995.

[171] M. F. Ashby, "The deformation of plastically non-homogeneous materials," *Philos. Mag.*, vol. 21, no. 170, pp. 399–424, 1970.

[172] N. a. Fleck, G. M. Muller, M. F. Ashby, and J. W. Hutchinson, "Strain gradient plasticity: Theory and experiment," *Acta Metall. Mater.*, vol. 42, no. 2, pp. 475–487, 1994.

[173] G. Z. Voyiadjis and D. Faghihi, "Microstructure to macro-scale using gradient plasticity with temperature and rate dependent length scale," in *Procedia IUTAM*, 2012, vol. 3, pp. 205–227.

[174] G. Z. Voyiadjis and M. Yaghoobi, "Large scale atomistic simulation of size effects during nanoindentation: Dislocation length and hardness," *Mater. Sci. Eng. A*, 2015.

[175] B. SridharBabu, A. Kumaraswamy, and B. AnjaneyaPrasad, "Effect of Indentation Size and Strain Rate on Nanomechanical Behavior of Ti-6Al-4VAlloy," *Trans. Indian Inst. Met.*, vol. 68, no. 1, pp. 143–150, 2014.

[176] J. Sieniawski, W. Ziaja, K. Kubiak, M. Motyka, Titanium Alloys-Advances in Properties Control, 2013.

[177] B. Baufeld, O. Van Der Biest, and R. Gault, "Microstructure of Ti-6Al-4V specimens produced by shaped metal deposition," *Int. J. Mater. Res.*, vol. 100, no. 11, pp. 1536–1542, 2009.

[178] C. de Formanoir, S. Michotte, O. Rigo, L. Germain, and S. Godet, "Electron beam melted Ti-6Al-4V: Microstructure, texture and mechanical behavior of the as-built and heat-treated material," *Mater. Sci. Eng. A*, vol. 652, pp. 105–119, 2016.

[179] T. Ahmed and H. J. Rack, "Phase transformations during cooling in $\alpha+\beta$ titanium alloys," *Mater. Sci. Eng. A*, 1998.

[180] G. Lütjering and J. C. Williams, "Special Properties and Applications of Titanium," in *Titanium*, 2007.

[181] M. Neikter, P. Åkerfeldt, R. Pederson, and M. L. Antti, "Microstructure characterisation of Ti-6Al-4V from different additive manufacturing processes," in *IOP Conference Series: Materials Science and Engineering*, 2017, vol. 258, no. 1.

[182] G. Lütjering, "Influence of processing on microstructure and mechanical properties of (α+β) titanium alloys," *Mater. Sci. Eng. A*, 1998.

[183] R. Boyer, G. Welsch, and E. W. Colilngs, *Materials Properties Handbook: Titanium Alloys*. 1994.

[184] S. Leuders *et al.*, "On the mechanical behaviour of titanium alloy TiAl6V4 manufactured by selective laser melting: Fatigue resistance and crack growth performance," *Int. J. Fatigue*, 2013.

[185] S. Q. Wu *et al.*, "Microstructural evolution and microhardness of a selective-laser-melted Ti-6Al-4V alloy after post heat treatments," *J. Alloys Compd.*, 2016.

[186] Y. Xu, Y. Lu, K. L. Sundberg, J. Liang, and R. D. Sisson, "Effect of Annealing Treatments on the Microstructure, Mechanical Properties and Corrosion Behavior of Direct Metal Laser Sintered Ti-6Al-4V," *J. Mater. Eng. Perform.*, 2017.

[187] Y. S. Zhang *et al.*, "Microstructure and mechanical properties of a high-oxygen core-shell network structured Ti6Al4V alloy," *Vacuum*, 2018.

[188] M. Zhang, Y. Yang, D. Wang, Z. Xiao, C. Song, and C. Weng, "Effect of heat treatment on the microstructure and mechanical properties of Ti6Al4V gradient structures manufactured by selective laser melting," *Mater. Sci. Eng. A*, 2018.

[189] M. Haghshenas, "Multi-cycling instrumented nanoindentation of a Ti-23Nb-0.7Ta-2Zr-1.2O alloy in annealed condition," *Mater. Sci. Eng. A*, 2017.

[190] W. D. Nix and H. Gao, "Indentation size effects in crystalline materials: A law for strain gradient plasticity," *J. Mech. Phys. Solids*, 1998.